Variational data assimilation of satellite observations to estimate volcanic ash emissions

Lu, Sha

DOI
10.4233/uuid:81eb2519-1125-469b-b3f4-4674ea495f65

Publication date
2017

Document Version
Final published version

Citation (APA)
Lu, S. (2017). *Variational data assimilation of satellite observations to estimate volcanic ash emissions*. [Dissertation (TU Delft), Delft University of Technology]. https://doi.org/10.4233/uuid:81eb2519-1125-469b-b3f4-4674ea495f65

Variational data assimilation of satellite observations to estimate volcanic ash emissions

Variational data assimilation of satellite observations to estimate volcanic ash emissions

Proefschrift

ter verkrijging van de graad van doctor
aan de Technische Universiteit Delft,
op gezag van de Rector Magnificus prof. ir. K.C.A.M. Luyben,
voorzitter van het College voor Promoties,
in het openbaar te verdedigen op woensdag 1 maart 2017 om 10.00 uur

door

Sha Lu

Master of Science in Numerical Mathematics,
Shandong University, China
geboren te Shandong, China

Dit proefschrift is goedgekeurd door de

promotor: Prof. dr. ir. H.X. Lin
promotor: Prof. dr. ir. A.W. Heemink

Samenstelling promotiecommissie:

Rector Magnificus,	voorzitter
Prof. dr. ir. H.X. Lin,	Technische Universiteit Delft, Promotor
Prof. dr. ir. A.W. Heemink,	Technische Universiteit Delft, Promotor
Onafhankelijke leden:	
Prof. dr. ir. H.W.J. Russchenberg,	Technische Universiteit Delft
Prof. dr. ir. M. Verlaan,	Technische Universiteit Delft
Prof. dr. ir. P.J.H. Builtjes,	Free University of Berlin, Germany
Prof. dr. Wei Han,	Numerical Weather Prediction Center, CMA, China
Overige leden:	
Dr. ir. A.J. Segers,	TNO Utrecht, The Netherlands

Dr. ir. A.J. Segers heeft in belangrijke mate aan de totstandkoming van het proefschrift bijgedragen.

Keywords: variational data assimilation, trajectory-based 4D-Var, volcanic ash emissions, volcanic ash forecasts, remote sensing measurements, correlations, evaluation score.

Printed by: Ipskamp Printing

ISBN 978-94-92516-43-5

An electronic version of this dissertation is available at
http://repository.tudelft.nl/.

Contents

Summary

Volcanic eruptions release a large amount of volcanic ash, which can pose hazard to human and animal health, land transportation, and aviation safety. Volcanic Ash Transport and Dispersion (VATD) models are critical tools to provide advisory information and timely volcanic ash forecasts. Due to the complexity and the uncertainty of many dynamic processes involved in the volcanic ash distribution, even the most advanced VATDs today are not capable to reproduce the reality accurately. It is necessary to integrate available observations in the models for more accurate predictions by emloying data assimilation techniques.

In addition to a valid VATD, ash emissions, usually used as input so the model, are crucial for the forecasts of the locations and shapes of the ash cloud. In general, the eruption source parameters for the construction of the emission are poorly known, which include Plume Height (PH), Mass Eruption Rate (MER) and vertical distribution of the emission rate. Even when PH can be obtained from ground-based observations in some cases, the emission source computed from this PH and a MER empirically related to this PH remains highly uncertain. Not to mention the volcanoes which are unmonitored or hardly accessible, the PH can merely be retrieved from satellite data with a large uncertainty and temporal insufficiency. Fortunately, satellite instruments are able to observe the movement of an ash cloud with a global coverage. Therefore, this thesis focuses on the estimation of the volcanic ash emissions by assimilating Ash Mass Loadings (AMLs) retrieved from satellite data to improve the accuracy of forecasts.

Among all available data assimilation approaches, Four Dimensional Variational assimilation (4D-Var) approach was chosen as a suitable one. 4D-Var seeks an optimal set of parameters, including model states, initial conditions and systematic parameters, by minimizing a cost function which combines the model simulations and observations over a period according to their statistic properties. 4D-Var with a standard form of the cost function is tested in a twin experiment framework, where synthetic observations of ash columns computed from model simulated 3D ash concentrations are used. The results show that Standard 4DVar (Std4DVar) is unable to reconstruct the vertical profile of the emission. The injection layer containing the maximal amount of emission rate cannot be accurately determined. This failure is attributed to the fact that AML data lacks vertical resolution. Using the AMLs, it is difficult to reconstruct the volcanic ash emission presented in forms of an eruption column.

To deal with this problem, a Trajectory-based 4D-Var (Trj4DVar) approach is proposed. Trj4DVar reformulates the cost function in a regression type which computes the total difference between observed ash columns and a linear combination of simulated trajectories coupled with a priori emission knowledge. The results of twin experiments show that, for most cases, Trj4DVar is capable of estimating

the input emission column when a large assimilation window (> 6 hours) is used. The twin experiments is repeated where different values of noise are given in the synthetic observations or perturbations are used in the meteorologic data. The outcomes show that there is still a small possibility that Trj4DVar fails to determine the injection height accurately. Being disturbed by the weather condition (light and cloud, etc) at that moment, satellite instrument can be hampered to observe the ash cloud, which may increase the possibility of failure for the use of Trj4DVar. To remedy this, Trj4DVar is modified to incorporate observations of PH and MER in addition to satellite AMLs. The modified Trj4DVar is shown to be able accurately estimate the injection height based on the results of twin experiments.

When it comes to using real-life field data, the situation is more complicated. The detection of volcanic ash can be disturbed by the weather condition such as water vapor. This will result in observations of undetected or wrongly-detected ash. Besides, many sensors ,such as UV and visible sensors, have limited temporal coverage which can only observe during daylight. In order to find effective method in dealing with the temporal and sometimes spatial insufficiency of the data, investigations are carried out on how to use the data properly to benefit more and produce a reasonable estimate. A prepossessing procedure and guidance on the proper use of satellite data are presented.

Finally, a deeper analysis is given on the failure of using Std4DVar in this application. It is found that using Std4DVar to assimilate remote sensing data can be tricky. Remote sensing measures quantities that combine several state variables. This creates Sensor-Induced Correlations between the state variables which share the same observation variable and may be physically unrelated. This may cause numerical problems resulting in a low convergence rate or inaccurate estimates of parameters using gradient-based variational assimilation if an erroneous or improper specification of error statistics is adopted. These problems are usually ignored when a reasonable result is obtained, or are avoided by reducing the 3D model to a 2D model. However, it results in significantly unreliable and misguiding estimates for the application in this thesis. Two criteria are proposed to quantify the negative effects of the SICs, which give indications of the effectiveness of the assimilation process and the forecast quality. They are simple to implement and very practical for the use of remote sensing data. They are tested in the twin experiments. The results show that they are able to give evaluation on the design and configuration of the assimilation system with remote sensing data.

Samenvatting

Bij vulkaanuitbarstingen komen er een grote hoeveelheid vulkanische as in de lucht, die gevaar kan opleveren voor de gezondheid van mensen en dieren, transport over land, en de veiligheid van de luchtvaart. Vulkanic Ash Transport en Dispersion (VATD) modellen zijn cruciaal gereedschappen waarmee adviesdiensten tijdig prognoses kunnen doen. Vanwege de complexiteit en de onzekerheid van de vele dynamische processen bij de vulkanische as distributie, zijn zelfs de meest geavanceerde VATDs van tegenwoordig niet in staat om de realiteit nauwkeuriger weer te geven. Om nauwkeurigere voorspellingen te maken moeten beschikbare waarnemingen in de modellen worden geïntegreerd met behulp van data-assimilatie technieken.

Naast een geldige VATD, gegevens over asemissies, die vaak als invoer voor het model worden gebruikt, zijn cruciaal voor de prognoses van de locaties en vormen van de aswolk. In het algemeen zijn de uitbarsting parameters voor de constructie van de emissie slecht bekend, zoals de Plume Hoogte (PH), Mass Eruption Rate (MER) en de verticale distributie van as emissie. Zelfs wanneer PH kan worden verkregen door grond waarneming stations in sommige gevallen, de emissiebron berekend uit deze PH en een MER empirisch in verband met deze PH blijven hoogst onzeker. Niet te vergeten de vulkanen zijn vaak ongecontroleerd of nauwelijks toegankelijk. De PH kan nauwlijks worden via de satelliet genemten en vaak met grote onzekerheid. Gelukkig zijn satelliet-instrumenten in staat om verspreiding van een aswolk te observeren met een wereldwijde dekking. Dit proefschrift richt zich op de schatting van de vulkanische asuitstoot door middel van het assimileren van Ash Mass Loadings (AMLs) opgehaald uit satellietgegevens ter verbetering van de nauwkeurigheid van de prognoses.

Van alle beschikbare data assimilatie benaderingen, Vier Dimensionaal Variationele assimilatie (4D-Var) methode werd gekozen als een geschikte aanpak. 4D-Var zoekt een optimale set parameters, waaronder modelstaten, beginwaarden en systeemparameters, door het minimaliseren van een kostenfunctie die de modelsimulaties combineert met observaties over een periode op basis van hun statistische eigenschappen. 4D-Var met een standaardvorm van de kostenfunctie wordt getest in het kader van een twin-experiment waar de synthetische waarnemingen van as kolommen berekend op basis van model gesimuleerde 3D asconcentraties worden gebruikt. De resultaten tonen aan dat Standaard 4DVar (Std4DVar) niet instaat is het verticale profiel van de emissie te reconstrueren. De injectielaag met de maximale hoeveelheid van de emissie kan niet nauwkeurig worden bepaald. Dit falen wordt toegeschreven aan het feit dat AML data verticale resolutie ontbreken. Het is moeilijk om de vulkanische asemissie te reconstrueren met de AML data in de vorm van een uitbarsting kolom. Een Traject gebaseerde 4D-Var (Trj4DVar) benadering is voorgesteld om dit probleem op te lossen. Trj4DVar herformuleert de kosten-

functie in een regressie type dat het totale verschil tussen waargenomen as zuilen en een lineaire combinatie van gesimuleerde trajecten gecombineerd met a priori kennis over emissie berekent. De resultaten van de twin-experimenten blijken dat in de meeste gevallen Trj4DVar de emissiekolommen goed kan schatten wanneer er een grote assimilatie venster (> 6 uur) wordt gebruikt. De twin-experimenten worden uitgevoerd met verschillende ruiswaarden in de synthetische waarnemingen of verschillende verstoringen in de meteorologische gegevens. De resultaten tonen dat er nog een kleine kans is dat Trj4DVar de hoogte van injectie niet nauwkeurig kan bepalen. Verschillende weersomstandigheden (licht en wolk, enz.) kunnen een satelliet-instrument belemmeren om de aswolk te observeren, waardoor de kans van het falen voor Trj4DVar groter wordt. Om dit te verhelpen, wordt Trj4DVar aangepast om observaties van PH en MER op te nemen in aanvulling op de AMLs waarnemingen van de satelliet. Deze aanpassing in Trj4DVar levert een nauwkeurige schatting van de as injectiehoogte zoals gebleken uit de resultaten van twin-experimenten.

Als het gaat om het gebruik van velddata (van echte metingen) is de situatie ingewikkelder. De detectie van vulkanische as kan worden verstoord door de weersomstandigheden zoals waterdamp. Dit zal resulteren in onopgemerkte of verkeerd gedetecteerde aswolk. Bovendien, veel sensoren, zoals UV en zichtbare sensoren hebben beperkte tijd dekking die alleen kan waarnemen bij daglicht. Met het oog op effectieve methode te vinden de behandeling van de soms onvoldoende temporele en ruimtelijke gegevens, hebben we onderzoek uitgevoerd op de vraag hoe de gegevens in deze situatie kunnen worden gebruikt om meer te profiteren en een redelijke schatting te produceren. Een voorbewerking procedure en richtlijn op het juiste gebruik van satellietgegevens worden gepresenteerd.

Tenslotte wordt een diepere analyse gegeven op het falen van Std4DVar met standaard kostenfunctie in deze toepassing. Het gebruik van Std4DVar om remote sensing data te assimileren kan in sommige gevallen problemen leveren. Remote sensing meet grootheden die in feit een aantal toestandsvariabelen combineren. Dit creëert valse correlaties tussen de toestandsvariabelen die dezelfde observatie variabele delen. Dit kan numerieke problemen veroorzaken zoals langzame convergentie of onjuiste schattingen in gradiënten voor variationele assimilatie. Deze problemen worden meestal genegeerd wanneer er een redelijk resultaat is verkregen, of worden vermeden door het 3D-model tot een 2D-model te reduceren. Echter ze leiden tot een aanmerkelijk onbetrouwbare en misleidende prognoses voor de toepassing in dit proefschrift. Twee criteria zijn voorgesteld om de negatieve effecten van de onechte correlaties te kwantificeren en indicaties van de effectiviteit van het assimilatieproces en prognose kwaliteit te geven. Zij worden getest in de twin-experimenten. De resultaten laten zien dat zij in staat zijn om het ontwerp en de configuratie van het assimilatiesysteem met remote sensing data te evalueren.

1

Introduction

1

1.1. Motivation: hazard of volcanic ash

Every now and then, the Earth undertakes tremendous explosive volcanic eruptions. The eruptions inject large amounts of chemicals, corrosive gases, and very small rock fragments known as volcanic ash into the upper troposphere and lower stratosphere. The fine ash with diameter less than 64 μm can be transported by wind at a continental scale. Due to its wide dispersal, volcanic ash can have great impacts on society, including human and animal health (Baxter *et al.*, 1999; Horwell *et al.*, 2003), disruption to aviation (Casadevall, 1994; Casadevall *et al.*, 1996; Prata, 2009), disruption to critical infrastructure (e.g., electric power supply systems, telecommunications, water and waste-water networks, transportation) (Stewart *et al.*, 2006; Wilson *et al.*, 2010; Wardman *et al.*, 2012; Wilson *et al.*, 2014), agriculture (Cook *et al.*, 1981; Cronin *et al.*, 1997), buildings and structures(Spence *et al.*, 2005). The next sections describe the various hazards in more detail.

1.1.1. Impact on human and animal health

Aerosol particles with a diameter less than 10 μm are known as Particular Matter $<$ 10 μm (PM_{10}). PM_{10} is harmful to human beings, therefore, as a source of PM_{10}, volcanic ash can impact human health. The suspended PM_{10} in the air are inhalable, so that people exposed to ash falls can experience respiratory discomfort. The reported symptoms include breathing difficulty, runny nose, throat irritation accompanied with by dry coughing sometimes, and eye and skin irritation.Most of these effects are short-term and are not considered to pose a significant health risk to those without pre-existing respiratory conditions (Horwell and Baxter, 2006). People with preexisting chest may develop severe bronchitic symptoms which can last several days after exposure to ash. People with asthma may experience shortness of breath, couching and wheezing (Shimizu *et al.*, 2007). Chronic health effects from volcanic ash falls are possible, since exposure to free crystalline silica may cause silicosis. However, there are no documented cases of silicosis developed from exposure to volcanic ash, and there lacks long-term studies which are necessary to evaluate these effects (Horwell and Baxter, 2006).

Ingesting ash may also be harmful to livestock. It may cause abrasion of the teeth for grazing animals, and cause fluorine poisoning in cases of high fluorine content (> 100 μg g^{-1}) (Cronin *et al.*, 2003). The eruption of Laki in 1783 released ash and gas containing high levels of Hydrogen Fluoride, which resulted in fluorine poisoning in human and livestock. The 1995/96 Mount Ruapehu eruptions in New Zealand created 1-3 mm of ash falls on the grazing land, and two thousand ewes and lambs died as a result of being affected by fluorosis (Cronin *et al.*, 2003).

1.1.2. Disruption to ground-based transportation

Volcanic ash falls may disturb ground-based transportation system over large regions for hours to days. Small accumulation of ash will reduce visibility and create slippery runways and taxiways, which makes driving difficult and dangerous (Guffanti *et al.*, 2009). In addition, fast traveling vehicles will stir up ash and cre-

ate secondary emissions, which can perpetuate ongoing visibility hazards. Railway transportation is less vulnerable, with disruptions mainly caused by the reduction in visibility (Wilson *et al.*, 2012). Ash accumulation of more than a few millimeters requires removal before airports can resume full operations. Ash must be disposed of in a manner that prevents it from being remobilized by wind and aircraft (Guffanti *et al.*, 2009). Marine transport can also be impacted by volcanic ash. Ash fall will block air and oil filters and abrade any moving parts if ingested into engines. Navigation will be impacted by a reduction in visibility during ash fall. Vesiculated ash (pumice and scoria) will float on the water surface in 'pumice rafts' which can clog water intakes quickly, leading to over heating of machinery Wilson *et al.* (2012).

1.1.3. Disruption to aviation

The airborne ash is an extreme hazard to everything flying including birds and aircrafts during its residence (Casadevall, 1992). Drifting ash clouds, consisting of corrosive gas and fine rock fragments, are carried away by winds. Large volcanic eruptions produce clouds that may transport over a continent domain and even circle the globe in a matter of weeks. The composition of most ash is such that its melting temperature is within the operating temperature ($> 1000°C$) of modern large jet engines Taylor and Lichte (1980). The melting ash would damage the engine of jet planes and lead to total engine failure. The threat of volcanic ash hazards to aviation safety first received public attention in 1980, when several commercial jet aircrafts were damaged flying through volcanic ash clouds duo to the following eruptions: Galunggung Volcano in Indonesia in 1982; Redoubt Volcano in Alaska, U.S. in 1989 and 1990 (Casadevall, 1994); and Mount St. Helens in Washinton, U.S in 1980. The interest in aviation safety grew rapidly after Mount Pinatubo volcano in 1991 caused significant damage to aircraft, including engine failures, and severely disrupted regional air operations (Casadevall *et al.*, 1996). Rerouting and cancellation of flights may result from the contaminated air routs and airport facilities by drifting clouds of volcanic ash and affect local economy. The repair and replacement costs associated with airplane-ash cloud encounters are also high. For instance, the repairing cost of the Boeing 747-400 damaged by an ash could from redoubt Volcano, Alaska, U.S., in 1989 was estimated to exceed $80 million US dollars (Casadevall, 1992).

1.1.4. Overview of severe economic losses

An overview of severe economic losses due to volcano eruptions are shown in Tab. 1.1, where the information is taken partly from Annen and Wagner (2003). The significant impact of Eyjafjallajökull eruption in 2010 was impressive and historical, which brought the UCL Institute for Risk and Disaster Reduction to provide an integrated analysis covering volcanology, geophysics, rock and ice physics, meteorology, statistics, mechanical engineering, systems engineering, transport engineering, hazard and risk communication, law and ethics (Ucl-Irdr, 2010). The eruption of Eyjafjallajökull began on 14 April 2010 and became an international event in mid April 2010 as the ash cloud spread eastwards towards Europe. It caused an unprecedented closure of UK, European and North Atlantic air space from 15-20

Table 1.1: Costs related to volcanic eruptions in U.S. Dollars reported with different information sources, taken partly from Annen and Wagner (2003).

Eruption	Year	Costs (U.S. dollars)	Source
Eyjafjallajökull, Iceland	2010	5 billion	Oxford-Economics (2010)
Pinatubo, Philippines	1991	553.5 million	Rantucci (1994)
Redoubt, USA	1990	160 million	AVO & Miller *et al.* (1993)
Soufriere Hills, Montserrat, U.K.	1995	120 million	MunichRe
Pacaya, Guatemala	1998	75 million	Press
Mayon, Philippines	1993	56.5 million	SwissRe
Rabaul, Papua New Guinea	1994	40.26 million	OCHA

Note: OCHA: United Nations Office for the Coordination of Humanitarian Affairs, AVO: Alaska Volcanic Observatory, SwissRe and MunichRe are reinsurance companies.

April 2010. This was followed by further episodes of air travel disruption. Business travellers and tourists were stranded, industrial production was affected as raw materials could not be flown in.

The volcanic activities at a similarly tremendous scale are not unusual. Explosive eruptions, comparable to the Eyjafjallajökull 2010 event, occur in Iceland every 20-40 years on average. The 1821-1823 Eyjafjallajökull eruption lasted 14 months. There is no doubt that future explosive eruptions, coupled with appropriate meteorological conditions, have the potential to cause further disruption to air transport. What makes it worse is that it is not possible to predict either when this will occur or at what scale (Ucl-Irdr, 2010).

However, the losses caused by Eyjafjallajökull 2010 event could have been reduced given good prediction of the volcanic ash transportation by making use of the existing observations of the ash clouds. Consequently, the ash-affected region with potential threat to aviation safety could be recognized in advance, give the prediction of ash clouds and safe ash levels. The response of the aviation advisory institutes to the volcanic eruptions can be more efficient and flexible. The impact of the eruption on regional air space could be predicted and be better prepared for.

1.2. Volcanic ash transport and dispersion models

Pyroclastic particles, known as tephra, can be classified by their diameters. Pyroclastic particles greater than 64 mm in diameter is referred to as volcanic bomb when molten, or volcanic block when solid. Lapilli range from 2 to 64 mm in diameter. Particles with diameter less than 2 mm are known as volcanic ash, and with diameter less than 64 μm are usually defined as fine ash. Blocks and lapilli follow ballistic and non-ballistic trajectories, and fall rapidly near the volcano. Volcanic ash remain airborne from hours to days, while fine ashes can remain entrapped in the atmosphere for months to years and cover wide areas downwind.

In order to define hazards to aircraft during volcanic eruptions and to provide

warnings on actual ash fall concentrations, volcanic ash transport and dispersion models (VATDs) have been developed to forecast the location and movement of ash clouds over hours to days. Considerable progress has been made during the last three decades on the development of effective VATDs through increasingly comprehensive understanding of ash movement and removal (aggregation and deposition) mechanism. In addition, models with more complexity that can simulate more realistic physical processes are affordable nowadays, thanks to the increasingly powerful computational capability of computers. Nowadays, models are basically used to quantify hazard scenarios and to provide short-range forecasts during emergency.

There are a number of models with different focuses and approximations. Some focus on particle settling and deposition in a wind field (Carey and Sparks, 1986; Bursik *et al.*, 1992b; Koyaguchi, 1994; Koyaguchi and Ohno, 2001; Bonadonna and Phillips, 2003; Bonadonna *et al.*, 1998; Bursik *et al.*, 1992a). Lagrangian particle tracking are devoted to tracking the trajectories of particles and the position of a volcanic cloud (Heffter and Stunder, 1993; D'amours, 1998; Searcy *et al.*, 1998; Draxler and Hess, 1998; Jones *et al.*, 2007). They are mainly used by the Volcanic Ash Advisory Centers (VAACs) to determine the potentially affected regions for the purposes of aviation safety. Advection-diffusion Eulerian models solve the advection-diffusion-sedimentation equation (Suzuki, 1983; Armienti *et al.*, 1988; Macedonio *et al.*, 1988, 2005; Glaze and Self, 1991; Connor *et al.*, 2001; Bonadonna *et al.*, 2002a; Folch and Felpeto, 2005; Costa *et al.*, 2006; Pfeiffer *et al.*, 2005). They are mainly used for the purposes of civil protection, for instance, hazard maps can be developed to give public warnings.

Each family of models can have a range of complexity, and each with their own advantages and drawbacks. Simple models can be less accurate. Their simulation are usually based on hypotheses that simplify the physics. Some precesses can be oversimplified, which may lead to poor matching between model outputs and reality. This is a critical issue in the case of volcanic ash transport. Particle dispersion and deposition is mainly ruled by atmospheric properties. Particle sedimentation transitions from inertial-dominated single particle settling to aggregation-dominated very fine particle (< 30 μm in diameter) settling as distance increases from the source (Rose and Durant, 2009). During one eruption, particle size distribution exhibit a wide range of variety both within the emission source (depending on the eruption type) and during the transport. A poor estimation on the eruption source and/or oversimplified removal processes can result in substantial bias. Yet, simple models require lower computational effort. They are suitable for inverse problems or immediate gross predictions.

In contrast, complex models are more accurate theoretically. However, they generally require more inputs, set-up times, computational costs and user expertise, where the inputs may not be always available. Therefore, they can be inefficient to produce short-term forecasts for the decision-making authorities during an episode of pre-eruptive crisis or even during the course of eruption.

1.3. Eruption source parameters

Initial source information on the volcanic emissions is critical for the quality of the forecasts using VATD models. Mastin *et al.* (2009b) has developed "Eruption Source Parameters (ESP)" for the definition of eruptive source, such as plume height H, mass eruption rate M, duration D, and the mass fraction m_{63} of erupted debris with diameter less than 63 μm.

1.3.1. Plume height

Plume height H is defined as the maximum height of an eruption column. It does not necessarily coincide with the injection height which contains the maximum of the eruptive mass. Most of the measurements provide information of the plume height, not the injection height. Plume height can be obtained primarily from ground-based or airborne visual observations, radar measurements, and cloud satellite temperature. The observations are not always available, especially for the unmonitored volcanoes or on the first a few minutes to hours after an eruption is detected.

Plume height has a significant influence on the vertical and horizontal structure of the ash cloud forecast downstream. Since the speed and direction of wind changes with altitude, the location and shape of ash cloud changes with plume heights. In order to accurately represent the evolution of the ash cloud, it is important to accurately determine the height at which ash particles are emitted into the atmosphere.

1.3.2. Vertical distribution

The vertical distribution of the ash load during an eruption is a parameter that is difficult to estimate. In general, most of the emitted ash is assumed to be found well above the ground and close to the plume top (Sparks, 1986; Sparks *et al.*, 1997). However, this is not always correct, for instance, if the volcano plume height is varying rapidly or the particles are released over a large range of heights. In addition, it is difficult to ascertain about the lower plume boundary (plume extent) or the information on lower part of the eruption column. Therefore, for operational use, uniform vertical distribution is sometimes employed in order to avoid predicting no ash where a significant hazard may exist.

1.3.3. Mass eruption rate

Up to now, there is no direct method of measuring the mass eruption rate or the emitted mass flux of an eruption. As a result, many VATDs use an empirical relationship to relate observed maximum plume height to the mass flux. The empirical relationships between plume height and mass eruption rate M (kg s^{-1}), or between plume height and volumetric flow rate V (Dense-Rock Equivalent m^3 s^{-1}) can be used for the determination of the emission rate of mass or volume. For instance, Dacre *et al.* (2011) used an empirical relationship for the 2010 Eyjafjallajökull eruptive events as follows:

$$H = 0.365M^{0.225}, \tag{1.1}$$

Table 1.2: ESP including injection height, duration, eruption rate, volume that are used to determine the eruption properties within the LOTOS-EUROS. Adapted from Mastin *et al.* (2009b). Type "M", or mafic types, include basaltic and ultramafic magmas. Type "S", or silicic types, include andesite, dacite, rhyolite, and others such as phonolite that can produce high ash columns. Submarine eruptions that occur beneath at least 50 m water depth are assigned type "0".

ESP	Type	Height above vent (km)	Duration (h)	Eruption rate (kg s^{-1})	Volume (km^3)	m_{63}
M0	standard mafic	7	60	1.0×10^5	0.01	0.05
M1	small mafic	2	100	5.0×10^3	0.001	0.02
M2	medium mafic	7	60	1.0×10^5	0.01	0.05
M3	large mafic	10	5	1.0×10^6	0.17	0.1
S0	standard silicic	11	3	4.0×10^6	0.015	0.4
S1	small silicic	5	12	2.0×10^5	0.003	0.1
S2	medium silicic	11	3	4.0×10^6	0.015	0.4
S3	large silicic	15	8	1.0×10^7	0.15	0.5
S8	co-ignimbrite silicic	25	0.5	1.0×10^8	0.05	0.5
S9	Brief silicic	10	0.01	3.0×10^6	0.0003	0.6
U0	default submarine	0	-	-	-	

where the power law was based on a fit to a look-up table constructed by the National Oceanic and Atmospheric Administration (NOAA) for the VAFTAD model (Heffter and Stunder, 1993), and the pre-factor was determined by comparing the values to the best fit curve presented by Mastin *et al.* (2009b). This empirical relationship is not necessarily valid, especially for phreatomagmatic eruptions or small eruptions that have no access into the stratosphere (at mid latitudes at about 10 km; the Eyjafjallajökull 2010 eruption was an example of this) due to the influence of variable meteorology (stratification and wind) (Dacre *et al.*, 2011).

In practice, the fine ash fraction of total emitted mass is important for quantitative predictions of ash concentrations at long-range. This fine ash refers to particles with diameter $< 63\ \mu$m , which dominate the transport of downstream plume. Studies showed that larger ash particles cannot survive after several hundred kilometers from the volcano, and fine ash retains consistent size characteristics in the distal part of ash cloud (Rose and Durant, 2009; Durant and Rose, 2009). The fine ash fraction varies a lot depending on different types of eruption.

1.3.4. Mastin's ESP

Mastin *et al.* (2009b) provides details on each source parameter for each ESP type (see Tab. 1.2). Eleven eruption ESP types were identified by compiling published data on plume height, erupted volume or mass, and duration from well-documented eruptions: small, medium, and large eruptions of mafic and silicic magma respectively; silicic co-ignimbrite (i.e. co-pyroclastic flow) plumes; "brief" vulcanian-style events possibly associated with lava-dome collapse; submarine eruptions from beneath over 50 m water depth; and "standard" values for mafic and silicic volcanoes, which are used when historical information about a volcano is unavailable.

These eruption types and associated parameters can be used for ash-cloud mod-

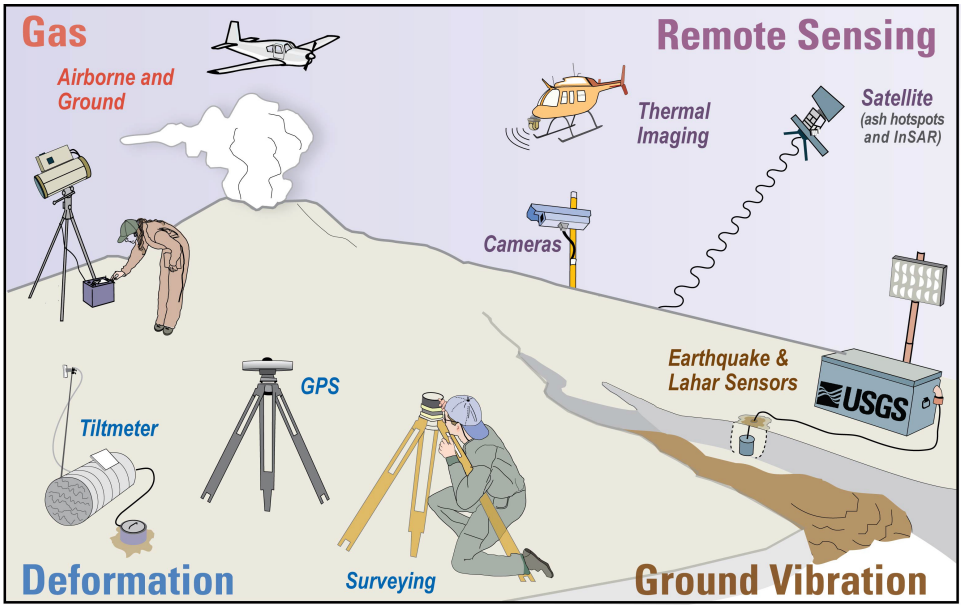

Figure 1.1: Volcanic monitoring types and methods employed by the USGS Volcano Hazards Program, taken from the following website: https://volcanoes.usgs.gov/vhp/monitoring.htmls

eling in the event of an eruption, when no observational constraints on these parameters are available.

1.4. Observations of volcanic ash

The monitoring of volcanic activities uses a variety of satellite-based, airborne and ground-based techniques, as illustrated in Fig. 1.1.

1.4.1. Satellite-based measurements

Current satellites provide unparalleled opportunities for the observation of volcanic ash and SO_2 with global coverage. They enable the retrieval of aerosol optical properties, such as the Aerosol Optical Depth (AOD), which can be transfered to a 2D ash-column (ash mass loading) field. There exists a broad range of satellite-borne instruments on various platforms in both Low Earth Orbit (LEO) and Geostationary Earth Orbit (GEO). The most prominent instruments used during the eruption of Eyjafjallajökull 2010 events were SEVIRI, AVHRR, MODIS and OMI (Prata and Prata, 2012; Prata, 2015; Christopher *et al.*, 2012).

The main requirements for an optimal satellite observing system are high temporal, spacial and spectral resolution. High temporal resolution permits to track the time evolution of volcanic ash cloud and to follow the continuity of the eruption process. High spatial resolution allows better characterisation of the volcanic plumes near the source for better initialising volcanic ash models. A wide spectral

range from UV to TIR can be exploited to retrieve the volcanic ash particles from fine (0.05 μm) to coarse (15 μm) and SO_2 (Prata *et al.*, 2014). SO_2 can be used as proxy for volcanic ash (Thomas and Prata, 2011).

However, many sensors have limited temporal coverage. Shortwave (UV and visible) sensors can only observe during daylight. There are passive and active sensors. The observations from passive sensors are hampered by clouds, and they are typically presented in column integrated values which hardly have any vertically resolved quantitative information. Satellite carrying lidars can measure at night and are less hampered by clouds than passive sensors, but observe only along a fixed line of sight (Winker *et al.*, 2012).

1.4.2. Ground-based measurements

Ground-based lidars, ceilometers, photometers and microwave radars provide observations for plume probing. A key element in understanding aerosol-related processes and transport are vertical profiles of aerosol parameters, which have been recorded since many years by lidar networks like EARLINET. Ground-based lidars can be used to monitor the aerosol dispersion in the low and middle troposphere. As a supplement to the 2D AOD fields provided by satellite observations, they provide observations of long-range transport, detailed information of plume height, vertical extent and vertical structure of the plume (Mona *et al.*, 2012; Flentje *et al.*, 2010; Ansmann *et al.*, 2010). These information allows a much better construction of the initial ash plume for the VATD models.

Ground-based weather radar systems are able to monitor 24-hours a day, in all weather conditions, with high spatial resolution and within few minutes after the eruption. The fast response is crucial to monitor the "near-source" eruption from the early-stage near the volcano vent, dominated by coarse ash and blocks, to the ash-dispersion stage up to hundreds of kilometers, dominated by transport and evolution of coarse and fine ash particles. For distances larger than about several tens of kilometers fine ash might become "invisible" to the radar (Marzano *et al.*, 2011). Active microwave remote sensing, through ground-based scanning weather radars, can be better exploited and can represent a very powerful, and to some extent, unique instrument to study explosive eruptions in proximity of volcanic vents (Harris and Rose, 1983; Lacasse *et al.*, 2004; Marzano *et al.*, 2006b; Gouhier and Donnadieu, 2008). In the 'near-source' region weather radars may in principle be, capable to provide data determining, not only the plume height, but also ash particle category, ash volume, ash fall-out and ash concentration (Marzano *et al.*, 2006a)

In addition, if available, webcams can provide a live video stream and allows viewers to get a better sense of the conditions near the volcano.

1.4.3. In-situ measurements

Aircraft measurements provide data directly along the flight path and with other methods to determine the height as well as the vertical extent of the ash plume. Newly-developed aircrafts have been specially designed to be allowed for the flight in the outskirt of the ash cloud with low ash concentration. They carried particle

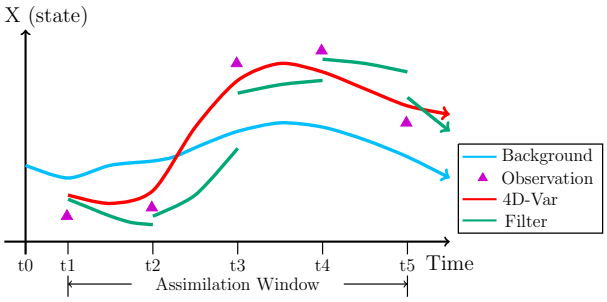

Figure 1.2: Comparison between kalman filter approach and 4D-Var approach.

counters which provide in-situ observations with high accuracy about particle sizes and the size distribution (Weber *et al.*, 2012).

Weather balloons have been enhanced to be able to acquire the information of where it is potentially dangerous to aircraft (Petäjä *et al.*, 2012). The balloons can carry instruments which measure the particle size and concentration using a miniature laser system. They provide detailed information on the ash plume position, extent and structure. The balloon system can also report its position using GPS. However, the route of balloon flight is determined by the local weather condition (wind).

1.5. Data assimilation

Data Assimilation (DA) has been used in atmospheric chemistry models for many decades to improve the air quality forecasts, reanalyze and reconstruct the 3D chemical concentrations, and estimate the model parameters or inputs. Coupled with the VATDs, data assimilation offers the possibility to improve the estimation of the eruption source inputs and the ash cloud forecasts,

The most commonly used DA approaches can be divided into two categories: filtering approaches and variational approaches. The former estimate model state sequentially by assimilating the observations up to this time (Evensen, 1994; Houtekamer and Mitchell, 1998; Burgers *et al.*, 1998; Whitaker and Hamill, 2002; Zupanski, 2005). The latter minimize a cost function which quantifies the difference between the model results and observations (Dimet and Talagrand, 1986; Penenko, 2009; Penenko *et al.*, 2012). 4-Dimensional Variational (4D-Var) approach benefits from the flow dependence in the statistics by incorporating observations over a period. Comparison between filtering approach and 4D-Var is shown by Fig. 1.2.

Both approaches have been successfully used for conducting air quality assessments or improving the accuracy of the forecast. The best known chemical species in the atmosphere to be calibrated include ozone (O_3), carbon monoxide (CO), nitrogen dioxide (NO_2), and aerosols/particular matter (PM). For instance, columns and vertical profiles retrieved from satellite data tracing gas of the above species were assimilated into stratospheric Chemical Transports Models (CTMs) (Errera and

Fonteyn, 2001) and tropospheric CTMs (Elbern *et al.*, 1997). DA approaches have also been used for multiple purposes. For instance, they can be used to reproduce air pollutant concentration maps (Elbern and Schmidt, 2001), to improve boundary conditions (Roustan and Bocquet, 2006) and model parameters (Bocquet, 2012; Jackson *et al.*, 2004; Barbu *et al.*, 2009; Tong and Xue, 2008), to identify model error and observation bias (Zupanski and Zupanski, 2006; Fertig *et al.*, 2009; Dee and Da Silva, 1998), and to estimate emissions (Yumimoto and Uno, 2006; Hakami *et al.*, 2005; Konovalov *et al.*, 2006).

For the concern of the estimation of model parameters and emissions, they provide two different types of solutions. These two approaches provides different types of solution in the estimation of model parameters or emissions. The filter approach requires the augmentation of the system state with the parameters (Ruiz *et al.*, 2013). The variational approach is preferable in these applications since the parameters can be accounted for in the cost function Penenko (2009); Penenko *et al.* (2012); Elbern *et al.* (2007); Bocquet (2012). 4D-Var approach, whose cost function is defined in both space and time, can be used to estimate emission rates either through a location-dependent scaling factor or/and arbitrary emission forcing restricted to a single point source Bocquet *et al.* (2014). The former has been used for optimization of emission inventories of anthropogenic or natural pollutants Meirink *et al.* (2008); Elbern *et al.* (2007); Strunk *et al.* (2010); Yumimoto *et al.* (2012); Vira and Sofiev (2012). The latter can be developed to source term estimation in volcanic eruptions (Lu *et al.*, 2016a).

1.6. Objectives and outline

The eruptive parameters or the emission source is critical on the forecasts of volcanic ash clouds, however, those parameters are either unable to be observed directly or poorly observed. More accurate estimation of the ash emission are required. Data assimilation using available observations is a possible solution. Among all means of measurements, the most powerful and generally used are satellite observations. This thesis aims at reconstructing the vertical profile of volcanic ash emissions using satellite ash mass loading data using a variational assimilation approach.

The potential of 4D variational approach for volcanic ash assimilation has been tested, which turns out to be failed in the estimation of the mass vertical structure. A series of scientific questions occur:

- What are the causes that 4D-Var is incapable of estimating the volcanic ash emissions using satellite-retrieved ash columns?
- Can we develop an alternative 4D-Var approach for this application?
- Can we use the SEVIRI satellite ash products to produce a more accurate estimate of the emission and a better forecast?
- Are there any criteria or soring rules that are able to predetermine whether the variational approach would work for a specific application instead of verifying the assimilation results by conducting the assimilation?

The content of the thesis is organized following the structure imposed by the questions, as a collection of the published work. In order to conduct experiments, a validated VATD model is required. The LOTOS-EUROS model is used by including the volcanic ash eruptive source parameters and generating an ash column as the emission input. The model is adapted to volcanic ash transport by adjusting the parameters in the advection and deposition processes. Description and validation of the model for this application based on a case study are given in Chapter 2.

In Chapter 3, 4D-Var approach is introduced to assimilate ash-column data for the estimation of volcanic ash emissions, which is shown to be unable to reconstruct the vertical structure of the emissions.

In Chapter 4, an alternative method termed 'trajectory-based 4D-Var (Trj4DVar)' is proposed. The derivation of the methodology and the details of the algorithm are presented. The method is tested in twin experiments using both a perfect model and a stochastic model. The latter is done to test how Trj4DVar deals with uncertainties of the observations. Comparisons are made against the experimental results of using standard 4D-Var.

Trj4DVar does not always guarantee an accurate reconstruction of the plume height, which is a critical parameter for the quality of the forecast. This motivates the assimilation of ground-based observations of plume heights in Chapter 5. Modifications of the Trj4DVar with different control strategies are proposed to this end. Results of twin experiments using modified Trj4DVar show that the method is capable of correctly estimating the plume heights, which largely improves the forecast quality and reliability compared to that of using straightforward Trj4DVar.

In Chapter 6, field data from the geostationary satellite instrument - SEVIRI and observations of plume heights from ground-based weather radar - IMO are put into use to explore the potential of applying Trj4DVar in real case. Pre-processing of satellite data and guidance on the proper use of it are provided in this chapter. Investigations of the influence of the assumptions on the observational uncertainty to the assimilation outcomes are carried out.

Chapter 7 gives a in-depth and comprehensive analysis of the ill-conditioned problem occurred when using standard 4D-Var for this application. Evaluation criteria on the quality of assimilating remote-sensing data using gradient-based (variational) assimilation approaches are presented based on the analysis. These criteria are validated to quantitatively evaluate the effectiveness of the assimilation process and the reliability of the forecast, and can be further used to adjust configuration of the assimilation system

Finally, Chapter 8 presents the conclusions and outlook of the thesis.

2

LOTOS-EUROS: modelling of volcanic ash cloud

This chapter mainly describe a new functionality within the LOTOS-EUROS model that allows the simulation of emission, transport (including advection and dispersion), and sedimentation of volcanic ash released during volcanic eruptions. A preprocessor tool produces a vertical ash column at the model pixel nearest to the volcano locations, based on eruption source parameters such as plume height and total emission rate, as well as additional information of timing and durations. Using this emission source, the LOTOS-EUROS model can realistically simulate transport and sedimentation of the ash cloud using its own dynamics. Parameterizations of some physical procedures are adapted. Model validation is carried out based on the case study of the 2010 Eyjafjallajökull eruption in Iceland. Comparisons about ash fall and movement of ash clouds are made, and show good matches with simulations of other VATDs and observations.

2.1. Introduction

Volcanoes can inject large volumes of ash into the atmosphere, which will pose a threat to international and domestic airspace and disrupt local communities (Casadevall, 1992; Tuck and Huskey, 1994; Casadevall, 1994). Volcanic ash typically contains fine-grained rock, glass shards, and mineral fragments. Volcanic Ash Transport and Dispersion (VATD) models play an important role in forecasting the movement of volcanic ash clouds to provide hazard mitigation and timely warnings for the concern about aviation safety.

Several VATD models have been developed for ash falling to low levels. Carey and Sigurdsson (1982) simulated the aggregation and deposition behavior from a dispersion ash plume. Hopkins and Bridgman (1985) modeled the transport and deposition of the ash particles to determine the ground-level fallout along a centerline. Suzuki (1983) used a 2D turbulent diffusion equation to calculate ground-based ash concentrations and the model was modified by Glaze and Self (1991) to account for vertical wind shear. Carey and Sparks (1986) presented a theoretical model for clast ash fallout from convective eruption columns. There are also VATD models for the understanding and tracking of the airborne volcanic ash clouds, such as Emergency Response Model (Pudykiewicz, 1988, 1989), PUFF (Searcy *et al.*, 1998), Hybrid Single-Particle Lagrangian Integrated Trajectory (HYSPLIT) (Draxler and Hess, 1998), Numerical Atmospheric-dispersion Modeling Environment (NAME) (Jones *et al.*, 2007). Besides, new models can be developed by adding new functionality within the existing numerical gas and aerosol transport models, for instance, Stuefer *et al.* (2013) included a volcanic emission preprocessor in the Weather Research and Forecasting model coupled with Chemistry(WRF-Chem) to compute the initial volcanic ash and SO_2 plume.

In our study, the LOTOS-EUROS model (Schaap *et al.*, 2008) version 1.10 is adapted to model the transport of volcanic ash and to determine the location of ash clouds. This model is an operational air-quality model, used for daily air-quality forecasts over Europe (Curier *et al.*, 2012), focusing on ozone, nitrogen oxides, and particular matter.

This chapter is organized as follows. Section 2.2 describes the physical processes that are used in the modeling, and the parameters of some of the processes that are adjusted for this application. In Section 2.3, a volcanic ash plume model is presented to generate the emission source input. In Section 2.3, validations for the model as VATD are provided based on a case study. A brief summary is given in the last section.

2.2. Description of the LOTOS-EUROS model

The model adapted for volcanic ash is based on a discretization of the advection diffusion equation:

$$\frac{\partial \mathbf{c}_s}{\partial t} = -\nabla \cdot (\mathbf{u} \cdot \mathbf{c}_s) + \frac{\partial}{\partial \mathbf{v}} \left(\boldsymbol{\mu}_\mathbf{v} \frac{\partial \mathbf{c}_s}{\partial \mathbf{v}} \right) + \mathbf{E}_s - \mathbf{D}_\mathbf{s}(\mathbf{c}_s) \tag{2.1}$$

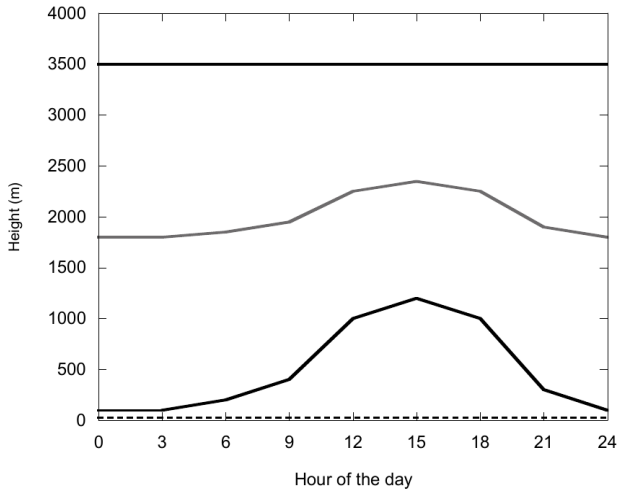

Figure 2.1: An illustration of the vertical grid system as function of the hour of the day, taken from LOTOS-EUROS manuscript.

where $\mathbf{c}_s$ is the 3D concentration field of the tracer gas or aerosol, or as in our study, volcanic ash. $\mathbf{u}$ is the wind velocity field. $\boldsymbol{\mu}_\mathbf{v}$ represents the vertical diffusion coefficients. The source and sink terms E and D account for emission and deposition, respectively.

The model domain in this study is bound at 45°N and 70°N, 30°E and 15°W. The grid resolution is 0.5° longitude $\times$ 0.25° latitude. There are 12 vertical layers, which contain a surface layer of 25 m, three dynamic layers with a top at 3.5 km Above Sea Level (ASL), and the rest are 1-km-thick layers to the top (see Fig. 2.1). The lowest dynamic layer represents the variable mixing layer with the height obtained from the meteorological input, and the upper two dynamic layers are reservoir layers with equal thickness and a minimum of 100 m.

The transport consist of 3D advection, horizontal and vertical diffusion. The advection is driven by meteorological data produced by European Centre for Medium-Range Weather Forecasts (ECMWF). This data provide wind fields in the 2 horizontal dimension, and the vertical wind speed is calculated by the model as a result of the divergence of the horizontal field. The system is solved highly-accurate, monotonic advection scheme by developed by Walcek (2000).

Deposition of particles follows Zhang (2001) deposition scheme(unless adapted), explicitly including particle size and sedimentation. The parameterization of particluar deposition has been adapted for tephra fallouts following Schwaiger *et al.* (2012).

2.3. Volcanic ash emission model

A volcanic plume model has been developed to generate the eruption ash column, which is represented by the term $\mathbf{E}_S$ in Eq. 2.1. The necessary parameters for the

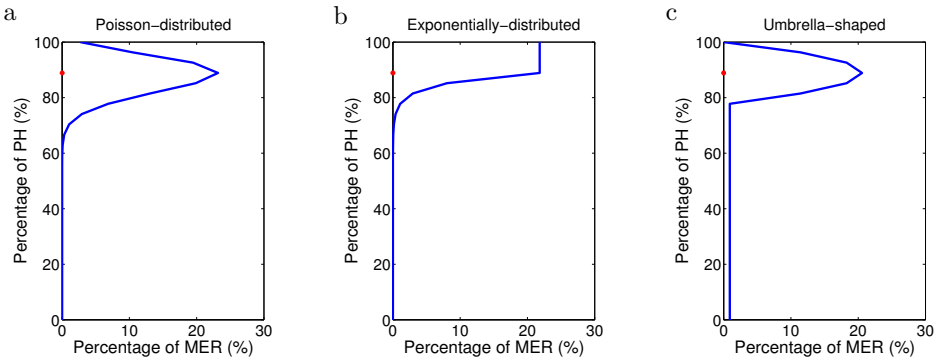

Figure 2.2: Vertical distribution of volcanic emission rates with a: Poisson-distributed; b: exponentially-distributed; and c: umbrella-shaped. The red dot represents the injection layer.

initial source information of the volcanic emissions include the mass eruption rate (MER), the plume height (PH), vertical distribution, and a grain size spectrum of the ash particles, as defined by Mastin *et al.* (2009b). Details of Mastin's ESP definition can be found in section 1.3.4. The volcanic emission generator provides the location of the volcano in the nearest model grid cell and the emission parameters (i.e. MER, PH and time duration) determined by the database developed by Mastin *et al.* (2009b). This default database can be used for the computation of the initial ash plume when no observations are available.

All parameters calculated from this database may be overwritten by the users once more accurate information is available. Ground-based observations from Lidar, weather radar, web-cam often provide PH H (m) that are more accurate than historical records. The total erupted mass rate M (kg s^{-1}) can be calculated using an empirical relationship according to Mastin *et al.* (2009b):

$$M = \rho(0.0005H)^{4.1494}, \tag{2.2}$$

where the variable ρ denotes the assumed magma density of 2600 kg m^{-3}. Note that the exponent of the power function (4.1494) and the multiplication coefficient (0.5) can be adapted to observations.

PH and MER are used within LOTOS-EUROS to determine the vertical distribution of the erupted mass. Large volcanic plumes are typically "umbrella" shaped (Sparks *et al.*, 1986; Koyaguchi, 1994; Sparks *et al.*, 1997), i.e. shaped as shown in Fig. 2.2c. Three types of vertical distribution, as shown in Fig. 2.2, are provided to generate this "umbrella-shaped" initial plume which can be modified by users. The first is Possion-distributed , where the percentage of the eruption rate is defined by probability density, the discrete random variable is the layer number, and the expected value is the injection layer at the injection height altitude. The second is exponentially-distributed, where values from the injection layer above are constant. The third is umbrella-shaped, where the cap containing 75% of the eruption mass is a parabolic function mirrored by the injection layer, and the base layers are uniformly distributed. The injection height with maximal emission rate is assumed to be

Table 2.1: Volcanic ash particle size distribution corresponding to LOTOS-EUROS ash bins variable names; the mass fractions in percentage of total mass are given for each ESP eruption type M0-M3 and S0-S9.

Bin Vars	vash_1	vash_2	vash_3	vash_4	vash_5	vash_6
Par Dia (μm)	250 - 2000	63 - 250	30 - 63	10 - 30	2.5 - 10	< 2.5
M0	37.3	56.8	3.0	2.0	1.0	0.0
M1	14.0	84.0	2.0	0.0	0.0	0.0
M2	37.3	56.8	3.0	2.0	1.0	0.0
M3	60.5	29.5	4.0	4.0	2.0	0.0
S0	31.0	29.5	12.0	15.0	10.5	2.0
S1	69.0	21.0	4.3	3.9	1.7	0.3
S2	31.0	29.5	12.0	15.0	10.5	2.0
S3	18.3	16.1	13.0	28.3	23.1	5.6
S8	18.3	16.1	13.0	28.3	23.1	5.6
S9	0.0	31.0	23.0	30.0	16.0	0.0

roughly located at 87% of the plume height.

It is evident that the total mass strongly depends on accurate injection heights according to the empirical relationship (2.2). However, injection heights can vary frequently during the eruption, and the forecasts for the location and concentration of the ash cloud are very sensitive to these parameters. In this thesis, data assimilation methods are developed to improve the accuracy of the modeled state of the atmosphere and its emission when more observations are available besides plume heights. The emission ash column can be renewed by the estimates.

The volcanic ash particles can be describes in terms of particle number per size bin. Here we use 6 different bins representing the diameters of the particles typically ranging from a few micrometers up to two millimeters. A look-up table has been developed based on literature for particle size distribution as illustrated by Tab. 2.1. This table gives the mass fraction in percentage of total mass for ESP eruption type M0-M3 and S0-S9, which is derived from the analysis of of ash samples mostly from the example eruptions listed in Tab. 1.2 (see section 1.3.4) provided by Bonadonna *et al.* (2002b); Bonadonna and Houghton (2005); Scollo *et al.* (2007); Rose *et al.* (2008); Durant and Rose (2009); Durant *et al.* (2009). This option is useful if it is important to predict ashfalls with reasonable accuracy. For a simple long-range forecast, the use of the fine ash ($< 63\mu$m in diameter) is enough to simulate the distal part of ash cloud and provide information for aviation safety.

2.4. Modeling of volcanic ash clouds and validation

The volcanic ash simulation with the LOTOS-EUROS model has been applied to based on a case study of the 2010 Eyjafjallajökull eruption event. The initial volcanic plume is calculated with PH derived from the local weather radar station (IMO, 2010), an MER according to Eq. 2.2, Poission-distributed vertical profile and a particle size distribution shown in Tab. 2.3 adjusted from S2 ESP type (compare

Table 2.2: Input parameters for April 14-19, 2010 period of activity at Eyjafjallajökull (Webley *et al.*, 2012).

Start Time (UTC)	Duration (hour)	Height (km a.s.l.)	Eruption Rate (m^3 s^{-1})	Eruption Rate (kg s^{-1})
4/14/2010 09:00	10	9	219.553	$5.71e+05$
4/14/2010 19:00	9	5.5	14.884	$3.87e+04$
4/15/2010 04:00	39	6	199.503	$6.44e+04$
4/16/2010 19:00	35	8.25	140.325	$3.65e+05$
4/18/2010 06:00	17	5	8.335	$2.17e+04$
4/18/2010 23:00	1	4	1.898	$4.93e+03$

Table 2.3: Volcanic ash particle size distribution and ash bins property for LOTOS-EUROS model simulation. Fine ashes categorized in vash_4 to vash_6 are used to compare model simulations and satellite observations.

Bins	Particle Diameter	Percent of Mass	Average Particle Size (μm)
vash_1	250 to 2000 μm	29	1125.00
vash_2	63 to 250 μm	31	156.50
vash_3	30 to 63 μm	12	46.50
vash_4	10 to 30 μm	18	20.00
vash_5	2.5 to 10 μm	8	6.25
vash_6	0.0 to 2.5 μm	2	1.25

to Tab. 2.1). The emission information of explosive eruption from 14 April, 00:00 UTC for 5 days until 19 April, 00:00 UTC is taken from Webley *et al.* (2012) and shown in Tab. 2.1. The 3D volcanic ash concentrations are described by the 6 tracers following Tab. 2.3. The transport processes include advection, diffusion, sedimentation, and dry and wet depositions as described in section 2.2.

LOTOS-EUROS simulations show that wind patterns first transported the ash cloud to the northeast of Iceland, then turned the cloud's main trajectory to the southeaster toward mainland North-Western Europe and the United Kingdom (April 15, 2010 at 00:00 UTC, Fig. 2.3(a)). In the further forecast, the ash dispersed further over Europe and to the east towards northern Russia, then shifting winds across the United Kingdom and over the North Atlantic during the following days (April 17, 2010 at 00:00 UTC, Fig. 2.3(b)).

LOTOS-EUROS simulated results are compared with forecasts modeled by Weather Research Forecast coupled with Chemistry (WRF-Chem) and provided by Volcanic Ash Advisory Center (VAAC), shown in Fig. 2.3. The ash mass loadings in Fig. 2.3 for comparison against other model outcomes, include all the volcanic ash mass from volcanic ash particle size bin 1 (0.25 to 2 mm diameter) to volcanic ash bin 6 (less than 2.5 μm). The WRF-Chem has been validated as a proper VATD model, and its simulated snapshots (Figs. 2.3(c)-(d)) are taken from Webley *et al.* (2012). By comparing Figs. 2.3(a)-(b) against Figs. 2.3(c)-(d), respectively, we

can see that LOTOS-EUROS simulations match the WRF-Chem forecasts in the same time period.

VAAC are established by the International Civil Aviation Organization (ICAO), to provide information to the aviation community through timely Volcanic Ash Advisories (VAA) based on NAME modeled forecast. VAAC provides figures that show contour boundaries of ash concentrations of 200 μg m^{-3} at specific altitude bounds. 200 μg m^{-3} is low valued limitation of aviation safety (Zehner, 2012). Comparison of NAME model to other models is to compare superposition of ash cloud locations over all the altitude bounds to the boundaries of ash mass loadings. LOTOS-EUROS forecasts show a good agreement with VAAC outcomes, comparing Figs. 2.3(a)-(b) against Figs. 2.3(e)-(f), respectively,

Volcanic ash concentration maps from each individual bin illustrate the ability of the model to deal with the dispersion and settling processed for different particle sizes (at 00:00 UTC on April 17, 2010, Fig. 2.4). Figs. 2.4(a)-(b) show that large particles with diameter $>$ 63 μm from bins 1-2 were not advected beyond 120 km from the volcano. This is consistent with the conclusions of Schneider *et al.* (1999) and Rose *et al.* (2001). Schneider *et al.* (1999) showed particles in diameter $>$ 50 μm would have residence time of less than 5 hours given spherical particles falling out of a 20 km ASL initial plume and Rose *et al.* (2001) stated that particles of $>$ 500 μm in size would fall out rapidly within 0-12 hour after emission, within 25 km of the volcano. Figs. 2.4(c)-(f) show the ash particles from bins 3-6 dominated the dispersing ash cloud, which propagated across Northern Europe (Northern Scandinavia).

In addition, satellite observations are also used to aid in confirming the LOTOS-EUROS-predicted volcanic ash clouds, shown by Fig. 2.5. These observations are ash mass loadings retrieved by Prata and Prata (2012) from Spinning Enhanced Visible and Infrared Imager (SEVIRI) data. The SEVIRI data confirmed the presence of the volcanic cloud propagated towards (April 15, 2010 at 12:00 UTC, Fig. 2.3(c)) and situated overhead at (April 15, 2010 at 17:00 UTC, Fig. 2.3(d)) northern Russia. Figs. 2.3(a)-(b) show that the ash-dense part (in red) of the modeled ash clouds have similar shapes and positions as SEVIRI observations at the same time.

2.5. Summary and conclusions

A volcanic ash plume module has been added to the LOTOS-EUROS model. It generates eruption sources in an ash column above the volcano as input in three stages. In stage one: this module can produce a default emission for a certain eruptive type based on historical data for the initial release when no observations are available. The calculation of the emission are made using a definition of eruption source parameters, which are given in a look-up table. The default parameters are those compiled by Mastin *et al.* (2009b) from historical eruptions. In stage two: the module is able to calculate a new emission using observed eruptive source parameters. Usually the plume height and mass eruption rate can be updated, and the latter is computed by using observations of the former. In stage three: an estimate of the eruption ash column can be obtained through data assimilation using more observations besides the source parameters. The application of data

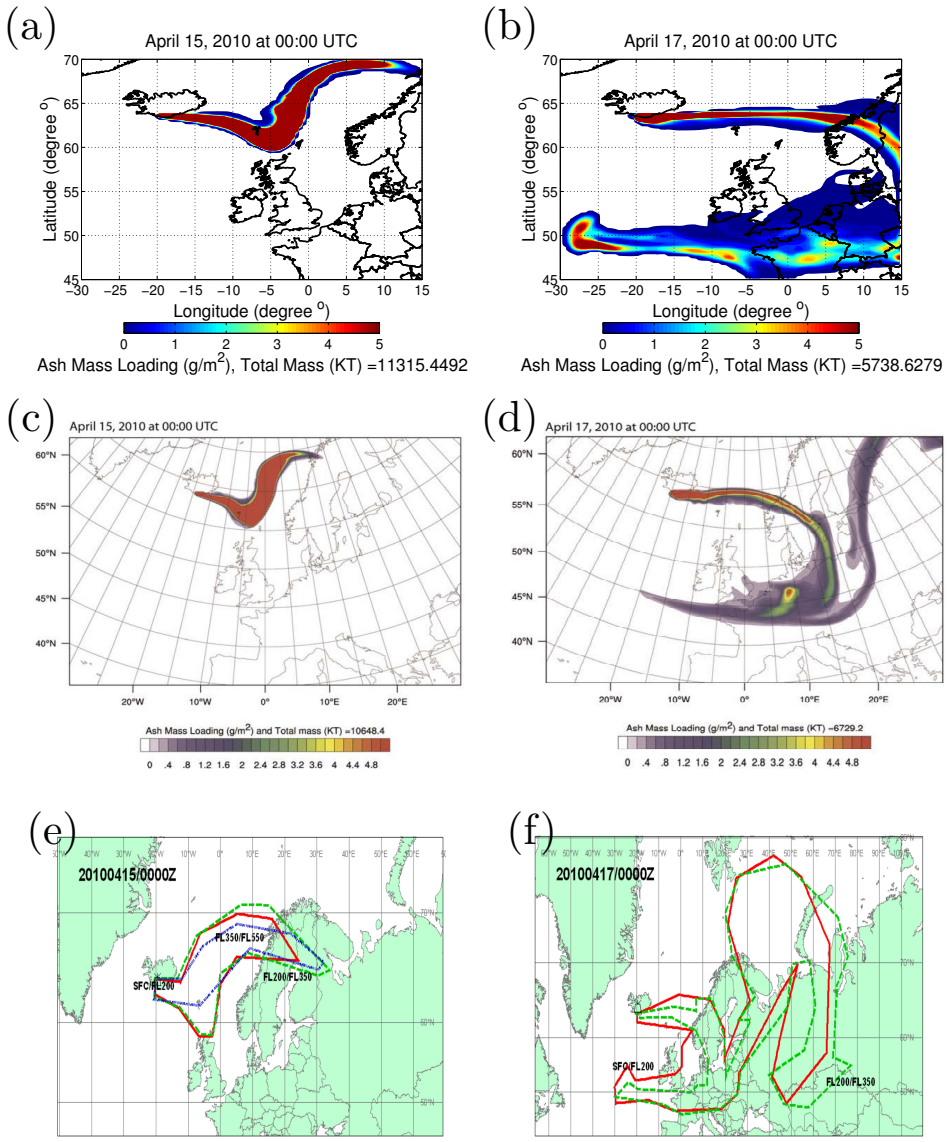

Figure 2.3: LOTOS-EUROS model simulation results compared with WRF-Chem forecasts and VAAC forecasts. In the top row there are the time snapshots from LOTOS-EUROS model simulations of April 14-19, 2010 volcanic ash clouds from Eyjafjallajökull volcano at (a) 10:00 UTC on April 15; (b) 00:00 UTC on April 17. The middle row are the corresponding WRF-Chem forecasts at (c) 00:00 UTC on April 15; and (d) 00:00 UTC on April 17. The bottom row are the corresponding VAAC forecasts at (e) 00:00 UTC on April 15; and (f) 00:00 UTC on April 17.

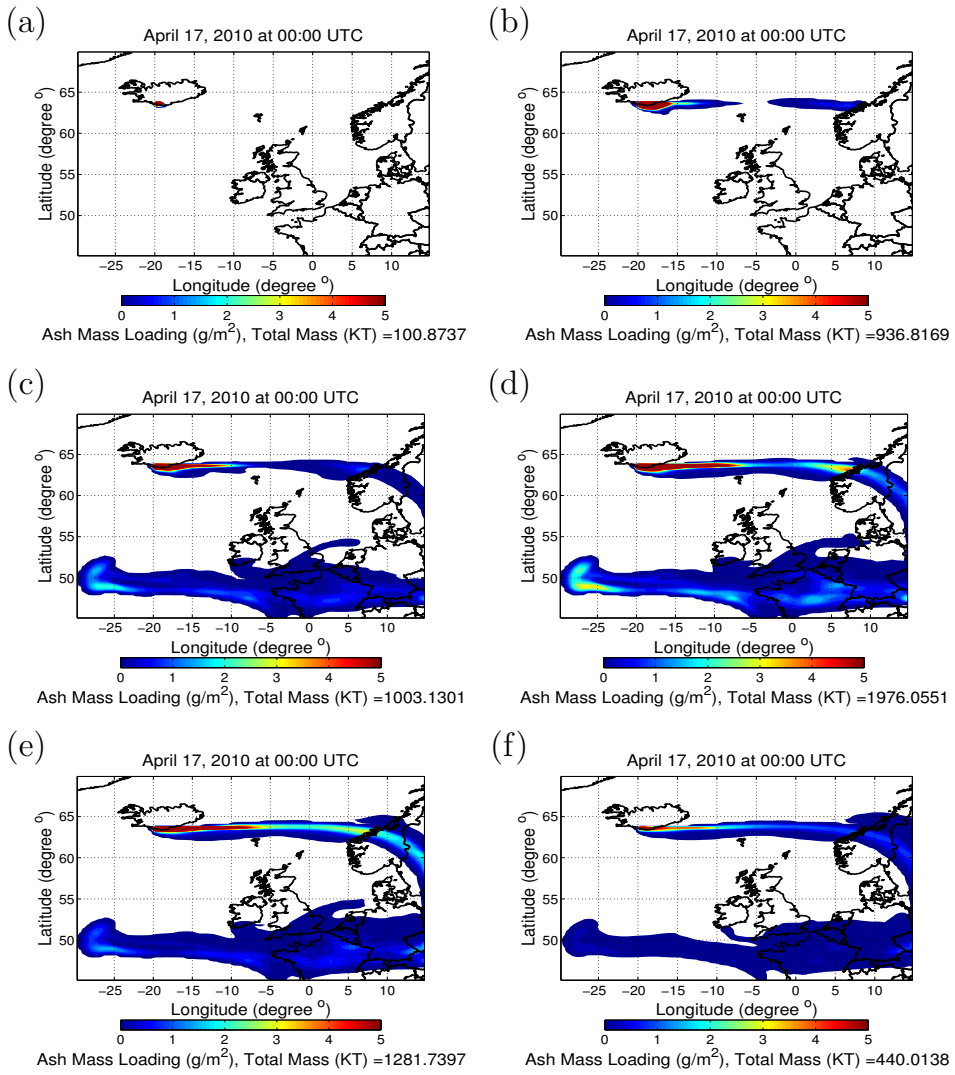

Figure 2.4: LOTOS-EUROS simulations with ash bin (a) vash_1, (b) vash_2, (c) vash_3, (d) vash_4, (e) vash_5 and (f) vash_6.

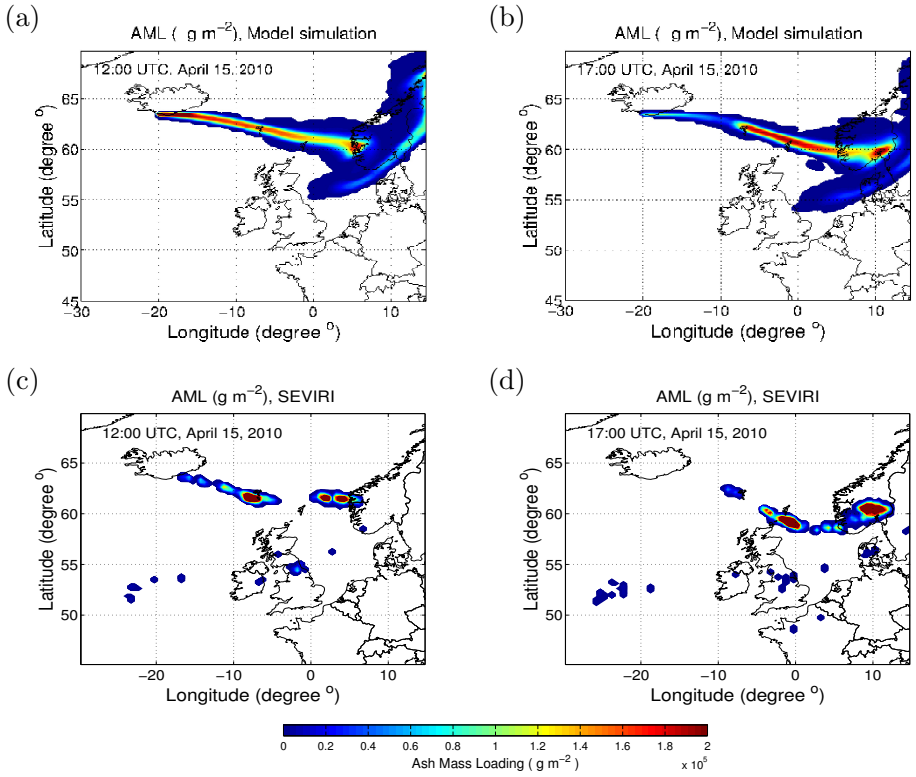

Figure 2.5: LOTOS-EUROS simulated results at (a) 12:00 UTC; and (b) 17:00 UTC; compared against SEVIRI retrieved ash mass loading fields at (c) 12:00 UTC; and (d) 17:00 UTC, on April 15, 2010.

assimilation is the subjects of the next chapters.

The ash tracers in the model are categorized by their diameter according to particle size distribution into 6 bins. The size distribution is given by 11 default eruption types, and can be further adjusted using observations of ash fallout. The trajectories of ash in each bin can be computed independently as tracers from coarse mode to fine mode. The physical processes include advection, diffusion, sedimentation, and wet and dry deposition. The parameters for the depositions are adapted for the prediction of ash falls according to historical database and parameterization study of tephra sedimentations. Removal processes for aggregation, evaporation and resuspension have not yet been taken into account, and might be included later.

The model simulations have been validated as capable to provide quantitative forecasts on volcanic ash air-borne concentrations. The validation was made using the example of Eyjafjallajökull 2010 eruptions in Iceland. The model simulations have been compared and showed a good match with the simulations from other VATDs such as NAME and WRF-Chem and real data. The shapes and locations of ash clouds were in good agreement with those obtained from the SEVIRI retrievals. The LOTOS-EUROS model can now be used for the next step of this study - the assimilation of data and calibration of some of the parameters.

3

Standard 4D-Var and its application in volcanic ash problem

The forecast of the location and movement of volcanic ash clouds depends largely on the eruption source parameters, especially the plume height and vertical structure. 4-dimensional variational data assimilation (4D-Var) approach is used to estimate the ash emissions from 2D ash column observations combining the LOTOS-EUROS simulations. In general, it is beneficial to use variational data assimilation for the estimation of aerosol pollutant emissions. However, the trial for our case shows that the 4D-Var fails to reconstruct the vertical profile of volcanic ash emissions or improve the forecast of ash concentrations. Twin experiments are conducted to illustrate this fact, using simplified LOTOS-EUROS model and synthetic satellite observations. The ill-posed nature of this problem is analyzed to provide an inspiration to solve the problem.

Parts of this chapter have been published in:
Lu, S.*, Lin, H.X., Heemink, A.W., Fu, G., and Segers, A.J. (2016). Estimation of Volcanic Ash Emissions Using Trajectory-Based 4D-Var Data Assimilation. ***M*onthly Weather Review** 144, 575-589, 2016.

3.1. Introduction

Volcanic eruptions lead to the release of greenhouse gases, ashes, and chemicals that influences climate (Robock, 2000). Volcanic ash impacts respiratory health of human beings, and can cause acute and chronic diseases (Horwell and Baxter, 2006). People in a wide area covered by extensive ash fallout will be affected, and undertake long term health risk after ash falls. Despite of relatively rapid settling process of large particles (Rose *et al.*, 2001), fine particles with small radius can float in the atmosphere for a long time, transport and spread out in a continental domain. Airborne ash, containing silicate which can melt in the engines and cause devastating risk to jet planes, could affect commercial and military air operations, and disturb local economy (Casadevall, 1994). Therefore rerouting and cancellation is necessary according to hazard assessment.

Volcanic ash forecasting is a crucial tool in hazard assessment and operational volcano monitoring. Analysts use volcanic ash transport models to determine the future location of ash clouds. Besides, validated atmospheric transport models which are capable of modeling the physical behavior of volcanic ash transport and dispersion process, accurate estimation of emission source terms is needed in order to obtain reliable prediction results. However, the source parameters, such as total mass of eruption products and the altitude at which they are effectively released into the atmosphere, are hardly known. Thus, the source term, which usually appears in forms of vertical distribution of emission rates in an aerosol transport model, must be accurately estimated.

Therefore, systematic and automatic estimation approaches are needed to correct emission parameters and improve forecast accuracy. In this chapter the use of data assimilation (DA) is considered. DA techniques have been successfully applied to meteorology and oceanography, to produce improved model states forecast or model parameters, by combining model and observations. There are two main categories of modern DA approaches, filtering (Evensen, 1994) and variational methods (Dimet and Talagrand, 1986). The former is a class of sequential methods, which seeks a balance between prior model states and observations by minimizing the updated error covariance matrix. The latter search an optimal set of parameters by minimizing a cost function measuring the difference between the model outputs and observations.

Both approaches have been successfully used for estimating the state space variables on the purpose of conducting air quality assessments or of improving the initial condition for a better forecast. The best known chemical species in the atmosphere to be celebrated include ozone (O_3), carbon monoxide (CO), nitrogen dioxide (NO_2), and aerosols/particular matter (PM). For the concern of the estimation of model parameters and emissions, they provide two different types of solutions. These two approaches provides different types of solution in the estimation of model parameters or emissions. The filter approach requires the augmentation of the system state with the parameters (Ruiz *et al.*, 2013). The variational approach is preferable in these applications since the parameters can be accounted for in the cost function Penenko (2009); Penenko *et al.* (2012); Elbern *et al.* (2007); Bocquet (2012). 4D-Var approach, whose cost function is defined in both space and time,

can be used to estimate emission rates either through a location-dependent scaling factor or and arbitrary emission forcing restricted to a single point source Bocquet *et al.* (2014). The former has been used for optimization of emission inventories of anthropogenic or natural pollutants Meirink *et al.* (2008); Elbern *et al.* (2007); Strunk *et al.* (2010); Yumimoto *et al.* (2012); Vira and Sofiev (2012). The latter can be developed to source term estimation in volcanic eruptions.

The number of applications of 4D-Var on volcanic ash problem is quite limited. Valdebenito *et al.* (2010) assimilated the PM mass concentrations near the surface with observations provided by Dutch stations, and corrected the PM mass concentrations in other places according to the correlation between the observed state variables and the unobserved ones. The emission rates were adjusted through experience (so not using systematic approach) by comparison of AOD values with the simulated model forecasts and the retrievals from satellite instruments. Due to the insufficiency of in-situ observations, and the small correlation between the state variables at the surface layer and the ones at higher layers, the estimation of volcanic ash concentrations at higher layers remains unreliable. Accurate estimation of volcanic ash cloud at higher altitudes is critical for aviation hazard information, which needs a more sufficient observation sets and an systematic way to assimilate them.

The 4D-Var with a standard cost function is tested for the optimization of volcanic ash emissions using observations provided by the powerful monitoring tool - satellite. The experimental outcomes shows that standard 4D-Var is not able to accurately estimate vertical distribution of effective volcanic ash injection rates from ash columns. In this chapter, this problem will be illustrated and analyzed both theoretically and experimentally.

This chapter consists of the following topics. Section 3.2 gives an overview of 4D-Var approach. Section 3.3 explains theoretically how an ill-conditioned situation occurs which results in ineffective estimates. In section 3.4, twin experiments are carried out for the demonstration of the ill-conditioned problem and its influence on the assimilation results. Section 3.5 summarizes the chapter.

3.2. 4D-Var approach

Variational methods determine an optimal combination of the prior information and observation data over an assimilation period by minimizing a cost function to estimate the control variables of a model. Control variables can include both state variables and system parameters, and in our case (total column observations to estimate volcanic ash emissions) they are the input of the system. A typical cost function would be the sum of the squared deviations of the analysis values from the observations weighted by the accuracy of the observations, plus the sum of the squared deviations of the background fields and the analyzed fields weighted by the accuracy of the background parameters. The cost function of Four-Dimensional Variational data assimilation (4D- Var) is defined in space and in time.

In our case, suppose the volcanic ash model can be mathematically represented

in forms of:

$$\mathbf{x}_k = M_k(\mathbf{x}_{k-1}, \mathbf{u}_k + \mathbf{w}_k), \tag{3.1}$$
$$\mathbf{y}_k = H_k(\mathbf{x}_k) + \mathbf{v}_k. \tag{3.2}$$

The subscript k represents time t_k. $\mathbf{x}_k \in R^n$ is the state vector; in volcanic ash transport model, this contains ash concentrations defined in a 3D array of grid cells. $\mathbf{u}_k \in R^p$ is the parameter vector including model parameters, inputs and initials. Here $\boldsymbol{u}_k$ is defined as the volcanic ash emission rate in a column as input to the model, which comprises the emission rates at p vertical layers above the summit. Vector $\mathbf{y}_k \in R^q$ contains the observations. The noise terms $\mathbf{w}_k$ and $\mathbf{v}_k$ represent the model and observation uncertainty respectively, both in terms of a Gaussian distribution with covariance matrices $\mathbf{B}_k$ and $\mathbf{R}_k$ respectively, where the model uncertainty lies in the parameter in this case. $M_k \in R^{n\times n}$ is the eventually transport model. Observation operator $H_k \in R^{q\times n}$ projects the state space into observation space; the inverse observation operator H_k^T that will be used in 4D-Var projects the observation space into the state space.

Once the observations are obtained, 4D-Var data assimilation can be carried out to seek optimal initial states and parameters which minimize the following cost function over an assimilation window $[t_0, t_N]$:

$$\begin{aligned} J(\mathbf{U}) &= \frac{1}{2}\sum_{k=0}^{N}\left(\mathbf{u}_k - \mathbf{u}_k^b\right)^T \mathbf{B}_k^{-1}\left(\mathbf{u}_k - \mathbf{u}_k^b\right) + \frac{1}{2}\sum_{k=0}^{N}\left(\tilde{\mathbf{y}}_k - \mathbf{y}_k\right)^T \mathbf{R}_k^{-1}\left(\tilde{\mathbf{y}}_k - \mathbf{y}_k\right) \\ &= J^b + J^o, \end{aligned} \tag{3.3}$$

where $\tilde{\mathbf{y}}_k = H_k(\mathbf{x}_k)$, and $\mathbf{U} = [\mathbf{u}_0, \cdots, \mathbf{u}_k, \cdots, \mathbf{u}_N]$. The model described by Eq. (3.1)-(3.2) is regarded as constraints to the minimization problem Eq. (3.3).

The solution of the minimization problem could be obtained using gradient-based methods (conjugate gradient, quasi-Newton, etc.), which are iterative methods by updating the parameters based on the gradients of the cost function with respect to the parameters. The adjoint model is usually required for the computation of the gradient (Talagrand and Courtier, 1987; Courtier and Talagrand, 1987). The incremental 4D-Var method has been developed to accelerate the solution process of nonlinear problems (Courtier *et al.*, 1994). However, no matter how advanced the approach is, the key point lies in how accurate the gradient represents the perturbations of parameters. When the gradient cannot represent the perturbations, it will never converge to the correct solution, as will be illustrated for the volcanic ash application in the next section.

3.3. The ill-posed nature of the problem

The standard 4D-Var has been successfully applied in air quality applications (Elbern *et al.*, 2000), including source estimation (Elbern *et al.*, 2007; Meirink *et al.*, 2008). However, estimation of vertical distribution of ash emission rates from satellite data is problematic. Infrared satellite instruments from which aerosol optical

depth (AOD) is retrieved only provide information on total column ash loadings. The instruments provide effective particle radius and AOD (τ) of volcanic ash clouds (Prata, 1989). The column mass loading (Ω) (or $\mathbf{y}_k$ in Eq. (3.2)) is related to τ by $\Omega = 4\rho r_e \tau/(3Q_e)$, where ρ is the aerosol mass density at ambient relative humidity, r_e is the column averaged effective radius and Q_e is the column averaged extinction efficiency with 40%-60% (Wen and Rose, 1994; Fu *et al.*, 2015). To transfer the ash concentrations $\mathbf{x}_k$ to ash mass loadings $\mathbf{y}_k$ (in Eq. (3.1)-(3.2)) the observation operator is in the following form:

$$H_k(\mathbf{x}_k) = \sum_{l=1}^{Nz} \omega^l * \mathbf{x}_k^l . * \Delta\mathbf{h}^l, \tag{3.4}$$

where Nz is the number of the vertical layers, $.*$ denotes the element-wise multiplication, $\mathbf{x}_k^l$ and $\Delta\mathbf{h}^l$ represent the states and thicknesses of the all grid cells in the l^{th} layer, respectively, and ω^l is the weighing factor of the l^{th} layer corresponding to mass extinction and the sensitivity of the specific satellite instrument with respect to height (Pierce, 2013).

Since in this way the satellite observation computes the vertical integral of state variables along a column and has no vertical resolution, it is difficult to distinguish which of the vertical emissions could explain a mismatch between the model and the observation. This results in invalid gradients for the parameter update, and the ill-conditioning issue in the optimization process.

To explain how the invalid gradients are formed, first the concept of Sensor-Induced Correlation (SIC) is introduced which is created by observation. Suppose there is an observation variable formed by summation of state variables as $y = x_1 + x_2$. A change in y will be explained by changes in both x_1 and x_2 even it is introduced by only one of the states. Therefore, there is a SIC between x_1 and x_2 created through shared observation y.

Additionally, if x_1 and x_2 are sensitive to different parameters u_1 and u_2 through a model, respectively, or to say, x_1 and x_2 are physically uncorrelated, the SIC may cause ineffective estimations of the parameters. If x_1 and x_2 are sensitive to the same parameter, the SIC may help to accelerate the convergence process. Fig. 3.1 gives us an example of the former case, and illustrates how satellite observation y build up SIC between states $[x_1, \cdots, x_i, \cdots, x_p]$, which are sensitive to different input parameters $[u_1, \cdots, u_i, \cdots, u_p]$. All parameters are updated no matter which parameter causes a perturbation in the observation. Now it will be shown how SICs occur in our case and work on the DA process. In atmospheric transport models, particles are transported with the wind to somewhere else other than the source position. Thus wind transports information of the emissions from the location of release to the place where the particles reach. Observations of concentration at certain position (in-situ observation) could be used to trace back information of emissions through wind field. This is how the sensitivity of state vector (concentrations) with respect to emissions is formed. However, observations in the real world are usually not of a single state variable but combination of several state variables or other variables, such as satellite data, which measures total column mass load-

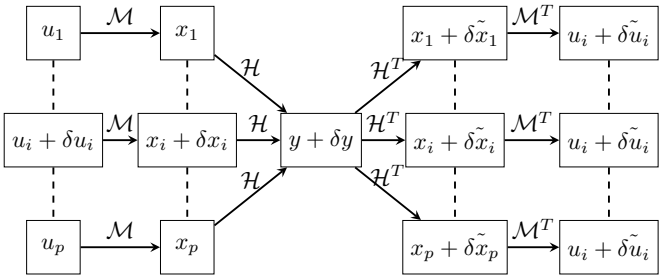

Figure 3.1: The impact of sensor-induced correlations on the update of parameters.

ings of volcanic ash. It is problematic to use observations like this to trace back along the wind field and obtain the emission information. In normal cases, wind fields bear the characteristic that horizontal winds are much stronger than vertical winds (extreme cases such as hurricane are not considered). Hence, states in one layer are sensitive to the input parameter in that layer. Subsequently, states along a column are sensitive to different input parameters locating at the corresponding layers, respectively. Therefore, the satellite observation operator creates strong ISA correlations between physically uncorrelated or slightly-correlated state variables, and between emission source variables. Therefore, a perturbation in one emission layer may result in big values of the element in gradient corresponding to other layers.

3.4. Twin experiments and discussion

3.4.1. Experimental setup

Twin experiments are conducted to test the performance of standard 4D-Var approach on the estimation of volcanic ash emissions using synthetic ash column data and a priori emissions. The synthetic observations are generated by the implementation of the model with the 'true' emission rates.

A simplified LOTOS-EUROS model is utilized to simulate the eruption of the Eyjafjallajökull volcanic activity during April 14-19, 2010. The model computes the forecasts in a tracer mode, which includes only the advection and diffusion processes. Wind fields are obtained from 3-hourly meteorological data from the European Centre for Medium-Range Weather Forecasts (ECMWF), which is interpolated to a hourly resolution.

The emission information of the first few days of explosive eruption is taken from (Webley *et al.*, 2012) and shown by Tab. 2.2 in chapter 2.4. The eruption is described in terms of parameters such as total emission rate and plume height, which are assumed to be constant during an emission episode of several hours. Poisson distribution (see section 2.3) are used to generate the 'truth' emission rates in vertical layers according to emission information in Tab. 2.2. To give the 'background'/a priori emission rates, a total emission rate is used which is an underestimation com-

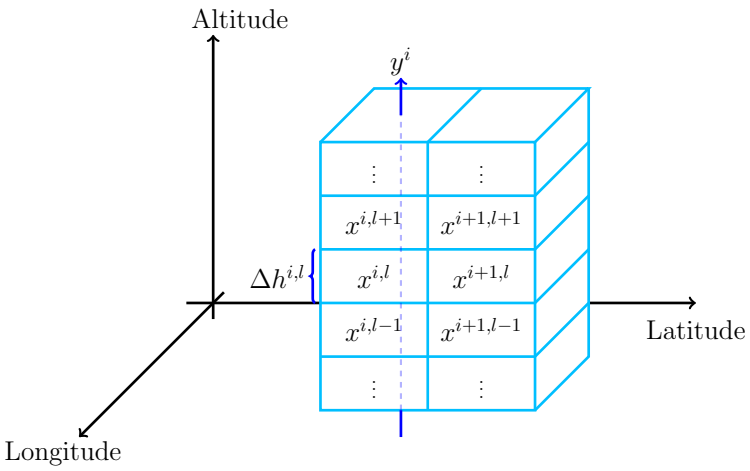

Figure 3.2: An illustration for the computation of the synthetic observations.

pared to the 'truth'. Then the corresponding plume height, which is higher than that of the 'truth', is computed from the empirical relationship (1.1) in chapter 1.3.3, and the vertical profile is also given by Poisson distribution.

Because this chapter focuses on obtaining a theoretical base for future implementations, instead of real data, synthetic observations (μg m^{-2}) is generated by assuming $\omega = 1$ in Eq. (3.4):

$$y^i = \sum_{l=1}^{Nz} x^{i,l} * \Delta h^{i,l}, \tag{3.5}$$

where y^i is the observation variable at i^{th} pixel, $x^{i,l}$ is the ash density at i^{th} pixel and l^{th} vertical layer, $\Delta h^{i,l}$ is the height of the grid cell where $x^{i,l}$ locates. The computation of synthetic observations is illustrated in Fig. 3.2. In reality a satellite instrument will not observe this quantity directly but the optical properties, and the observation operator for the model state should include a radiative transfer model with assumptions on for example the ash density ρ. The observations are obtained hourly such as potentially available from the geostationary SEVIRI instrument Prata and Prata (2012). A spatial resolution of $0.25^\circ \times 0.25^\circ$ is assumed for both modeling and observations, which is equivalent to the spatial resolution of the meteorological data used in this chapter.

To compare the influence of assimilation window length, assimilation windows of 1, 3, or 6 hours are used which are no longer than one emission episode. In practice, assimilation window of constant length should be used within one episode. To deal with the change of episodes, the length should be adaptively shorten within one episode. Since in our case new released particles will not spread further than 50 grid cells horizontally within 6 hours according to local wind velocity, a small domain

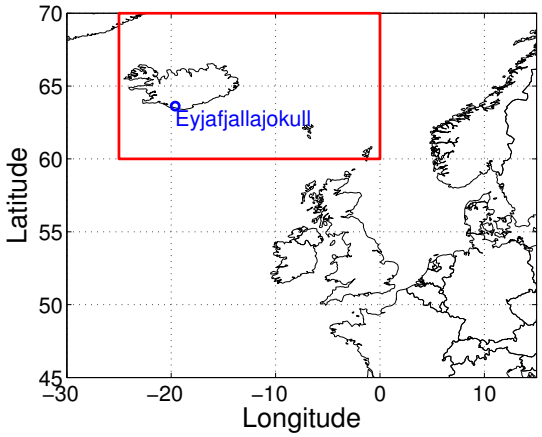

Figure 3.3: European domain for forecast and Iceland domain in the rectangular for assimilation.

(Iceland area in the red rectangular, Fig. 3.3) is employed for the assimilation in order to keep a low computational expense. In practice, an extended domain (European area, Fig. 3.3) should be used for forecast in one day or longer after assimilation.

In the experiments, both deterministic model and stochastic model are used. For deterministic (noise-free) model experiments, observations are obtained by direct realization of the model with the 'truth' emission rates. Since the emission parameters $\mathbf{u}$ and the observation variables $\mathbf{y}_k$ are assumed to be independent, the background covariance matrices $\mathbf{B}$ and observation covariance matrices $\mathbf{R}_k$ are diagonal (in Eq. (3.1)-(3.2)), in forms of $\mathbf{B} = \sigma_b^2\mathbf{I}$ and $\mathbf{R}_k = \sigma_o^2\mathbf{I}$, respectively. For experiments using models with uncertainties, 50% noise is added to observation data according to realistic satellite instrument retrieval uncertainties in section 3.3. For the construction of $\mathbf{B}$ in the cost function (3.3) of the stochastic model, the uncertainties in the background parameters are always assumed to be 50%.

3.4.2. Estimation of volcanic ash emissions

First, a perfect model and complete observation which measures the state variables in all the grid cells are used to verify whether the model is physically well-conditioned. The results with 1h assimilation window are shown in Fig. 3.4, where the 'analysis' perfectly matches the 'truth', and the results with 3h and 6h assimilation windows are similar. This means emission rates can be well estimated using standard 4D-Var according to model dynamic. Therefore, once the estimation result with another observation operator is undesirable, it is caused by the observation but not the model.

Next, experiments with satellite ash column observations are conducted by both the noise free model and stochastic model, and 50% noise are added in the synthetic observations for the stochastic case. The noise-free model is used here to

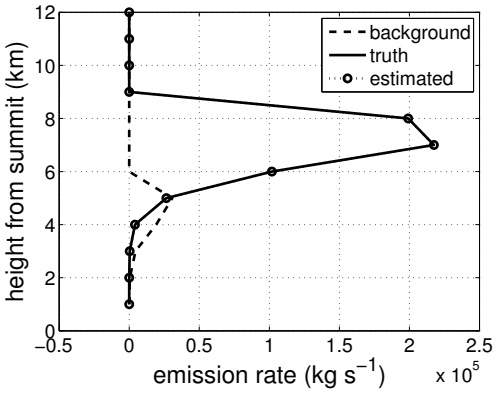

Figure 3.4: Estimation result of emission rates using standard 4D-var with complete observations and 1h assimilation window.

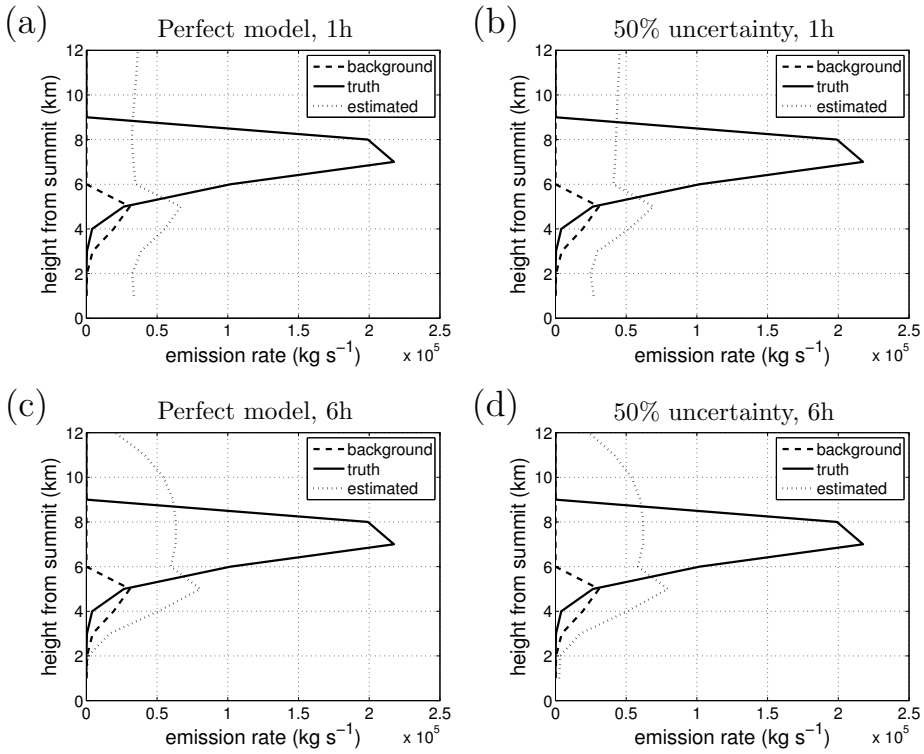

Figure 3.5: Estimation result of emission rates using standard 4D-var with satellite observations and assimilation window of (a)-(b) 1h and (c)-(d) 6h, conducted by the noise-free model (left column) and the stochastic model (right column), respectively.

exclude the influences of uncertainty in observations or other disturbance for the performance of the assimilation approach. Note that in the noise-free model with a zero observational error covariance matrix, the inverse of the matrix will be infinity and the 'background' term vanishes compared to the 'observation' term. The stochastic model is able to create a more realistic simulation situation, besides, it can be used to include the influence of 'background' term.

Results in Fig. 3.5 shows that standard 4D-Var is incapable of reconstructing the vertical profile of the emissions. The injection height is unable to be accurately determined. To be more specific, the emissions are corrected as a whole, i.e., the total emission rate is improved, and the emission rates in each layer are increased by almost the same amount. This ineffective estimation problem is not caused by observation uncertainty but the observation itself (comparing Figs. 3.5(a) with 3.4). The problem will not be solved or improved by including the background term (comparing the figures in right column against those in the left column of Fig. 3.5). Enlarging the assimilation window and integrating a larger the amount of data do not have obvious improvement of the situation (comparing Figs. 3.5(c)-(d) against Figs. 3.5(a)-(b)).

3.4.3. Impact on volcanic ash forecast

Forecasts are produced using emissions of the truth, the background and the estimated till the end of assimilation (at 19:00 UTC, April 14, 2010), which are regarded as initial conditions for future prediction, shown by Fig. 3.6. It can be seen that the ash columns of the forecast with assimilation have been largely improved from the background and are closer to the observations of the truth (Figs. 3.6(a)-(c)).

However, shapes and concentrations of ash cloud at individual layers do not fit the 'truth'. To illustrate this aspect, ash concentration fields are used which are taken out of the 7^{th} layer (Figs. 3.6(d)-(f)) and 5^{th} layer (Figs. 3.6(g)-(i)) above the summit, which are the injection layers with the maximum emission rates of the 'true' and 'background' emissions, respectively. We can see that the ash concentrations are increased in both layers with assimilation, but the shapes and positions do not match the 'truth'. This is implied by the estimates of emissions, the total amounts of which are increased but the vertical profiles do not match the true emissions. This would misguide us to regard that the initial condition is good enough for an accurate forecast in a nearby future (less than 24 hours) by only comparing the ash columns.

Next, comparison are made for the future forecasts in Fig. 3.7, which are the model simulations at 10:00 UTC, April 15, 2010, using the above initial conditions. We compare the main bodies of the ash clouds around Western Norway and Western Sweden, where the ash particles can be by the assimilation. It can be observed that either the ash concentration fields (Figs. 3.7(d)-(f) and (g)-(i)) or the ash mass loading fields (Fig. 3.7 (a)-(c)) do not fit the 'truth'. This would mean that, in an application with real data, even if we obtain an analysis which matches satellite image, there is a high probability that we may still give a bad and misguiding forecast.

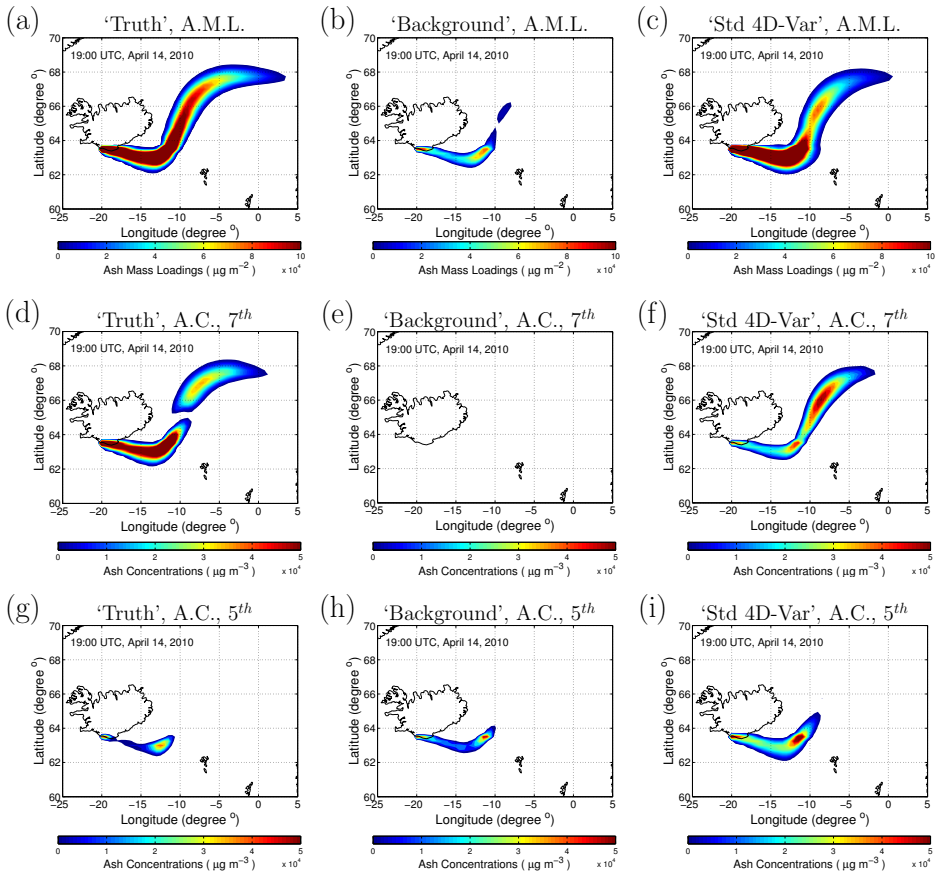

Figure 3.6: Forecasts of volcanic ash clouds at 19:00 UTC, April 14, 2010 with (a), (d), (g): the true emissions; (b), (e), (h): the background emissions; (c), (f) and (i): the estimate of emissions using standard 4D-Var approach. The top row illustrates the ash mass loading fields, the middle row illustrates the ash concentration fields at the 7^{th} layer above the summit, and the bottom row illustrates the ash concentration fields at the 5^{th} layer above the summit.

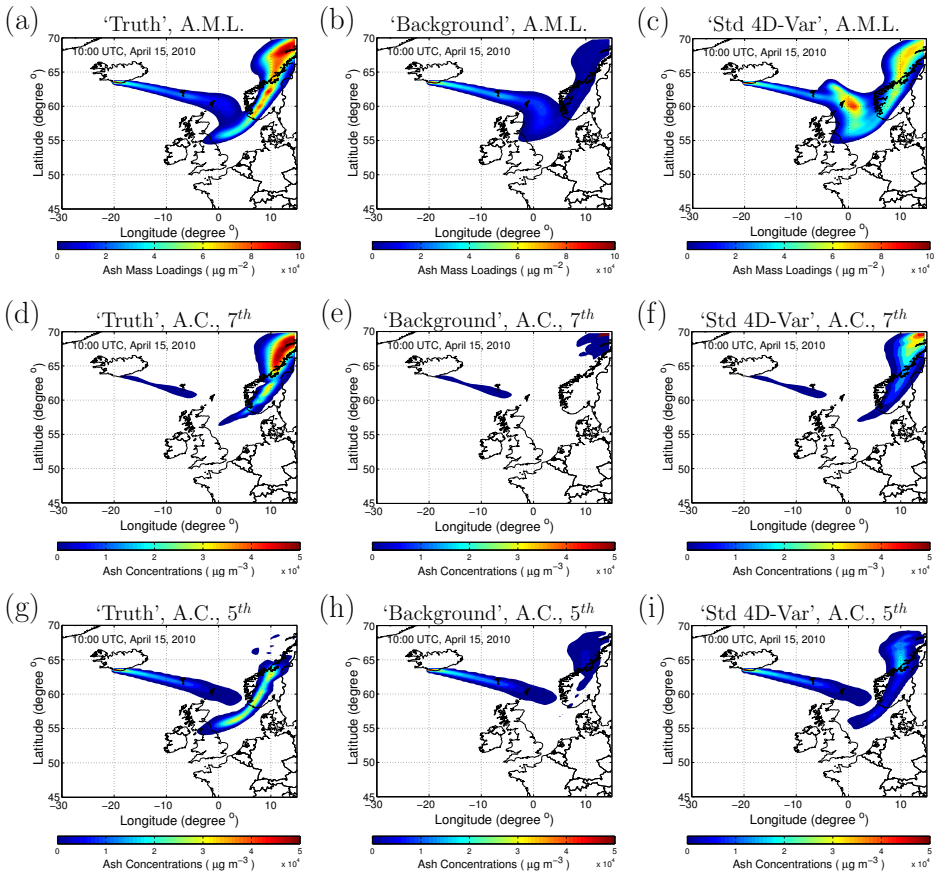

Figure 3.7: Forecasts of volcanic ash clouds at 10:00 UTC, April 15, 2010 with (a), (d), (g): the true emissions; (b), (e), (h): the background emissions; (c), (f) and (i): the estimate of emissions using standard 4D-Var approach. The top row illustrates the ash mass loading fields, the middle row illustrates the ash concentration fields at the 7^{th} layer above the summit, and the bottom row illustrates the ash concentration fields at the 5^{th} layer above the summit.

3.4.4. Ineffectiveness of the standard 4D-Var approach

To illustrate how ineffective ISA correlation and invalid gradient lead to the problem, a single-input-perturbation experiment is conducted. In the experiment, perturbation is given in a single input parameter and gradients are computed and normalized with both complete observations and column observations. The former reflects model behavior and the comparison with the perturbation vector illustrates whether the model is physically well conditioned to identify the perturbed parameter, which will be called normalized 'model gradient'. The latter compared with normalized 'model gradient' illustrates whether the observation creates ineffective ISA correlations or leads to invalid gradient, which can be called normalized 'observation gradient' accordingly. The formulations are given based on model representation in Eqs. 3.1-3.1.

The true observations are computed by:

$$\mathbf{x}_k^t = M_k(\mathbf{x}_{k-1}^t, \mathbf{u}), \tag{3.6}$$
$$\mathbf{y}_k^t = H_k(\mathbf{x}_k^t). \tag{3.7}$$

where $\mathbf{y}_k^t$ are the synthetic column observations.

The background model simulations with single-input-perturbation on the i^{th} input variable are:

$$\mathbf{x}_k^t = M_k(\mathbf{x}_{k-1}^t, \mathbf{u} + \Delta\mathbf{u}^i),, \tag{3.8}$$

where $\Delta\mathbf{u}^i = [u_1, \cdots, \Delta u_i, \cdots, u_p]^T$.

J^{col} and J^{com} are the cost functions with column observations and complete observations, respectively, given as following:

$$J^{col} = (\mathbf{y}_k^t - H_k(\mathbf{x}_k))^T(\mathbf{y}_k^t - H_k(\mathbf{x}_k)), \tag{3.9}$$
$$J^{com} = (\mathbf{x}_k^t - \mathbf{x}_k)^T(\mathbf{x}_k^t - \mathbf{x}_k), \tag{3.10}$$

The model gradient and observation gradient will be $\nabla J_{\mathbf{u}}^{com}$ and $\nabla J_{\mathbf{u}}^{col}$, respectively.

In this experiment, the 7^{th} parameter is perturbed which bears the biggest difference between the 'background' and the 'truth' input, and the both normalized gradients are shown in Fig 3.8. It is observed that 'model gradient' can well represent the perturbation of the input but 'observation gradient' evens out the perturbation. Moreover, the value of the 'observation gradient' with respect to the 7^{th} parameter is smaller than to some other parameters. This is consistent with the estimation results, which means the estimation result will never reach the 'truth' regardless of the number of iterations.

3.5. Summary and conclusions

The adjoint model is needed for the computation of the gradient of objective function in the implementation of the 4D-Var approach. The LOTOS-EUROS model has been simplified and modified such that the corresponding adjoint model is easy to build. 4D-Var approach has been integrated to the simplified model, and twin experiment was carried out for the volcanic ash problem based on this configuration.

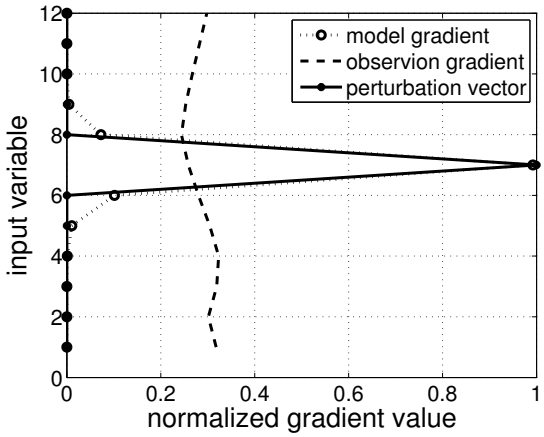

Figure 3.8: Normalized gradient generated by perturbation in a single input parameter at the 7^{th} layer above the summit with 1h assimilation window.

The experimental outcomes illustrated that was unable to reproduce the mass vertical structure of the ash emissions. The plume height, which has been shown to be an important parameter in the construction of emission source, was not accurately determined. Actually, the total emission rate was corrected and the correction effect was distributed almost evenly in the vertical. The forecasts of ash cloud produced by this estimates of emissions were misleading. The ash-column field has been largely improved, from which one can believe that this forecast was good and reliable. However, the interior concentration fields differed a lot from that of the truth.

The ill-conditioning problem is attributed to the fact that one data value was computed by the integration of several state variables. This integrated data will create numerical and ISA correlation between the states that share the data and may not be physically correlated. Some input (emission) variables are strongly related to these states. Therefore, ISA correlations are consequently created between these inputs. This resulted in the inappropriate estimate of the inputs, where the change of one variable is related to the perturbation of another variable. Experiment was designed and conducted based on this discussion to gain insight of how the ISA correlation was created and influenced the estimates. The results confirmed the theoretical analysis and showed that each variable had strong correlations to all other variables. This fact will inspire the development of an alternative assimilation approach in the next chapter.

4

Trajectory-based 4D-Var for volcanic ash problem: twin experiment

The ill-conditioned problem of using 4D-Var approach with a standard type of cost function to estimation volcanic ash emissions by assimilating ash column observations has been addressed from the perspective of SICs as mentioned in the previous chapter. In order to make better use of the influence of SICs created by observations integrating multiple state variables, an alternative approach termed 'trajectory-based 4D-Var (Trj4DVar)' is proposed. This approach is adjoint-free, which is more accurate to estimate the vertical profile of volcanic ash from volcanic eruptions. It seeks the optimal vertical distribution of emission rates of a reformulated cost function which computes the total difference between simulated and observed ash columns. Twin experiments are conducted to test the performance of the new method. Experimental results are compared against those of using standard 4D-Var to assess the improvement on methodology on dealing with integrated type of observations.

Parts of this chapter have been published in:
Lu, S.*, Lin, H.X., Heemink, A.W., Fu, G., and Segers, A.J. (2016). Estimation of Volcanic Ash Emissions Using Trajectory-Based 4D-Var Data Assimilation. ***M*onthly Weather Review** 144, 575-589, 2016.

4.1. Introduction

The forecast of the locations and concentrations of the volcanic ash cloud is very sensitive to emissions. However, it is a great challenge to accurately determine source parameters such as vertical distribution of volcanic emission plume. Volcanoes exhibit a wide range of eruption types, thus it is difficult to make assumptions of emission parameters estimation for predictive purpose. Up to now, indirect methods are used to estimate volcanic ash emissions (Mastin *et al.*, 2009b). For instance, empirical relationship between plume height above vent and total volume has been used to determine total emission rates from plume altitude observations. This plume height could be obtained from aircraft measurements (Mankin *et al.*, 1992) or ground-based radar or Lidar observations (Wang *et al.*, 2008), which are often not available. Then, in practice, explicit assumptions on the vertical distribution have to be made such as an uniform-distributed (Dacre *et al.*, 2011), umbrella-shaped (Stuefer *et al.*, 2013; Webley *et al.*, 2012), Poisson-distributed, or exponentially-distributed plume (Searcy *et al.*, 1998). Even if the vertical distribution is more or less correct, the relationship between plume height and total emission is loose, thus the vertical assignment of the total emission rates to each layer is poorly quantified.

Data assimilation (DA) techniques, which have been used in traditional weather forecasting for many years, can be applied for forecasting volcanic ash (Fu *et al.*, 2015, 2016). The variational approach has already been used to estimate volcanic eruptive parameters and to improve the forecast accuracy using satellite Ash Mass Loading (AML) data (Strunk *et al.*, 2010). Flemming and Inness (2013) used satellite observations of sulfur dioxide to estimate the total emission rate and the plume height using a 'trajectory-matching' 4D-Var method. However, the vertical distribution of the emission rate remains uncertain. Eckhardt *et al.* (2008) first reconstructed the vertical profiles of sulfur emissions from AML data based on the inverse modeling approach proposed by Seibert (2000). Stohl *et al.* (2011) improved the inverse modeling method to estimate the vertical profile of the volcanic ash emissions and the mass eruption rate of fine ash as a function of both height and time.

Satellite ash-column observations lack vertical resolution which integrate the states in a column. This will result in strong SICs between the input variables distributed vertically which are assumed to be independent on each other in our case as mentioned in the previous chapter. The SICs can lead to the failure of using the standard 4D-Var (Std4DVar) to estimate the volcanic ash emissions due to improper specification of error statistics. To remedy this, a trajectory-based 4D-Var (Trj4DVar) assimilation method is proposed as an alternative.

This chapter has the following topics. Section 4.2 gives the derivation of Trj4DVar, the steps to conduct the algorithm and an acceleration scheme. In section 4.3, the performance of Trj4DVar in the application of volcanic ash problem is tested in the twin experiments, and comparison is made between Trj4DVar and Std4DVar. Section 4.4 gives a brief summary of this chapter.

4.2. Trajectory-based 4D-Var approach

4.2.1. Derivation of trajectory-based 4D-Var

We can reduce the influnece of SICs artificially by perturbing parameters one by one, such that the states sensitive to the perturbed parameter are automatically activated and separated from other states. Therefore, we propose a modified 4D-Var method, which reformulates the least square problem by using a better error statictics for the SICs. In this method, we seek a linear combination of states (or trajectories) generated by system simulations with perturbed input parameters, which best matches the observation data.

The trajectories consists of a reference simulation with background input parameters $M_k(\mathbf{x}_{k-1}, \mathbf{u}^b)$ and a set of simulations with perturbed parameters $M_k(\mathbf{x}_{k-1}, \mathbf{u}^b + \Delta\mathbf{u}^i)$ for $i = 1, \cdots, p$, where $\Delta\mathbf{u}^i$ is a perturbation of the emission rate in the i^{th} layer above summit, which is the i^{th} effective emission layer and denoted as i^{th} EEL in this chapter. Then we define the background measurements: $\mathbf{y}_k^0 = H_k(M_k(\mathbf{x}_{k-1}, \mathbf{u}^b))$ and the snapshot measurements: $\Delta\mathbf{y}_k^i = H_k(M_k(\mathbf{x}_{k-1}, \mathbf{u}^b + \Delta\mathbf{u}^i)) - \mathbf{y}_k^0$. Suppose the parameter space can be spanned by the perturbed parameter sets, which means that the 'truth' can be computed as a linear combination of perturbed parameters weighted by unknown parameters β^i: $\mathbf{u} = \mathbf{u}^b + \sum_{i=1}^{p} \beta^i \Delta\mathbf{u}^i$. Then the observations in Eq. (3.2) can be approximated by:

$$\begin{aligned}
\mathbf{y}_k &\approx H_k(M_k(\mathbf{x}_{k-1}, \mathbf{u}^b)) + \sum_{i=1}^{p} \beta^i \mathbf{H}_k \mathbf{M}_k(\mathbf{x}_{k-1}, \mathbf{u}^b) \Delta\mathbf{u}^i + \mathbf{v}_k \\
&\approx \mathbf{y}_k^0 + \sum_{i=1}^{p} \beta^i (H_k(M_k(\mathbf{x}_{k-1}, \mathbf{u}^b + \Delta\mathbf{u}^i)) - \mathbf{y}_k^0) + \mathbf{v}_k \\
&= \mathbf{y}_k^0 + \sum_{i=1}^{p} \beta^i \Delta\mathbf{y}_k^i + \mathbf{v}_k,
\end{aligned} \tag{4.1}$$

where $\mathbf{H}_k$ and $\mathbf{M}_k$ denote the tangent linear model of H_k and M_k, respectively. Therefore, the coefficients $\boldsymbol{\beta} = [\beta^1, \cdots, \beta^p]$ can be computed by minimizing the reformulated cost function given by:

$$\begin{aligned}
J(\boldsymbol{\beta}) &= \frac{1}{2} \sum_{k=1}^{Nt} \left(\sum_{i=1}^{p} \beta^i \Delta\mathbf{y}_k^i + \mathbf{y}_k^0 - \mathbf{y}_k \right)^T [\mathbf{R}_k]^{-1} \left(\sum_{i=1}^{p} \beta^i \Delta\mathbf{y}_k^i + \mathbf{y}_k^0 - \mathbf{y}_k \right) \\
&+ \frac{1}{2} \sum_{k=1}^{Nt} \left(\mathbf{u} - \mathbf{u}^b \right)^T [\mathbf{B}_k]^{-1} \left(\mathbf{u} - \mathbf{u}^b \right) + \mu ||\nabla\mathbf{u}||^2 \\
&= J^o + J^b + J^r,
\end{aligned} \tag{4.2}$$

where J^o and J^b are defined similar to those in cost function Eq. (3.3), and J^r is a regularization term in case that large uncertainties in model or observations lead to unstable solution or negative solution.

When the number of parameters is small (less than 100) we can transform the optimization problem into an algebraic problem and solve it directly. As it can be observed that cost function (4.2) is convex, according to the first order optimality condition, to find the minimum is to find the solution to the linear problem:

$$\frac{dJ}{d\boldsymbol{\beta}} = \frac{dJ^o}{d\boldsymbol{\beta}} + \frac{dJ^b}{d\boldsymbol{\beta}} + \frac{dJ^r}{d\boldsymbol{\beta}} = 0. \tag{4.3}$$

Simple derivation and moving all the terms independent of $\boldsymbol{\beta}$ to the right hand side yields:

$$(\mathbf{A}^o + \mathbf{A}^b + \mathbf{A}^r)\boldsymbol{\beta} = \mathbf{b}^o + \mathbf{b}^b + \mathbf{b}^r, \tag{4.4}$$

where

$$\mathbf{A}^o = \begin{bmatrix} \Delta\mathbf{y}_1^1 & \cdots & \Delta\mathbf{y}_1^p \\ \vdots & \ddots & \vdots \\ \Delta\mathbf{y}_{Nt}^1 & \cdots & \Delta\mathbf{y}_{Nt}^p \end{bmatrix}^T \begin{bmatrix} [\mathbf{R}_1]^{-1} & & 0 \\ & \ddots & \\ 0 & & [\mathbf{R}_{Nt}]^{-1} \end{bmatrix} \begin{bmatrix} \Delta\mathbf{y}_1^1 & \cdots & \Delta\mathbf{y}_1^p \\ \vdots & \ddots & \vdots \\ \Delta\mathbf{y}_{Nt}^1 & \cdots & \Delta\mathbf{y}_{Nt}^p \end{bmatrix}, \tag{4.5}$$

$$\mathbf{b}^o = \begin{bmatrix} \Delta\mathbf{y}_1^1 & \cdots & \Delta\mathbf{y}_1^p \\ \vdots & \ddots & \vdots \\ \Delta\mathbf{y}_{Nt}^1 & \cdots & \Delta\mathbf{y}_{Nt}^p \end{bmatrix}^T \begin{bmatrix} [\mathbf{R}_1]^{-1} & & 0 \\ & \ddots & \\ 0 & & [\mathbf{R}_{Nt}]^{-1} \end{bmatrix} \begin{bmatrix} \mathbf{y}_1 - \mathbf{y}_1^0 \\ \vdots \\ \mathbf{y}_{Nt} - \mathbf{y}_{Nt}^0 \end{bmatrix}, \tag{4.6}$$

$$\mathbf{A}^b = \begin{bmatrix} \Delta\mathbf{u}^1 & \cdots & \Delta\mathbf{u}^p \end{bmatrix}^T \left(\sum_{k=1}^{Nt} [\mathbf{B}_k]^{-1} \right) \begin{bmatrix} \Delta\mathbf{u}^1 & \cdots & \Delta\mathbf{u}^p \end{bmatrix}, \tag{4.7}$$

$\mathbf{b}^b = 0$, $\mathbf{A}^r = \mu\mathbf{L}$, $\mathbf{b}^r = 0$, and regularization operator $\mathbf{L}$ is defined in section 4.2.2.

The Trj4DVar algorithm is thus described as the following sequence of operations:

1. Specify the background emission rates $\mathbf{u}^b$ and run the model to obtain model state $\mathbf{x}_k = M_k(\mathbf{x}_{k-1}, \mathbf{u}^b)$ and background measurement $\mathbf{y}_k^0 = H_k(\mathbf{x}_k)$ $(k = 1, \cdots, Nt)$.

2. Perturb the emission rates $\mathbf{u}^i = \mathbf{u}^b + \Delta\mathbf{u}^i$ and perform the forward model runs $\mathbf{x}_k^i = M_k(\mathbf{x}_{k-1}^i, \mathbf{u}^i)$, then compute the snapshot measurements $\Delta\mathbf{y}_k^i = H_k(\mathbf{x}_k^i) - \mathbf{y}_k^0$ $(k = 1, \cdots, Nt,\ i = 1, \cdots, p)$.

3. Solve the linear system of equations (4.4) to obtain coefficients $\boldsymbol{\beta} = [\beta^1, \cdots, \beta^p]^T$.

4. Update emission rates $\mathbf{u} = \mathbf{u}^b + \sum_{i=1}^p \beta^i \Delta\mathbf{u}^i$.

Note that Trj4DVar is adjoint free, since it needs only forward model runs to generate the trajectories and the effort to solve the transformed algebraic problem without adjoint model runs to compute the gradients. This saves the effort in the formulation and implementation of the tangent linear model and the adjoint model for the transport model, which is usually required for a 4D-Var application.

Since the meteorological conditions vary at each layer, the position and shape of the ash plume bear information on its emission altitude, and vice versa. Therefore, the snapshots $\Delta\mathbf{y}_k^i$ have different values as wind fields change with altitude, which benefits in emission profile estimation with this trajectory-based 4D-Var (Trj4DVar) method. Trj4DVar would not work with velocity fields that are vertically unchanged. Fortunately, this is not the case in the real world. However, there are still cases where meteorological pattern of one layer bear a great resemblance to that of other layers, which will result in unstable solution. This problem can be solved by regularization as mentioned above, and details will be given in section 4.2.2.

Notice that although the formulation is similar, our method is different from ensemble-based 4D-Var(En4DVar) (Tian *et al.*, 2008; Liu *et al.*, 2009; Tian *et al.*, 2011) in three folds. First, this method aims at solving the ill-conditioning problem in our case, whereas En4DVar targets at obtaining a flow-dependent error covariance matrix. Second, the generation of trajectories in this method is specially designed according to a priori knowledge of the model property and the characteristics of the observation, but En4DVar adopts Monte Carlo method which technically can be applied to any case. Third, this method is not scalable to the cases with a huge amount of parameters and it is specially designed to efficiently estimate vertical emission profile with a relative small number of parameters, while En4DVar naturally reduces the rank of the problem and can be scalable to high-dimensional cases. However, in our case, the utilization of En4DVar with a set of randomly generated ensembles would lead to inaccurate estimation as standard 4D-Var does (see Figs. 3.5 and 4.5).

4.2.2. Regularization

There are three types of ill-posedness of an inverse problem (the optimization problem in our case): the solution does not exist, is not uniqueness or is unstable (Doicu *et al.*, 2010). In our case we have the third type, the stability of the solution. Note that due to the severe ill-conditioning of the Hessian ($\mathrm{Hess} = [\sum_{k=1}^{Nt}(\Delta\mathbf{y}_k^i)^T(\Delta\mathbf{y}_k^j)]_{ij}$) in the term J^o of cost function (4.2) and the noise in the observations $\mathbf{y}_k$, the solution of minimizing J^o is not a meaningful approximation of the 'truth'. In order to be able to obtain an accurate approximation of the 'truth', a regularization term is added in the cost function, whose solution is less sensitive to perturbations in $\mathbf{y}_k$ (Reichel and Ye, 2008).

Actually, the 'background' term J^b plays a role as regularization term (Cacuci *et al.*, 2013), but the ill-posedness of the problem is still unresolved although somewhat improved since we can not arbitrarily enlarge the proportion it takes in cost function (4.2). Firstly in our case the 'background' emissions have a large uncertainty, a larger proportion of J^b leads to a solution closer to the very inaccurate 'background' emissions; and secondly the weighting factors of J^o and J^b (i.e. $[\mathbf{R}_k]^{-1}$ and $[\mathbf{B}_k]^{-1}$) are generated according to their statistic properties through Bayesian theory in 4D-Var approaches, hence increasing the weighting for J^b will make it statistically unrealistic. Therefore, an extra term J^r for regularization is introduced in cost function (4.2).

In the Trj4DVar approach, the popular Tikhonov regularization is used, where a

regularization term is in the following form

$$J^r(\boldsymbol{\beta}) = \mu||L\boldsymbol{\beta}||^2, \tag{4.8}$$

where the matrix $L \in R^{k\times p}$, is referred to as the regularization operator and the scalar $\mu \leq 0$ as the regularization parameter.

Common choices of regularization operators are the identity matrix and a scaled finite difference approximation of a derivative $||\nabla\boldsymbol{\beta}||^2$ (equals $||\nabla\mathbf{u}||^2$ in our case). They both have a smoothing effect on the solution and make the solution more stable. However, when μ is large, using identity matrix results in a solution close to zero, while using the derivative can preserve the total emission rate. Therefore, in this chapter, a scaled finite difference approximation of a derivative in the following forms is used:

$$L_1 := \frac{1}{2}\begin{bmatrix} 1 & -1 & & & 0 \\ & 1 & -1 & & \\ & & \ddots & \ddots & \\ 0 & & & 1 & -1 \end{bmatrix} \in R^{(p-1)\times p} \tag{4.9}$$

or

$$L_2 := \frac{1}{4}\begin{bmatrix} -1 & 2 & -1 & & & 0 \\ & -1 & 2 & -1 & & \\ & & \ddots & \ddots & \ddots & \\ 0 & & & -1 & 2 & -1 \end{bmatrix} \in R^{(p-2)\times p}. \tag{4.10}$$

4.2.3. Acceleration schemes

Most of the computational cost of the Trj4DVar method lies in the generation of the trajectories. Therefore, the total cost is linearly proportional to the number of forward model simulations denoted by n_{sim}^{ref}. The number of ensembles n_{sim}^{ref} is equal to the number of input parameters p according to section 4.2.1. For standard 4D-Var method the computation of gradients takes most of the time, which can also be quantified in terms of forward model simulations n_{sim}^{trad}. Since one gradient computation requires one forward run and one adjoint run, this can be counted approximately as two forward simulations. Thus n_{sim}^{trad} equals to the twice the number of iterations n_{itr}. Therefore, when p and $2n_{itr}$ are almost the same, the computational costs of the two methods are comparable. In our experiment, p is smaller than $2n_{itr}$ and thus the reformulated method is more efficient in this case.

However, n_{sim}^{ref} increases with p, thus refining grid cells vertically could make the reformulated 4D-Var less efficient than the standard 4D-Var. Moreover, to deal with the nonlinearity of a more realistic model, the reformulated 4D-Var scheme should be repeated several times with new ensembles generated from an updated background state $\mathbf{x}_k^{updated}$ and parameters $\mathbf{u}^{b,updated}$ in each iteration. This problem can be reduced by a simple acceleration scheme through generating multiple ensembles in one forward simulation. This can be done in the following way:

1. In one simulation, we perturb multiple input parameters which are physically unrelated or slightly related to each other. For instance we perturb the input variables located in every m layers (i.e., with a distance of m layers) as follows $\mathbf{u} = \mathbf{u}^b + \sum_{i=1}^{(p-1)/m} \Delta\mathbf{u}^{m*i+1}$, and compute $\Delta\mathbf{x}_k = M_k(\mathbf{x}_{k-1}, \mathbf{u}) - M_k(\mathbf{x}_{k-1}, \mathbf{u}^b)$.

2. After the forward simulation, we generate the ensembles corresponding to each perturbed parameter by computing the column integral of the layers where the states are sensitive to the specific parameter according to Eq. (3.4) as follows

$$\Delta \mathbf{y}_k^l = \sum_{j=\max\{1,l-(m+1)/2\}}^{\min\{p,l+(m+1)/2\}} \omega^j * \Delta \mathbf{x}_k^j . * \Delta \mathbf{h}^j, \qquad l = m * i + 1, \quad i = 1, \cdots, (p-1)/m. \tag{4.11}$$

3. Repeat 1 and 2 to compute trajectories $\Delta \mathbf{y}_k^{m*i+j}, i = 1, \cdots, (p-j)/m$, with perturbed parameter $\mathbf{u} = \mathbf{u}^b + \sum_{i=1}^{(p-j)/m} \Delta \mathbf{u}^{m*i+j}$, $j = 2, \cdots, m$.

In this way, we can efficiently obtain the entire approximated trajectories with m model simulations, which is independent of p. There is a trade off between a small value of m and high accuracy of the trajectories.

4.3. Twin experiments and discussion

4.3.1. Experimental setup

Twin experiments are conducted to test the performance of Trj4DVar approach, on a PC with an Intel Xeon E3-1240 V2 processor with 8 cores, a total memory of 32 GB (approximately 5% was taken during experiments) and a clock speed of 3.4GHz. In order to compare the it with Std4DVar, the same experimental configurations as in chapter 3 are employed.

The influence of assimilation window on the approach are tested with length 1-hour, 3-hour, and 6-hour. Both deterministic model and stochastic model are used. The former is used to compare the difference between Std4DVar and Trj4DVar. The latter is used to explore the influences of uncertainties or other aspects to the performance of Trj4DVar. 50% Gaussian noise is added to the synthetic observations according to realistic satellite instrument retrieval uncertainties in section 3.3. Besides, in order to investigate the influence of noise for solutions 10% noise is used in comparison experiments.

4.3.2. Estimation of volcanic ash emissions

The Trj4DVar method is first applied to the noise-free model with the same background emissions as in the previous experiments, and the comparison with the standard 4D-Var method shows that this method can help solve the ill-conditioned problem caused by the radiation observation (Fig. 4.1 compared with Fig. 3.5(d)). However, when it is applied to a stochastic model, unstable solution with big oscillations occurs especially with a small assimilation window (Fig. 4.2(a)), which is caused by the similarity of meteorological fields in each layer. Therefore, the regularization term is used according to a priori knowledge of the model that the input should be smoothed.

To test the influence of noise, assimilation window length and regularization term on the performance of Trj4DVar, we apply Trj4D-Var with 50% model uncertainties, 10% and 50% observation uncertainties and assimilation windows of 1h, 3h and 6h, respectively, and the results are shown in Fig 4.2 where 'est_reg' is the estimate

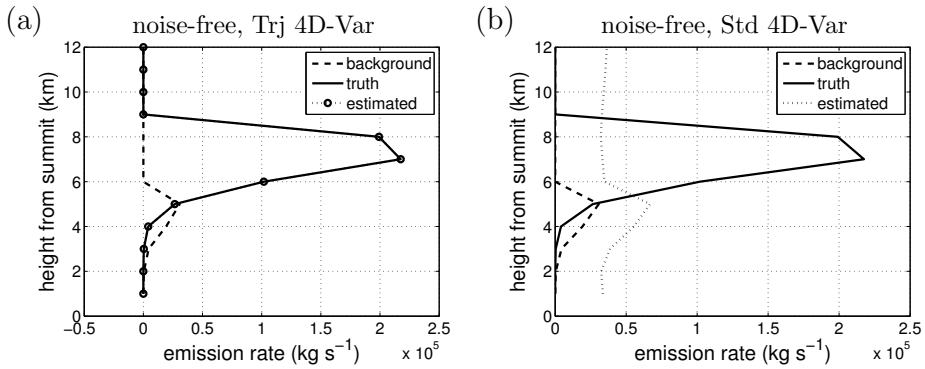

Figure 4.1: Estimation result with 1h assimilation window and a noise-free model using (a): Trj4Dvar method; and (b): Std4DVar .

with regularization.

It can be noticed that the basic vertical profile of inputs is preserved in Fig. 4.2, especially the effective injection layer is well estimated, but oscillations in the solution occur when noise is added to observations. We observe large oscillation in 1h cases especially with 50% observation noise in Fig. 4.2(d). Situation is improved with smaller observation uncertainty or larger assimilation window. This can be explained from the perspective of statistics that larger amount of data can reduce the disturbance of noise and provide more stable solution.

Moreover, by comparing the results with 10% noise and 50% noise, we can observe obviously that in Figs. 4.2(e) and 4.2(f) a spike appear around the 5^{th} layer where the maximal input of 'background' lies, which is because with larger observation uncertainty the 'background' impact more in the solution. Enlarging assimilation window helps improving the situation, which can be observed by comparing the 3 figures with 50% uncertainty. However, enlarging the assimilation window will increase computational time polynomially with both increased DA time and enlarged DA domain, thus a trade off should be made between stable solution and computational efficiency.

Regularization can smooth the solution and reduce oscillation (Fig. 4.2(a)), which improves the accuracy of parameter estimation. However, sometimes it works in a negative way that it smooths the solution too much and thus decreases the accuracy (Fig. 4.2(f)). Therefore, compromise should be made between the oscillation problem and the smoothing problem. The impact of regularization decreases with the length of assimilation window, which can be observed by comparing the 1h, 3h and 6h cases. It would not be a problem, because as the estimation becomes more accurate with bigger assimilation window, regularization becomes less important to further improve the accuracy.

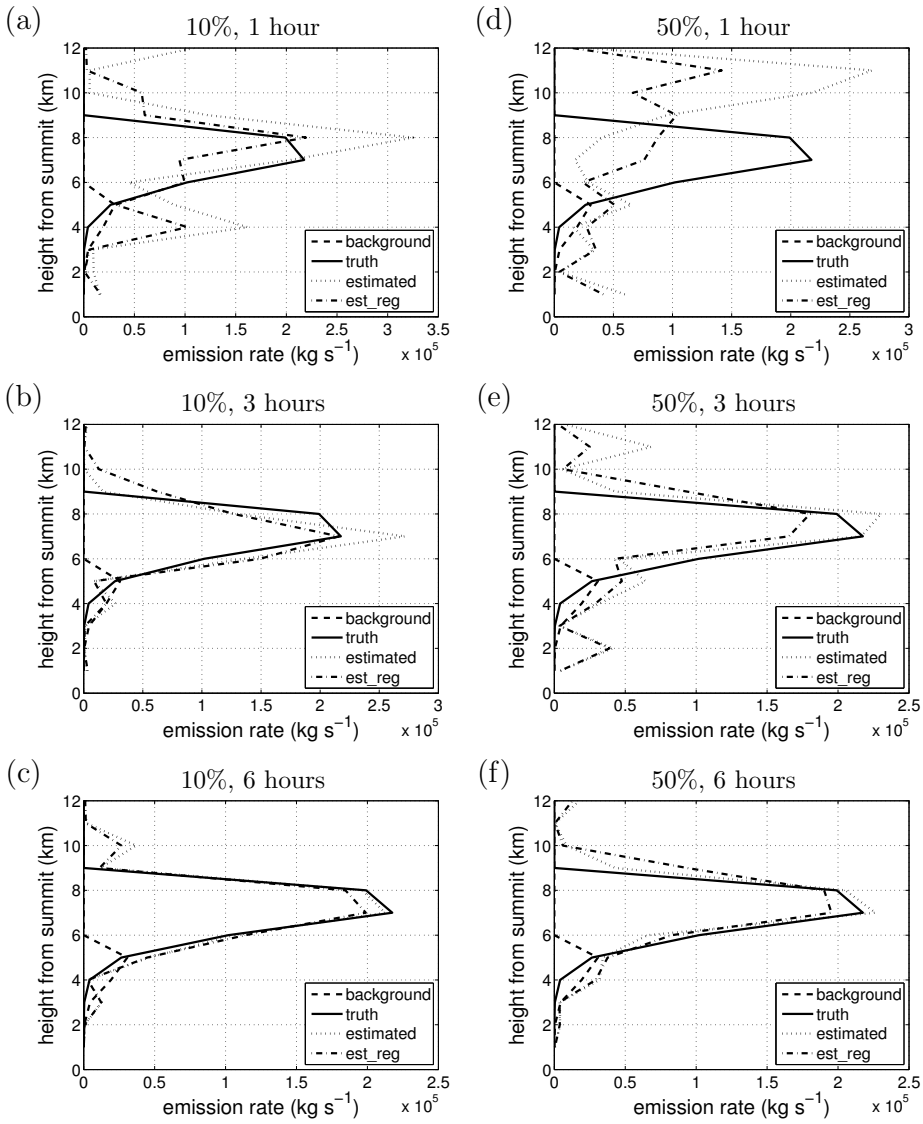

Figure 4.2: Trj4DVar results of twin experiments with (a)-(c) 10% and (d)-(f) 50% observation noise and assimilation window of (a),(d) 1h; (b),(e)3h and (c),(f) 6h.

4.3.3. Impact on volcanic ash forecast

With a more accurate estimation of vertical profile of emission rates, a better forecast of state fields will be obtained. Although the forecasts of ash mass loadings using both Std4DVar and Trj4DVar methods are largely improved (Fig. 4.4), Trj4DVar gives a more reliable ash fields in layers (Fig. 4.3) as advisory information.

Additionally, free forecasts are conducted using the state fields at the end of assimilation time (19:00 UTC, April 14, 2010, in this experiment) as initial condition and emissions in Table 2.2 for further forecast (till 10:00 UTC, April 15, 2010, in this experiment). Results show that initial condition computed with a more accurate emission yields a more faithful forecast (Fig. 4.5). It can also be observed that ash clouds between Fig. 4.5(c) and Fig. 4.5(d) are more distinguishable in terms of the shapes and values than those between Fig. 4.4(c) and Fig. 4.4(d). This is because although they bear a great resemblance from the top view at one moment, the ash clouds locate in different altitudes, and will eventually transport in different patterns due to the meteorological fields . It confirms the conclusion in section 3.4.3 that an inaccurate estimate of vertical distribution is likely to result in a misleading forecast in the long run.

4.4. Summary and conclusions

Satellite observations of ash columns create SICs between the state variables in a column, which will lead to low convergence rate and ineffective estimates of volcanic ash emissions when standard 4D-Var (Std4DVar) approach is employed. In order to solve the ineffectiveness problem, a trajectory-based 4D-Var (Trj4DVar) approach was proposed. The approach perturbs the input parameters one by one and computes different trajectories resulted from the perturbations. Then it reformulates the cost function to seek the optimal linear combination of trajectories, which forms an ash-column field that fits the observations the most. It benefits from the fact that the wind fields change with altitude and the shapes of the trajectories differ from each other. It does not lose meteorological information as regular 4D-Var cost function does. In the reformulated cost function, the impact of SICs between the parameters being calibrated (coefficients for the linear combination of the trajectories) has been reduced.

In addition, Trj4DVar approach is adjoint free, so it does not require the implementation of the adjoint of the tangent linear model. This is a very attractive feature of the new approach. However the computational effort required for the modified 4D-Var method increases fast with the number of parameters. Therefore, an acceleration technique was discussed to solve the problem of large computational costs.

Twin experiment was conducted using the same set-ups as in chapter 3 so that comparison could be made between using Std4DVar and using Trj4DVar. Trj4DVar showed good performance in the estimation of the emissions with a perfect model. However, ill-conditioned physical condition with similar wind fields in each layer can lead to a set of similar snapshot observations and resulted in an unstable solution. Therefore, regularization terms were introduced in the cost function to include additional information.

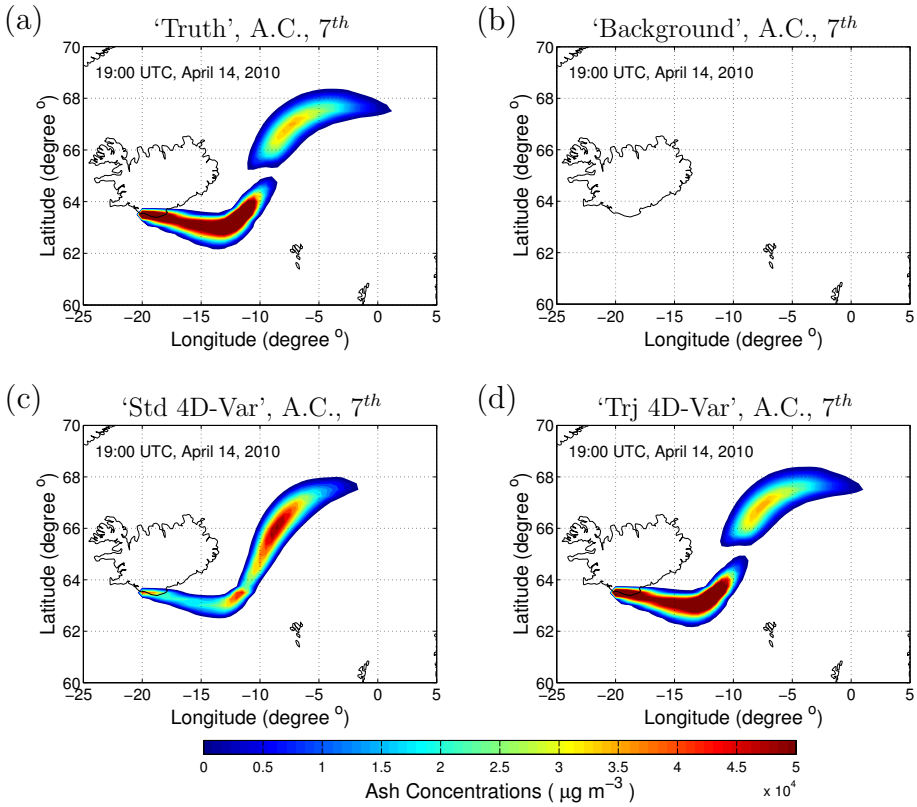

Figure 4.3: Ash concentrations at the 7^{th} layer above summit of initial condition after assimilation at 19:00 UTC, April 14, 2010: generated with emission rates for the first 10 hours of (a) the 'truth', (b) the 'background', (c) 'estimated' through standard 4D-Var method and (d) the 'estimated' through Trj4Dvar method.

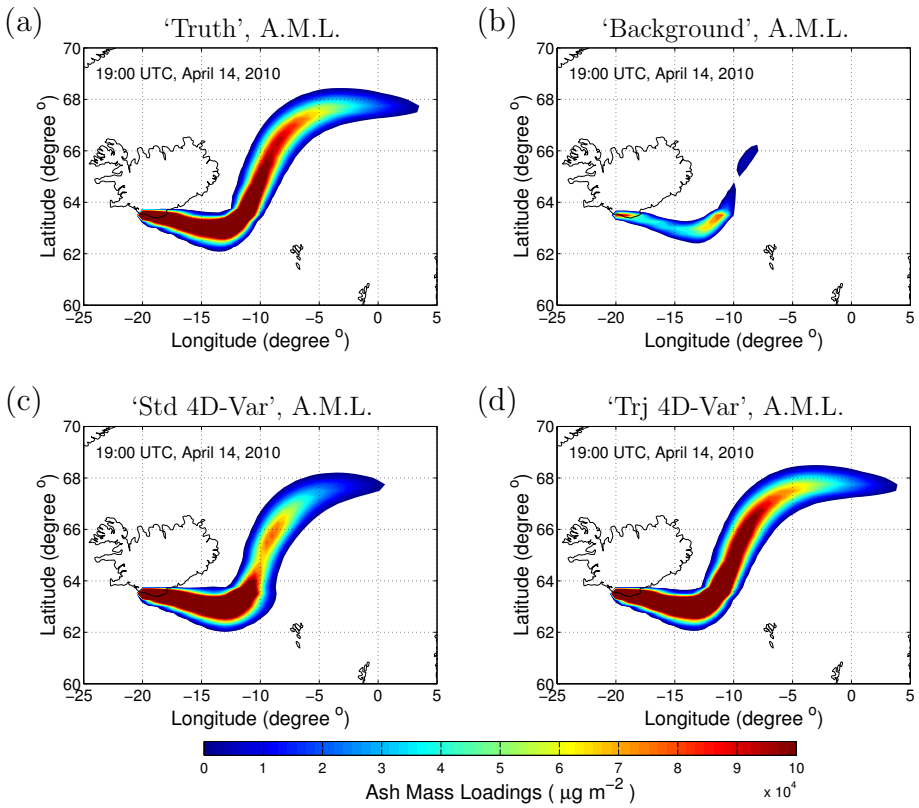

Figure 4.4: Ash columns of initial condition after assimilation at 19:00 UTC, April 14, 2010: generated with emission rates for the first 10 hours of (a) the 'truth', (b) the 'background', (c) 'estimated' through standard 4D-Var method and (d) the 'estimated' through Trj4Dvar method.

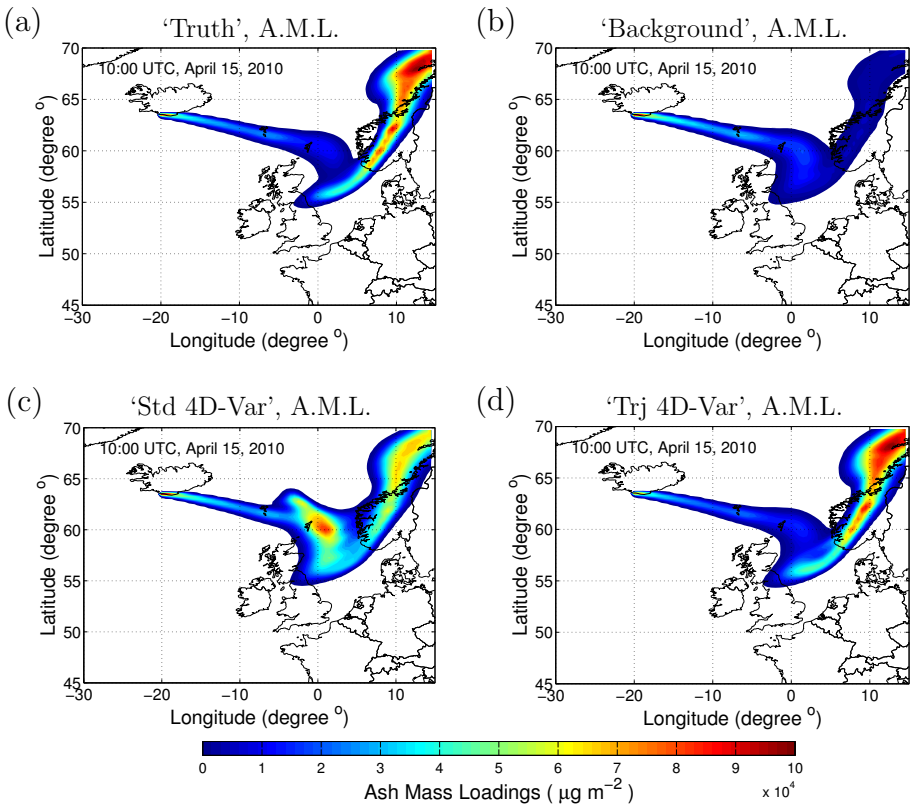

Figure 4.5: Ash columns of free forecasts after assimilation at 10:00 UTC, April 15, 2010: generated with emission rates for the first 10 hours of (a) the 'truth', (b) the 'background', (c) 'estimated' through standard 4D-Var method and (d) the 'estimated' through Trj4Dvar method.

A stochastic model was also used to test the performance of Trj4Dvar method. Although the estimates basically preserve the vertical profile of the true emission rates, oscillations in solution occurred with noise, and large noise led to large oscillations. Regularization helped to smooth the solution and improve the estimation accuracy. With a larger assimilation window, more observations were available, which diminished the influence of noise and resulted in a more stable and accurate solution. Moreover, in the case of larger assimilation window, the regularization had less impact on the solution, and thus the more accurate solution could be better preserved. However, enlarging assimilation window would cause an polynomial increase in computational expense, and trade off should be made between a more accurate estimation and less computational effort.

The Trj4DVar method has been shown to be able to produce satisfactory estimates using a simplified model and yet one has to test it on realistic models and real-life volcanic ash emissions. Next chapter will focus on application to real data with a full model including other physical ash transport processes besides advection and diffusion, such as dry deposition and wet deposition.

5

Modified trajectory-based 4D-Var to integrate ground-based observations: twin experiment

In the previous chapters, it has been show that an accurate determination of the injection layer, where the ash is emitted into the atmosphere, is crucial for the forecast of volcanic ash clouds. Trj4DVar was implemented and it has shown improved performance compared to Std4DVar in twin experiments using synthetic satellite observations. However, there are some cases with real satellite data where Trj4DVar has difficulty in obtaining an accurate estimation of the injection layer. To remedy this, Trj4DVar is modified to reconstruct the vertical profile of volcanic ash emissions by assimilating observations of PH along with satellite data. The modified approach is tested with synthetic twin experiments in this chapter. The results show that the modified Trj4DVar is capable of accurately estimating the injection height (location of the maximal emission rate) by incorporating the PH (top of the ash plume) and MER data obtained from ground-based observations near the source into the assimilation system. This will produce more accurate emission estimations and more reliable forecasts of volcanic ash clouds.

Parts of this chapter have been published in:
Lu, S.*, Lin, H.-X., Heemink, A., Segers, A., and Fu, G. (2016). Estimation of volcanic ash emissions through assimilating satellite data and ground-based observations. ***Journal of Geophysical Research: Atmospheres*** 121, 18, 10,971-10,994, 2016.

5.1. Introduction

In the previous chapters, it has been discussed that Std4DVar is unable to reconstruct the vertical profile of volcanic ash emissions. The failure is attributed to the ill-conditioning problem caused by the lack the vertical information in satellite data. To deal with the problem, the Trj4DVar approach was proposed. Trj4DVar reformulates the cost function in a regression type which computes the total difference between observed ash columns and a linear combination of simulated trajectories coupled with a priori emission knowledge ('background' term). To construct the cost function, it decomposes the system into subsystems which represent source-receptor relationships to each source term (ash injection at each layer), thus it does not lose vertical information as Std4DVar does. This approach has been tested in the twin experiments using a simplified model. The results showed that it was capable of estimating the input emission column when a large assimilation window (> 6 hours) is used for most of the time. The twin experiments were repeated where different values of noise were given in the synthetic observations or perturbations were used in the meteorologic data. The outcomes show that there is still a small possibility that Trj4DVar fails to determine the injection height accurately. Being disturbed by the weather condition (light and cloud, etc) at that moment, satellite instrument can be hampered to observe the ash cloud, which may increase the possibility of failure for the use of Trj4DVar.

Information about the Plume Height (PH) and the Mass Eruption Rate (MER) are available for some extensively monitored volcanoes from ground-based, airborne and space-borne measurements. PH can be observed from the ground by weather radar, Lidar and web-cam (Lacasse *et al.*, 2004; Arason *et al.*, 2011; Mona *et al.*, 2012; Flentje *et al.*, 2010; Ansmann *et al.*, 2010). Aircrafts and weather balloons have provided in-situ measurements of PH with high temporal resolution and accuracy (Weber *et al.*, 2012; Petäjä *et al.*, 2012). For unmonitored or hardly accessible volcanoes, one still has to rely on satellite data. Zakšek *et al.* (2013) has recently developed a photogrammetric method to determine the height of the volcanic ash cloud through simultaneous retrieval of optical data from polar orbiting and geostationary satellites. In addition, the 'trajectory-matching' method in Flemming and Inness (2013) can be used to automatically estimate injection height and MER as a part of the DA process. This provides a new possibility to increase the accuracy of estimation results by integrating the information of PH and MER into DA systems.

Observations of PH have already used in an indirect way to estimate volcanic ash emissions for predictive purposes (Mastin *et al.*, 2009a) as mentioned in chapter 1 and 2. MER can be determined using an empirical relationship between plume height above the vent and total volume (Mastin *et al.*, 2009a). Emission plume can be computed combining the PH, MER and a presumed vertical distribution. However, this approach is not always feasible. Firstly, the plume height observations are often not available, and secondly, the empirical relationship is loose. Furthermore, one of the main limitations of this approach is that it does not provide an estimate for the vertical distribution of the emissions, which can vary substantially. Mastin *et al.* (2009a) also provide estimates of the fraction of total emitted mass carried by small particles ($< 63\mu$m diameter), which is termed as 'fine ash fraction'. These

fine particles are known to be able to survive early fall out near the source (Rose *et al.*, 2001). A limitation of using this fine ash fraction is that the fraction values can vary a lot ranging from 2% to 60% depending on the type of volcano, and the assumption on this strongly affects the forecasts of fine ash.

In this chapter, a modification of Trj4DVar is proposed in order to be able to estimate emission rates using a combination of satellite ash mass loading data and information of PH and MER. Twin experiments are designed based on the eruption activity of Eyjafjallajökull in April 2010. In order to make it more realistic, the full LOTOS-EUROS model is used and the synthetic observation are generated according to the retrieval products of SIVIRI data (say effective radius and AML). Instead of fine ash fraction, we use the Satellite-Constraint Ash Fraction (SCAF) which defines the emitted mass fraction carried by the particles with radii ranging from 1 μm to 16 μm constrained by SEVIRI retrievals. Studies show that very fine particles ($<$ 30 μm diameter) with extended atmospheric residence present the greatest hazard (Rose and Durant, 2009). Therefore, the SCAF in this case is also good to simulate the distal part of the ash cloud ($>$ 500 km from the source or $>$ 6 hours travel time) in long-range forecasts (Dacre *et al.*, 2013).

This chapter has been organized as follows: Section 5.1.1 presents two modifications on Trj4DVar to integrate ground-based observations PH and MER for a better estimation of injection layer. In section 5.2, the modified Trj4DVar is tested in twin experiments, besides, its influence on the estimates of the emissions and the forecasts of ash cloud is discussed. The last section briefly summarizes this chapter.

5.1.1. Incorporating MER and PH information in Trj4DVar

Trj4DVar has been presented to estimate emission rates from ash mass loadings based on the concept of 4D-Var and a trajectory matching approach. Trj4DVar seeks an optimal linear combination of trajectories generated with different inputs (emission) to fit the observation data as good as possible, by minimizing a reformulated 4D-Var cost function (4.2) (see section 4.2.1).

In an ideal situation, with a perfect model and exact observations, Trj4DVar can accurately estimate the parameters, however, it encounters difficulty in dealing with real satellite data with a large uncertainty. In this chapter, we propose two schemes of integrating the additional information of PH and the MER in the DA process to enhance the estimates. The idea is to restrict the sum of emission rates at all layers to the value of MER and the maximal emission rate to be at the injection layer. The injection layer is calculated with observations of the PH. The two modifications are defined as follows:

1. Penalty term correction: add penalty terms containing additional information to the cost function:

$$J(\boldsymbol{\beta}) = J^o + J^b + J^p, \tag{5.1}$$

where J^o, J^b are defined in Eq. (4.2). The penalty term J^p restricts most of the emission products to the injection layer and restricts the MER to the observations (such as the satellite mass loadings). For instance, in the twin experiment of this chapter, we compute the total mass loading from satellite retrievals (summation of

mass loadings at all pixels) at the beginning of the assimilation time m_0, and at the end of the assimilation time is m_{Nt}. The satellite-constraint MER can now be roughly calculated as:

$$MER = \frac{m_{Nt} - m_0}{t_N - t_0}, \tag{5.2}$$

We assume a fraction f_m of this MER distributed at the injection layer indexed by i_h and assume the summation along the emission column $\boldsymbol{u}$ equal MER as follows:

$$J^p(\boldsymbol{\beta}) = \alpha_h(\boldsymbol{u}^T\boldsymbol{e}_{i_h} - f_m * MER)^2 + \alpha_m(\boldsymbol{u}^T\boldsymbol{\epsilon} - MER)^2, \tag{5.3}$$

where α_h and α_m are weight factors, the unit vector $\boldsymbol{e}_i$ is a vector with the i^{th} element equals 1, all others are 0, and $\boldsymbol{\epsilon}$ is a vector filled with ones. Note that the calculation of MER (5.2) does not take removal processes (such as sedimentation) into account. A better MER can be achieved by using a combination of satellite observations and other types of observations. This MER is constrained by the limitations of satellite retrieval of ash to a certain size range within the Satellite-Constraint Ash Fraction (SCAF). In order to obtain a reasonable model forecast after the assimilation, the emitted MER including all particle sizes should be corrected by the SCAF.

2. Background term correction: generate a new emission based on the additional information and substitute it for the background

$$J(\boldsymbol{\beta}) = J^o + \alpha_b \left(\boldsymbol{u} - \boldsymbol{u}^{b,new}\right)^T [\mathbf{B}^{new}]^{-1} \left(\boldsymbol{u} - \boldsymbol{u}^{b,new}\right) = J^o + J^{b,new}, \tag{5.4}$$

where $\boldsymbol{u}^{b,new}$ is calculated according to the additional information of PH and MER with a predefined vertical distribution. The new error covariance matrix $\mathbf{B}^{new}$ represents the uncertainty of $\boldsymbol{u}^{b,new}$ that should be smaller than $\mathbf{B}_k$. The vertical distribution could be based on explicit assumptions, such as uniform-distributed (Dacre *et al.*, 2011), umbrella-shaped (Stuefer *et al.*, 2013; Webley *et al.*, 2012), Poisson-distributed, exponentially-distributed plume (Searcy *et al.*, 1998), or based on characteristics of the current eruption type.

Note that, the thickness of injection layer does not necessarily cover only one layer depending on the vertical extent. Or there can be multiple peaks of the vertical distribution of the emission rate due to the frequent changing of PH. Therefore, the injection layer in the two modifications should be extended to multiple layers according to the observations. Besides, the background term J^b in the formula of the penalty term correction (5.1) can also be replaced by $J^{b,new}$ in formula (5.4). In the experiments, the original J^b is used to include the influence of a priori information since the injection height value is uncertain as mentioned in the introduction of this chapter.

In order to determine the weight factors α_m, α_h and α_b, two schemes are considered as following. One is based on the uncertainty of the additional information, and the weight factors are chosen as:

$$\alpha_m = c1_m, \quad \alpha_h = c1_h, \quad \alpha_b = c1_b. \tag{5.5}$$

where $c1_m$, $c1_h$ and $c1_b$ are constants. The other is based on the accumulative influence of the uncertainty in each time step, thus the weight factors are linearly related to the length of assimilation window as

$$\alpha_m = c2_m * Nt, \quad \alpha_h = c2_h * Nt, \quad \alpha_b = c2_b * Nt, \tag{5.6}$$

where $c2_m$, $c2_h$ and $c2_b$ are constants. Values of $c1_m$, $c1_h$, $c1_b$, $c2_m$, $c2_h$ and $c2_b$ depend on the uncertainties of observations of PH and MER.

5.2. Twin experiments and discussion

Twin experiments are designed to test the performance of the Trj4DVar approach and the impact of integrating the injection height and the total mass loading in the DA system. The experiments are carried out using the Eyjafjallajökull 2010 eruptive event as a case study.

5.2.1. Experimental setup

In the twin experiments, we estimate the emission rates from the background emissions and the observations. The synthetic observations are generated hourly by summing up the mass loadings from ash concentrations of all the last 3 tracers in Tab. 2.3 (see section 2.4), to which the SEVIRI instrument is sensitive. These ash concentrations are computed using the full LOTOS-EUROS model (see section 2.2) with true emissions, which are calculated according to the PH and MER given in Tab. 2.2 (section 2.4). 50% Gaussian noise is added to the data according to the uncertainty in the retrieval of satellite data as suggested by Wen and Rose (1994) and Fu *et al.* (2015). The background emissions are computed with an overestimation of MER. This cautious approach is recommended in practice for advising commercial jet operations in airspace affected by volcanic ash. A correspondingly higher PH is used according to the empirical formula (1.1).

For the construction of $\mathbf{R}_k$ and $\mathbf{B}$ in the cost function (Eq. (4.2)), 50% uncertainty is assumed in both observations and parameters with $\mathbf{R}_k$ and $\mathbf{B}$ in form of a diagonal matrix $\mathbf{R}_k^{-1} = (1/\sigma_k^o)^2\mathbf{I}^o$ and $\mathbf{B}^{-1} = (1/\sigma^b)^2\mathbf{I}^b$. To compare the influence of the assimilation window length on the estimates, assimilation windows of 1, 3, or 6 hours are used. Using a larger assimilation window implies that more observations are incorporated. During one episode the eruptive parameters are assumed to be constant. All assimilation windows are shorter than the eruption episodes. In practice, an assimilation window of constant length should be used within one episode.

PH information retrieved by Icelandic Meteorological Office (IMO) is integrated in the construction of correction terms. The height of the plume was monitored every 5 minutes with a weather radar located in Keflavík International Airport, at 155 km distance from the volcano. PH (echo top altitude) is calculated from the volume reflectivity data with a lowest altitude limitation of 2.9 km, which is archived at the IMO. Fig. 5.1 shows the time series and the 6-hour averages constructed from the radar detected echo tops by IMO, taken from Arason *et al.* (2011). To generate the penalty term and the new background term as described in section 5.1.1, $f_m = 0.8$

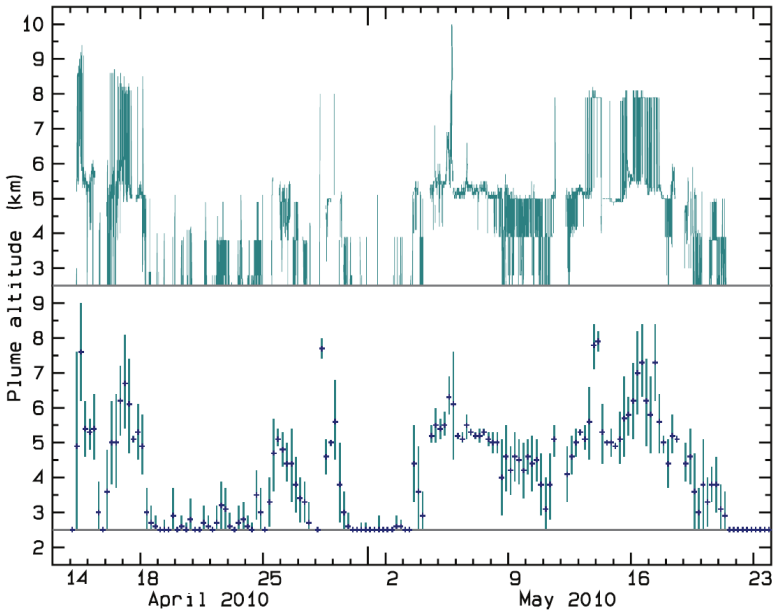

Figure 5.1: Additional information of plume height obtained from a weather radar provided by IMO, taken from Arason *et al.* (2011). Upper panel: The 5-min time series of the echo top radar data of the eruption plume altitude (km). Lower panel: The 6-hour averages of the echo top heights of the eruption plumes (km) with the bars representing the standard deviation.

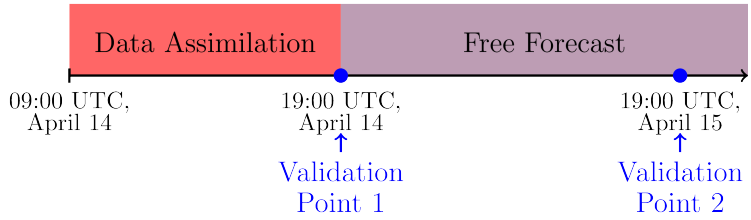

Figure 5.2: Timeline of twin experiment.

is used in the penalty term. This value is based on experience. It means that 80% of the MER is assumed to be distributed at the injection layer. The injection layer is computed according to the PH information from the IMO observations. To make it more realistic, this MER is computed by applying formula (5.2) to the synthetic observations, not the MER of the 'truth' in Tab. 2.2. To compare the two modifications, the new background term is calculated correspondingly with 80% of MER distributed at the injection layer and 20% of MER evenly distributed across other layers above the summit.

To test the impact of the estimate on the forecast, results with respect to the initial condition and the free forecast are computed. Data assimilation is iteratively applied with a 1h assimilation window till the end of the first episode at 19:00 UTC, April 14. The initial condition, which is the initial state field for the forecast run, is computed using the model with estimated emissions as reconstructed at the end of the assimilation. A forecast with the prior emission using this initial condition, denoted as 'free forecast', is computed for the next period of 24 hours. The result of the free forecast is given at 19:00 UTC, April 15. The timeline is shown in Fig. 5.2.

5.2.2. Estimates of emission and discussion

To test the impact of incorporating the additional information on the accuracy of the estimates, we use different assimilation windows and the two schemes of weighting the correction terms as mentioned in section 5.1.1. The results are shown in Figure 5.3, where 'estimated' represents the solution obtained from cost function (4.2) with only ash-column observations and the assumed background, 'est_pc' represents the solution of cost function (5.1) with penalty term correction, 'est_bc' represents the solution of cost function (5.4) with the background term correction, and 'bg_new' represents the new background emission used in the background term correction.

First, we evaluate the impact of incorporating additional information. It can be observed that large oscillations occur in the estimated solution and it may even be impossible to identify the injection height correctly (Figs. 5.3 (a) or (d)). This might be caused by the meteorological fields where some layers have similar meteorologic patterns, by the large uncertainty in observation data or by the nonlinearity in the volcanic ash model. The estimates with penalty term (est_pc) or new background

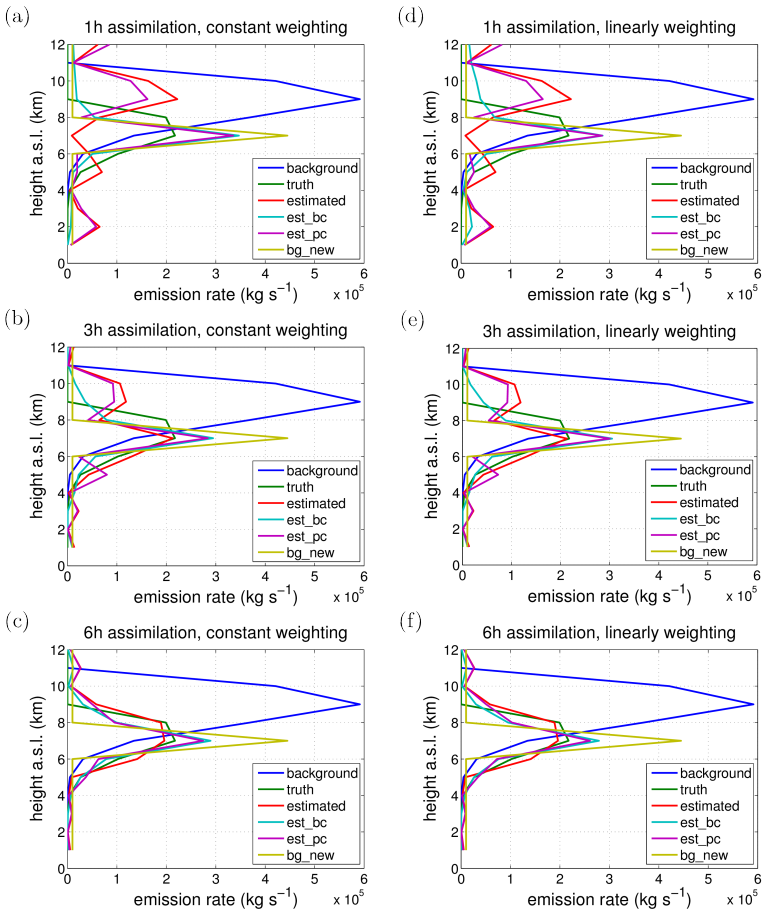

Figure 5.3: Estimation of the vertical profile of the volcanic ash emission at 19:00 UTC, April 14, 2010, using modified Trj4DVar. Figures in the left column are computed with constant weight factors (α_m and α_h) and in the right column with weight factors as linear functions of the length of assimilation windows: using assimilation windows of 1h in (a) and (d); 3h in (b) and (e); and 6h in (c) and (f).

term (est_bc) are significantly more accurate. Both ways of adding information work well in order to restrict the injection height (comparing estimated against est_pc or est_bc in Figs. 5.3 (a) or (d)). We can also notice that est_pc is closer to estimated at the layers other than the injection layer. Therefore, when estimated is reliable, penalty term correction is recommended to achieve a more accurate vertical profile than using background term correction. Note that the use of correction terms aims at capturing the injection layer. The maximum emission rates might be an underestimation or, in this case, an overestimation of the truth. Therefore, f_m in cost function (5.3) and the weight factors (α_h, α_m in Eq. (5.1) and α_b in Eq. (5.4)) should be adjusted to change the influence of the correction terms.

Second, we consider the influence of the length of assimilation window to the estimation results. By comparing estimated solutions in one column (for instance, Figs. 5.3 (a), (b) and (c)), it can be observed that when the assimilation window is enlarged oscillations are decreased and emissions are estimated more accurately. Especially the injection height and the basic shape of the profile are preserved in the 6h situation. Moreover, the influence of the background (a priori information) on the estimates reduces with an increasing assimilation window, since the estimates are improved and consequently the importance of the background is decreased (Figs. 5.3 (a), (b) and (c)).

Finally, the impact of the weights of the correction terms (α_h, α_m in Eq. (5.1) and α_b in Eq. (5.4)) is analyzed. By comparing the figures in one column, we observe that the influence of the additional information decreases with the length of assimilation window when constant weight factors are used (Figs. 5.3 (a) - (c)), and the influence remains the same when the other set of weight factors is used (Figs. 5.3 (d) - (f)). A constant weighting scheme is recommended when AML has a large uncertainty, since it makes the solution closer to the estimated solution when the assimilation window is enlarged and the accuracy of estimated is improved. Linear weight factors with small values are recommended when AML has a small uncertainty. Note that, the weighting schemes are provided for assimilation windows with adjustable length. They are not considered when assimilation windows with constant length are used.

5.2.3. Forecasts of ash clouds

In this section, the predictive performance of the assimilation with or without the additional information of PH and MER will be analyzed.

As shown in the previous section, the original estimates and the estimates with correction terms differ more when using 1h assimilation window than larger assimilation windows. Therefore the forecasts using a 1h assimilation window will be better for illustrative purpose. We apply data assimilation sequentially with a 1h assimilation window during the first eruptive episode and simulate the model with the assimilation results until the end of the first episode (19:00 UTC, April 14, 2010). The ash columns after simulation, which can be regarded as the initial condition for the forecast run, are illustrated in the left column of Fig. 5.4. It can be noticed that both estimated results (Figs. 5.4 (c) and (d)) are significantly improved with the mass loadings much closer to the forecast with the true emissions (Fig. 5.4 (a)).

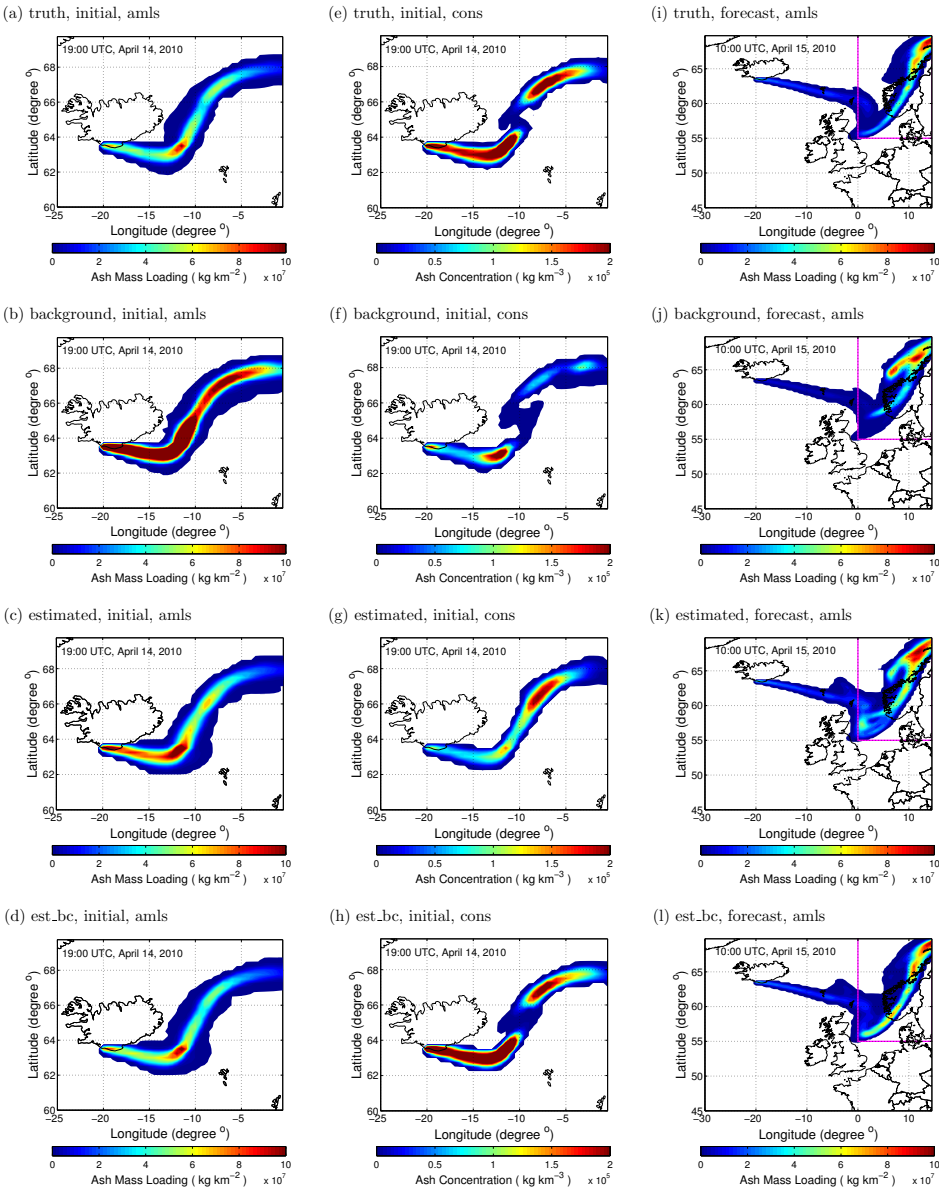

Figure 5.4: Comparison of the simulation results with assimilation and without assimilation. Figures in different rows represent results simulated with different emissions of: (a),(e) and (i) the truth; (b), (f) and (j) the background; (c), (g) and (k) the estimate with assimilation of PH and MER; and (d), (h) and (l) the estimate without assimilation of PH and MER. Figures in the left column are the AMLs of the initial conditions at 19:00 UTC, April 14, 2010. Figures in the middle column are the ash clouds at the 7^{th} layer over the vent of the initial condition, at 19:00 UTC, April 14, 2010. Figures in the right column are the AMLs of the free forecast at 10:00 UTC, April 15, 2010, initiated from 19:00 UTC, April 14, 2010.

Although the total column shows great resemblance, there are differences when looking into the details in each layer. This is because the wind fields change with the altitude, and the ash particles released at different layers transport differently. Therefore, each specific vertical profile of emissions will lead to a unique ash cloud which is distinguishable as shown in the initial conditions at the 7^{th} layer over the vent in the middle column of Fig. 5.4. This implies that, in practice, although ash clouds generated with poorly estimated emissions often appear to match the satellite image (Figs. 5.4 (e) and (g)), the interior 3D ash concentrations may be far from the truth (Figs. 5.4 (e) and (g)). However, with the incorporation of the additional information, both the ash mass loadings (comparing Figs. 5.4 (a), (b) and (d)) and the 3D ash fields (comparing Figs. 5.4 (e), (f)and (h)) improve a lot. This implies that the correction terms are able to improve the initial condition with a more accurate estimate of the emissions, resulting in a more reliable forecast. This is confirmed by the results in the right column of Fig. 5.4, which shows the free forecast until 10:00 UTC, April 15, 2010 simulated in the European domain with the same emissions and initial conditions as used for the model simulation in the left column of Fig. 5.4. The pink box marks the area where ash emitted from the first episode was transported to. We can see that the shapes and positions of ash clouds vary (Figs. 5.4 (k) and (l)) with different initial fields (Figs. 5.4 (g) and (h)), and apparently a better estimation of the emission leads to a more reliable forecast which is closer to the truth (Figs. 5.4 (i), (k) and (l)).

5.3. Summary and conclusions

Trj4DVar has been presented and tested on a simplified model previously. It was shown that this approach performed well with large assimilation windows and with synthetic observations of ash columns which can be regularly obtained in the whole domain. Given different observational noise or meteorologic condition, Trj4DVar may lead to a poor estimate with a 6-hour assimilation window, although only in very rare situations. This chapter illustrated a case where Trj4DVar was unable to accurately estimate the injection layer, and eventually resulted in a unreliable and misleading forecast.

Two modifications to Trj4DVar was thus proposed for a better estimation of the injection layer by incorporating observations of PH and MER in addition to AML data. They aim at restricting the sum of emission rates at all layers to the value of MER and restricting the maximal emission rate to be at the injection layer. One is adding a penalty term in the cost function for the restriction. The other is to replace the background term based on a priori knowledge with a new background term related to the PH and MER observations. The former is recommended when a priori information is with good accuracy or the vertical distribution have a large uncertainty. For instance, the plume extent can vary for different eruption type, and the thickness of the umbrella cap in the umbrella-shaped distribution (see section 2.3) should be adapted to this. Modified Trj4DVar was tested on the realistic (full) LOTOS-EUROS model and compared with straightforward Trj4DVar. Results showed that using modified Trj4DVar, the injection layer could be captured well and more accurate initial conditions were achieved. The forecast of ash cloud was also

improved. The approach should be further tested using real-life satellite data due to the complexity and insufficiency of the data.

6

Trajectory-based 4D-Var for volcanic ash problem: SEVIRI data experiment

In the previous chapters, Trj4DVar has been proposed based on the concept of 4D-Var assimilation approach and been enhanced to achieve more accurate estimates for our application. The modified Trj4DVar scheme has been tested on the full LOTOS-EUROS model using synthetic satellite-like ash columns, synthetic MER and weather radar observations of PH. This scheme was shown to be able to accurately determine the injection layer of an volcanic ash eruption plume. In this chapter, real-life field data is assimilated to explore the potential of applying the modified Trj4DVar in practice. Satellite data is more complicated to be used than synthetic data, therefore, the preprocessing of the data is presented before assimilation is conducted. Besides, the guidance and suggestions on the proper use of the data for assimilation are provided, which will result in a more reasonable estimate of emission and more reliable forecast than using the data directly without preprocessing.

Parts of this chapter have been published in:
Lu, S.*, Lin, H.-X., Heemink, A., Segers, A., and Fu, G. (2016). Estimation of volcanic ash emissions through assimilating satellite data and ground-based observations. ***Journal of Geophysical Research: Atmospheres*** 121, 18, 10,971-10,994, 2016.

6.1. Introduction

In the previous chapter, Trj4DVar was proposed for reconstructing the vertical profile of volcanic ash emissions by assimilating satellite AMLs. Using a simplified model, the method performed well with a 6-hour assimilation window in the twin experiments. When the full model is used, there are cases that the method is not able to provide a correct determination of the injection layer. Therefore, Trj4DVar has been modified to further incorporate PH and MER obtained from ground-based observations for a more accurate estimation of injection height. Results of the twin experiments using the full LOTOS-EUROS model showed good performance of the modified Trj4DVar, which implied that the approach was ready to be tested on a real-life case.

When it comes to using real-life field data, the situation is more complicated. The detection of volcanic ash can be disturbed by the weather condition such ash water vapor. This will result in observations of undetected or wrongly-detected ash. Besides, many sensors (such as UV and visible sensors) have limited temporal coverage which can only observe during daylight (see section 1.4). Due to the temporal and sometimes spatial insufficiency of the data, study is taken on how to use the data properly to benefit more and give a reasonable estimate.

This chapter is organized as follows. Section 6.2 gives a detailed description of the observations of the case study which are used in the experiments of this chapter. In section 6.3, a preprocessing procedure is provided to exclude pixels containing bad satellite data. In section 6.4, field data experiments are conducted using the preprocessed data, and a heuristic technique is presented to deal with the spatially insufficiency problem. A summary is given in the last section.

6.2. Observations for assimilation

We use the Eyjafjallajökull 2010 volcanic eruption event as a case study. The 39-day long eruption in April-May 2010 resulted in a dispersal of ash over a large part of Europe. It caused unprecedented disruption to air traffic and its implications on modern society have made Eyjafjallajökull 2010 a landmark event. Various techniques and observations have been used to detect the volcanic ash cloud, and provide unique data for various studies. In this chapter, we focus on the first explosive phase, 14-18 April.

6.2.1. SEVIRI ash mass loading data

Spinning Enhanced Visible and Infrared Imager (SEVIRI) (Schmetz *et al.*, 2002) is a 12-channel spin-stabilized imaging radiometer aboard the Meteosat Second Generation (MSG) platform, in geosynchronous orbit situated approximately over 0° longitude and 0° latitude. The total field of view coverage of the earth's surface and atmosphere is 70° from 70°S to 70°N and 70°W to 70°E. Measurements are made of spectral range from visible (500 nm) to the infrared (13400 nm) with a spatial resolution of 3 km $\times$ 3 km at the sub-satellite point and 10 km $\times$ 10 km at the edge of the scan. Images can be acquired in all channels for the whole of the 70° disk every 15 minutes.

Prata and Prata (2012) retrieved the ash mass loadings (AMLs) based on infrared channels for the case study of Eyjafjallajökull in a sub-region of the disk covering $40°$N to $70°$N and $30°$W to $30°$E. This region includes the geographic area affected by the Eyjafjallajökull volcanic ash. The data products from the SEVIRI ash retrievals contain estimates of mass loadings of particles with radii between $1\mu m$ and 16μm, the effective particle radius, and the retrieval errors in mass loadings at ash-detected pixels. In the Eyjafjallajökull dataset, 15 minutes samples were provided starting on April 14, 2010, 00:00 UTC and ending on May 22, 2010, 23:45 UTC. The 15 minutes pixel-by-pixel mass loadings were then binned into $0.1° \times 0.1°$ grid cells and time-averaged every hour. A parallax correction (Vicente *et al.*, 2002) was applied to all ash-detected pixels by first assuming that the ash clouds were at 6 km height. This simplification introduces a small error in geolocation, but is an improvement compared to using the data without a parallax correction. The data are the same as used by Stohl *et al.* (2011).

In our study, the data in the European continental domain (Fig. 3.3) is used for validation, while the data in the region of Iceland (area within the red box of Fig. 3.3) is used for the assimilation. The Iceland domain includes the area affected by the ash released within 6 hours, which is the maximal length of the assimilation window in our experiments.

6.2.2. Additional information of PH and MER

The ash plume was monitored by a doppler weather radar located in Keflavík International Airport. The radar was the only operational weather radar in Iceland during the eruption, which gave operational doppler scans from the beginning of the eruption towards the end of April. In case of a volcanic eruption within a radius of 240 km from the radar, the scanning strategy is to make 240 km reflectivity scans every five minutes (except at 5 and 35 minutes past the hour when 120 km doppler scans are made). PH (echo top altitude) is calculated from the volume reflectivity data with a lowest altitude limitation of 2.9 km. Gudmundsson *et al.* (2012) provided the 6-hourly mean and maximum values of the plume altitude based on Keflavík radar observations (Fig. 6.1(a)), which will be used in the field data experiment in section 6.4.

MER information was reported by Gudmundsson *et al.* (2012), shown in Fig. 6.1(b). The magma discharges were produced from combining information from tephra fallout maps and PH variations with time. The total volume for different periods is obtained from isopach maps on land and piecewise exponential decline outside Iceland. Gudmundsson *et al.* (2012) computed the 6-hourly discharge rate by applying the record of the PH to a scaled version of the empirical formula of Mastin *et al.* (2009a):

$$Q_i = 0.0564 k_i \left[\frac{H_{med} + H_{max}}{2} \right]^{4.15}. \tag{6.1}$$

Here Q_i ($m^3\ s^{-1}$) is the average magma discharge for the 6 hour interval. H_{med} and H_{max} are respectively the median and maximum values of the plume height

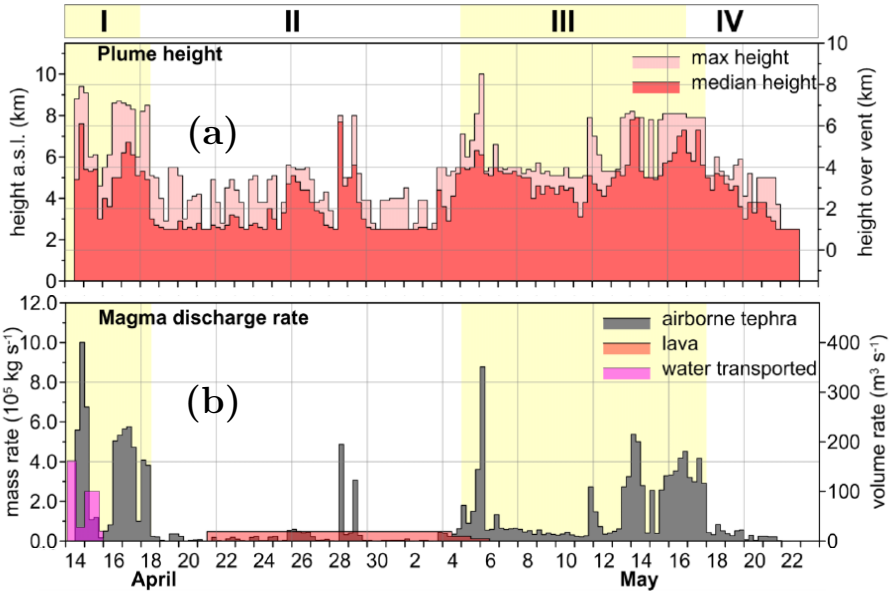

Figure 6.1: Eruption source parameters used for the field data experiment, taken from Gudmundsson *et al.* (2012). (a): Six hourly mean and maximum values of the plume altitude based on the weather radar in Keflavík. (b): Magma discharge based on combining plume and tephra dispersal data (6-hour average).

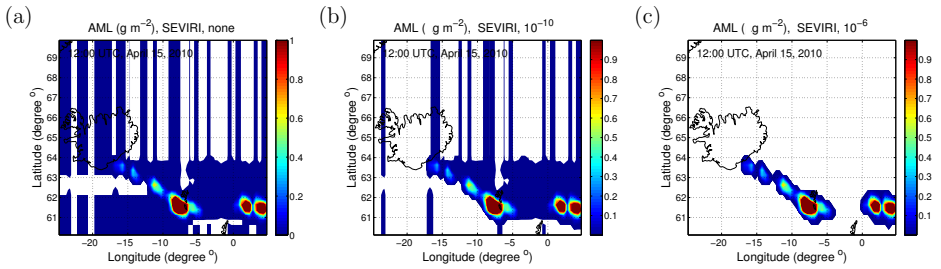

Figure 6.2: Preprocessing of SEVIRI data to remove retrieval noise with thresholds. (a) - (c) are the illustration of the retrieval noise (dark blue 'bands') and SEVIRI AMLs (g m^{-2}) filtered with different thresholds: (a) no threshold; (b) thr = 10^{-10}; and (c) thr = 10^{-6}.

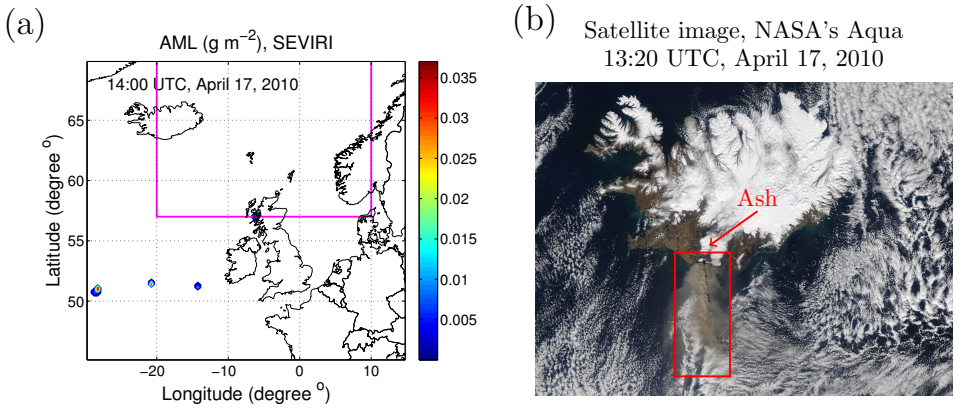

Figure 6.3: Illustration of an invalid detection of ash from SEVIRI retrievals: (a) AML of SEVIRI data; compared to (b) satellite image obtained by ASA's MODIS satellite.

over the vent for the interval. k_i is the scaling factor tuned in such a way that when integrated it yields values that fit the total ash volume estimates.

Note that the radar-observed PH value is not necessarily the injection height of the fine particles to be assimilated because the PH data bears a 20% uncertainty (Bonadonna and Costa, 2013). Microwave radar echoes are sensitive to coarse ash and lapilli concentrations (with size range from 2 to 64 mm in diameter), but not necessarily to moderate and light (< 5 g m^{-3}) fine ash distributions (Marzano *et al.*, 2011). Moreover, radar observes ash plume top height, which may not be where the maximal emission rate locates, leading to further inaccuracies.

6.3. Preprocessing of the SEVIRI data

To properly use the SEVIRI AML data, a threshold valued 10^{-6} (g m^{-2}) is adopted to screen out the invalid data below this threshold. The values below this threshold are set to zero in this study. Alternatively, they can be set to NaN or negative values. Noise is the result of the observational uncertainty of the instrument and

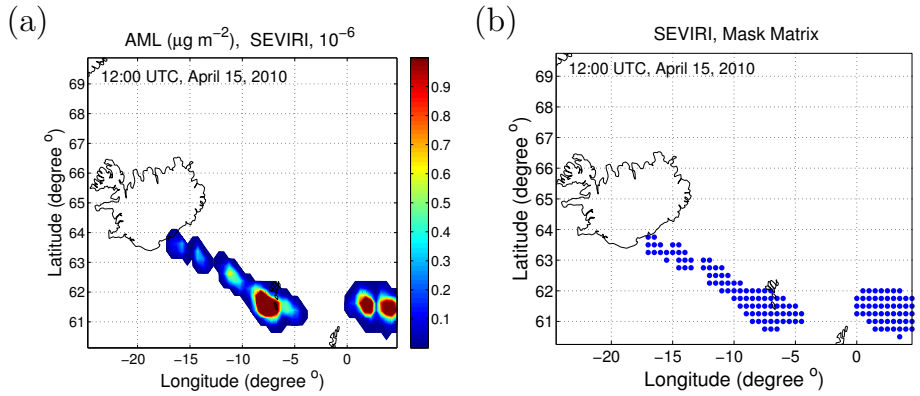

Figure 6.4: Illustration of a mask matrix to eliminate the influence of retrieval noise and invalid detection. (b) is the illustration of the mask matrix computed corresponding to (a).

the errors introduced by the retrieval algorithm. Fig. 6.2 (a) illustrates the noisy AML field of the original SEVIRI data, where the 'dark blue bands' indicate the noise resulted from the retrieval algorithm with the values above zero. Fig. 6.2 (c) shows the clean AML field used in the experiment. The threshold is manually tuned and selected based on experimental results, which is able to filter out the 'dark blue bands' while preserve most of the usable data.

Besides noise, invalid data can also be the result of undetectable ash or incorrectly-detected ash. Figs. 6.3 demonstrate a case of invalid ash detection. In the boxed area of Fig. 6.3 (a) there appears to be no ash detection from the SEVIRI data with zero values. However, NASA's MODIS satellite gives a clear observation of volcanic ash in the corresponding area (Fig. 6.3 (b)). In this case, assimilating the data of the entire domain or in the boxed area in Fig. 6.3 (a) will result in inaccurate estimates.

The original zero values (without being processed by the threshold) imply no ash detected, but it is difficult to determine whether that corresponds to really no ash in the real world. The use of the original zero to constrain the pixels without plume could be misleading and could influence the estimates negatively. Therefore, we only use the pixels where ash is clearly detected. To eliminate the disturbance of invalid data to the estimates, after the threshold is employed, a mask matrix is generated to select/mark the valid data area (pixels with values above zero). If the pixels containing original zeros are further confirmed and validated with extra knowledge to be no ash affected, these pixels can be marked so that the zeros will constrain where the plume should not be. An illustration of the mask matrix generated from Fig. 6.4 (a) is given in Fig. 6.4 (b) with selected pixels shown by blue dots. Consequently, the target of DA is to obtain the estimate of emission which will lead to an ash cloud matching the SEVIRI AML data the most in the selected area by the assimilation of preprocessed data above zeros.

6.4. Field data experiments

After having evaluated the method using synthetic data previously, now experiments with field data are conducted to explore the potentials of applying the method to realistic volcanic ash problems.

6.4.1. Experimental setup

The field data experiments is conducted on a PC with an Intel Xeon E3-1240 V2 processor with 8 cores, a total memory of 32 GB (approximately 5% was taken during experiments) and a clock speed of 3.4GHz. The full LOTOS-EUROS model is used. The background (a priori) emissions are calculated according to the PH and MER given in Tab. 2.2 (see section 2.4). The hourly-averaged mass loadings from the SEVIRI volcanic ash products are used to estimate the emission rates of the first eruptive phase of Eyjafjallajökull event. The validated data is available from 00:00 UTC, April 14, 2010 till 23:45 UTC, May 22, 2010. The data of 12:00 - 18:00 UTC, April 15 is used to carry out the assimilation, and future data is used to validate the results of the forecasts. The 6-hourly averaged PH and MER information shown in Fig. 6.1 is integrated in the assimilation process through the penalty correction and background correction methods. A 6-hour assimilation window is used since this has been shown as the best settings in section 5.2. We only use tracers of vash_4 - vash_6 in Tab. 2.1, because large particles will fall out of the ash plume very soon and will have little contribution to the forecasts. Furthermore, the SEVIRI instrument is sensitive to small particles with radii 1μm - 16μm (Prata and Prata, 2012). Subsequently, the value of MER to be assimilated is scaled with the SCAF accordingly. The SCAF value is a percentage of the total MER including particles ranged from vash_4 to vash_6.

6.4.2. Results with different estimation windows

In a typical assimilation process, the time range of the parameters to be calibrated (estimation window) coincides with that of the observations to be assimilated (observation window), represented by the assimilation window in Fig. 6.5 (a). In this section, an estimation window separate from the observation window is used as shown in Fig. 6.5 (b), and the performance of using different estimation windows is tested.

We assimilate the observations during 12:00 - 18:00 UTC, April 15, 2010. Fig. 6.6 gives a series of AML fields of SEVIRI to be assimilated. Notice that there is no valid data near the summit ($<$ 250 km from Iceland) in Figs. 6.6 (b) and (c) where newly emitted ash ($<$ 3 hours) should be transported to. Since the detected ash clouds (colored pixels) consist of emissions earlier than 12:00 UTC, April 15, 2010, it is not appropriate to estimate emissions after 12:00 UTC using this data. Therefore, an estimation window is computed by roughly tracing back the emission time from the valid data areas in the observation window according to the wind speeds. Note that the estimation window and observation window can overlap or can be totally different due to specific meteorological conditions.

The estimation results of applying both assimilation processes are given in Fig.

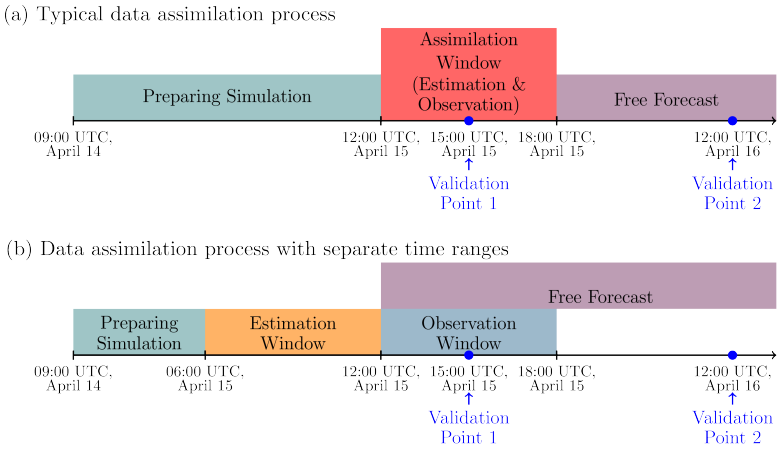

Figure 6.5: Timelines of real data experiment for: (a) typical assimilation process; and (b) assimilation process with separate time ranges.

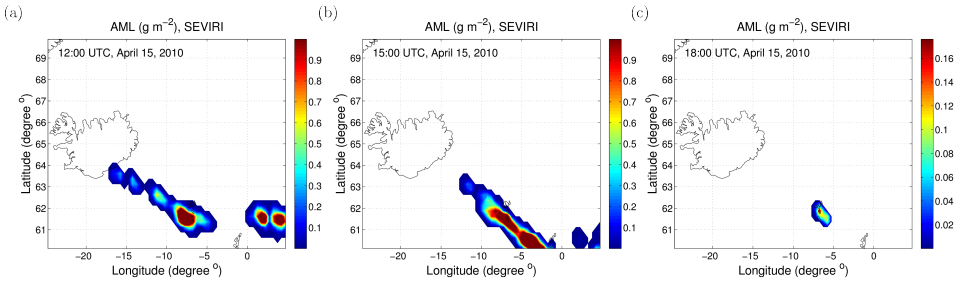

Figure 6.6: AMLs of SEVIRI during the observation window 12:00 - 18:00 UTC, April 15, 2010, chosen at time: (a) 12:00 UTC; (b) 15:00 UTC; and (c) 18:00 UTC.

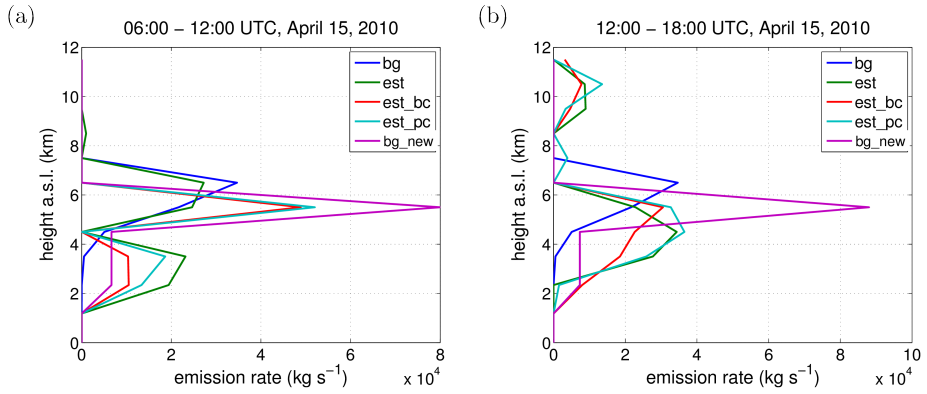

Figure 6.7: Estimation results of emissions during the estimation window of: (a) 06:00 - 12:00 UTC; and (b) 12:00 - 18:00 UTC, April 15, 2010.

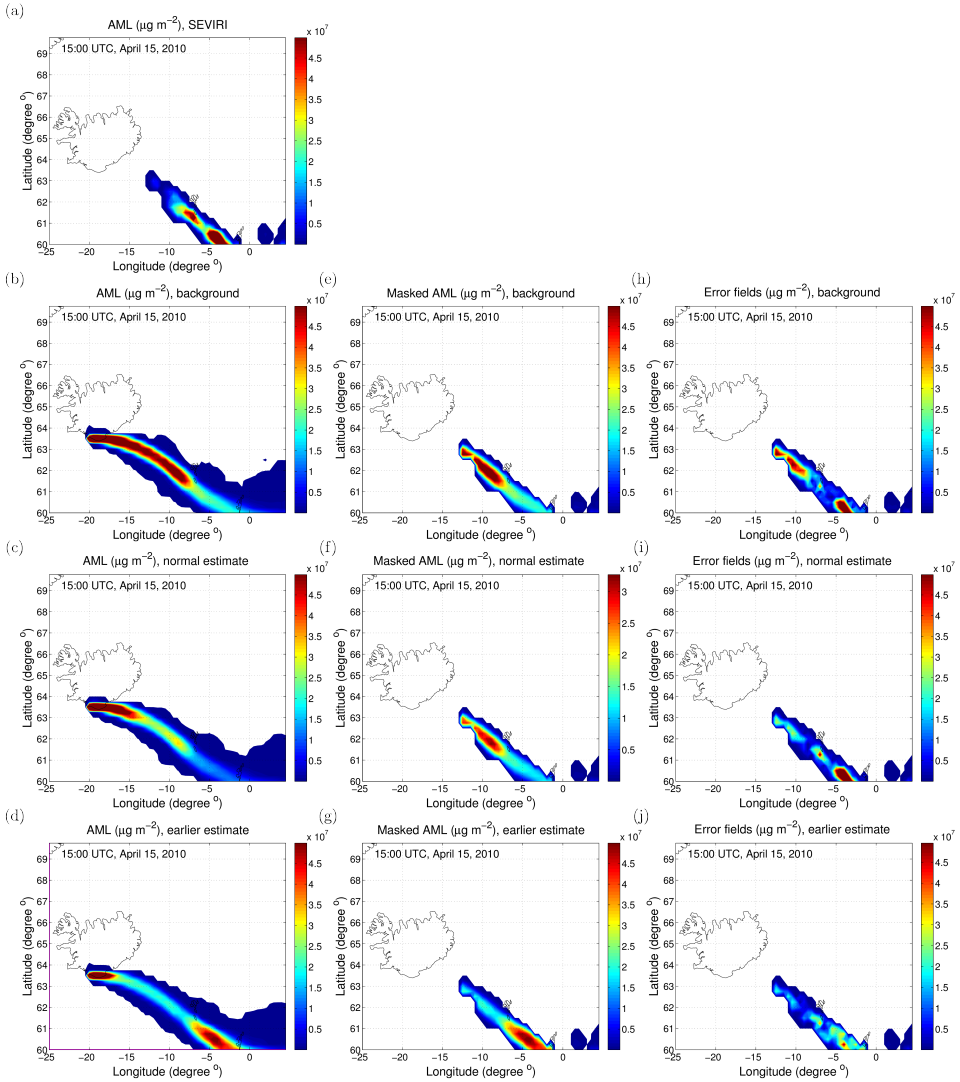

Figure 6.8: Initial conditions (AML) at 15:00 UTC, April 15, 2010, simulated with: (b) background emission; (c) normal estimate; and (d) earlier estimate. The middle column shows the AML fields of the left column in the masked area (colored pixels in (a)). The right column is the error fields of the middle column compared with (a) the SEVIRI AML fields.

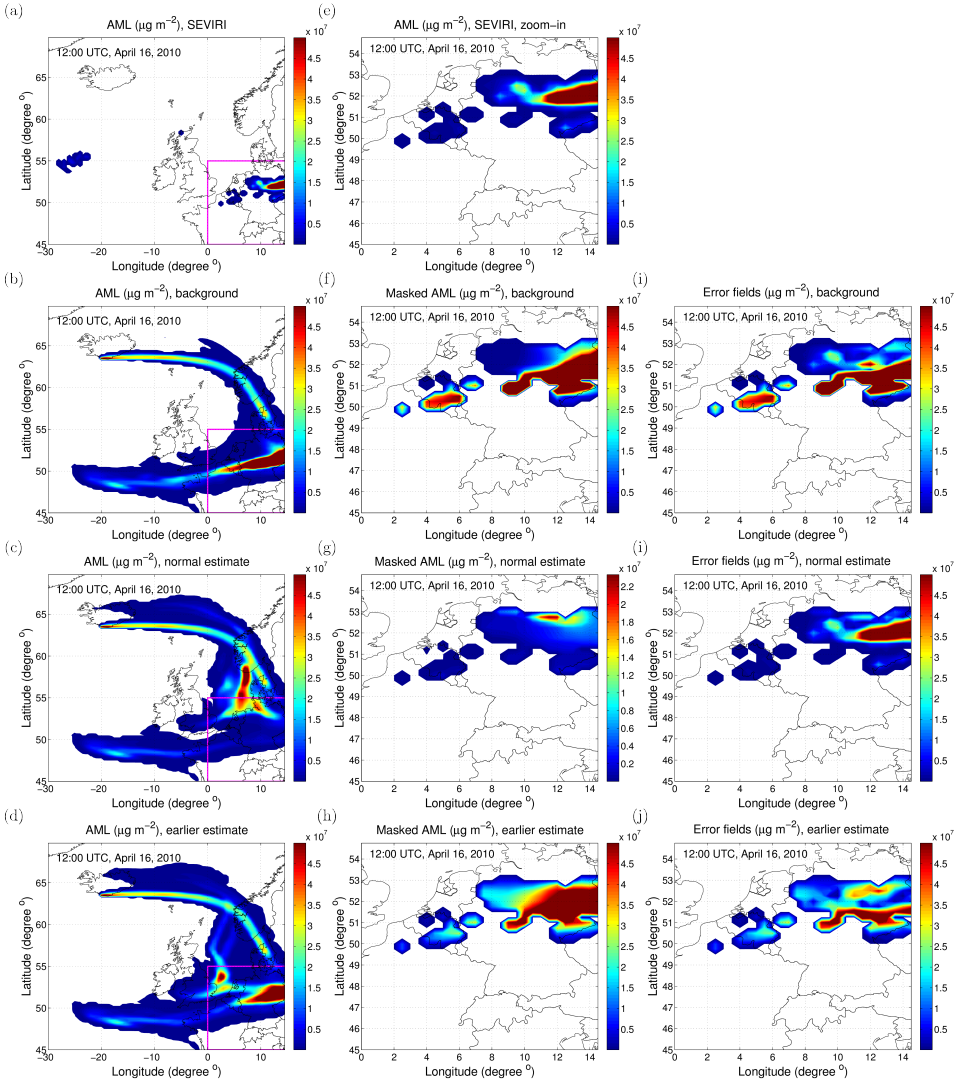

Figure 6.9: Free forecasts (AML) at 12:00 UTC, April 16, 2010, simulated with: (b) background emission; (c) normal estimate; and (d) earlier estimate. The middle column shows the zoomed-in AML fields of the left column in the masked area (colored pixels in (a)). The right column is the error fields of the middle column compared with (e) the SEVIRI AML fields.

6.7. Here, the estimate is denoted as 'earlier estimate' when using separate time ranges (with an earlier estimation window), and denoted as 'normal estimate' when using a typical assimilation time range. It is shown that both correction methods (est_bc and est_pc) will restrict the maximum of the emission rate at the injection height, 5.5 km in this case. This confirms the conclusion from the twin experiments.

The impact of using different estimation time ranges with respect to estimating the initial condition is explored. Usually, the initial condition is available when the free forecast starts, i.e. at the end of the estimation window. However, in this case, the two assimilation processes have different initial times for the free forecasts. For the purpose of comparison, a shared initial time at validation point 1 (15:00 UTC, April 15) is considered. This point is chosen because it should be later than 12:00 UTC so that the estimated emissions of both assimilation processes can influence the initial condition, and the masked area of SEVIRI should be large enough to clearly observe the influences.

The initial conditions are shown in Fig. 6.8. By comparing Figs. 6.8 (b), (c) and (d), we can see that both assimilations have influence on the initial condition However, the earlier estimate affects the whole masked area, while the normal estimate affects the tip in the Northwest of the masked area, since with the normal estimate ash cannot be transported that far in such a short period (compare the masked area in Figs. 6.8 (e), (f) and (g), and compare the error fields in Figs. 6.8 (h), (i) and (j)). This implies that the ash clouds in the masked areas of 12:00 - 18:00 UTC come mostly from the emission during 06:00 - 12:00 UTC.

The free forecasts till 12:00 UTC, April 16 (validation point 2) are shown in Fig. 6.9. It should be noticed that in the first column, forecasts show a large plume throughout the European domain (Figs. 6.9 (b) - (d)), but SEVIRI data shows no ash detected around Iceland (Figs. 6.9 (a)). It is difficult to determine which is correct since the free forecast is formed with the a priori emissions which have a large uncertainty, meanwhile no ash detected does not necessarily imply no ash presenting as illustrated Figs. 6.3. Therefore, the masked area is used for validation and the whole domain for a general comparison. It can be seen in the left column that the ash of earlier estimate has been transported to the masked area in the pink box, while the ash of normal estimate has only been transported there partly. Moreover, by observing the middle column and the right column, we can see that the earlier estimate corrects the whole masked area while the normal estimate hardly has influence in that area. This further confirms the conclusion that using the earlier estimation window is more proper in this case.

6.4.3. Results with different observational error covariance matrices

In this section, the effects of using different observation error covariance matrices in the field data case are compared. The earlier estimation window of 06:00 - 12:00 UTC in Fig. 6.5 (b) is used. The error covariance matrices are diagonally generated with 30%, 50%, 70% uncertainty, and the SEVIRI retrieval error data. Note that, theoretically, retrieval error data with high quality will provide a better latent information on the observational uncertainties than the Gaussian-distributed

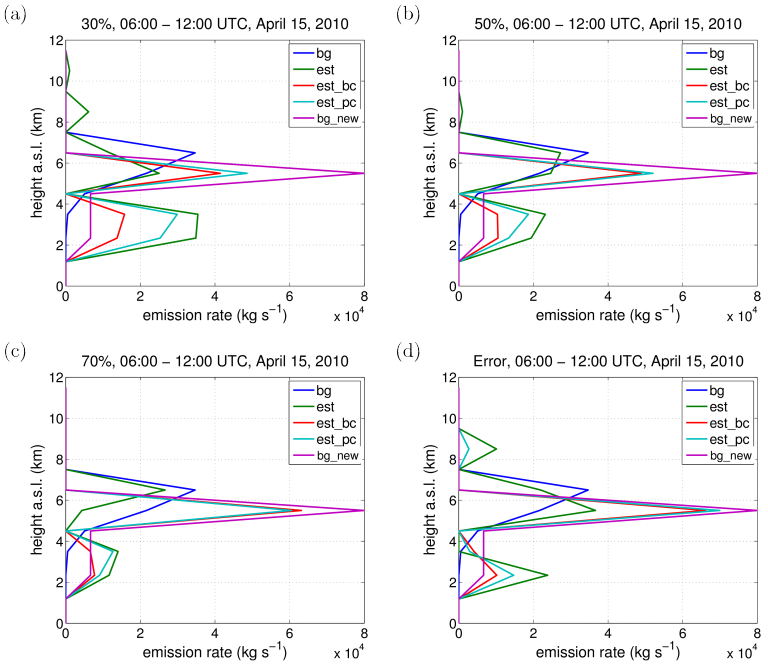

Figure 6.10: Estimation results of emission during 06:00 - 12:00 UTC, April 15, 2010, with observational error covariance matrices generated from: (a) 30% uncertainty; (b) 50% uncertainty; (c) 70% uncertainty; and (d) the SEVIRI retrieval error data.

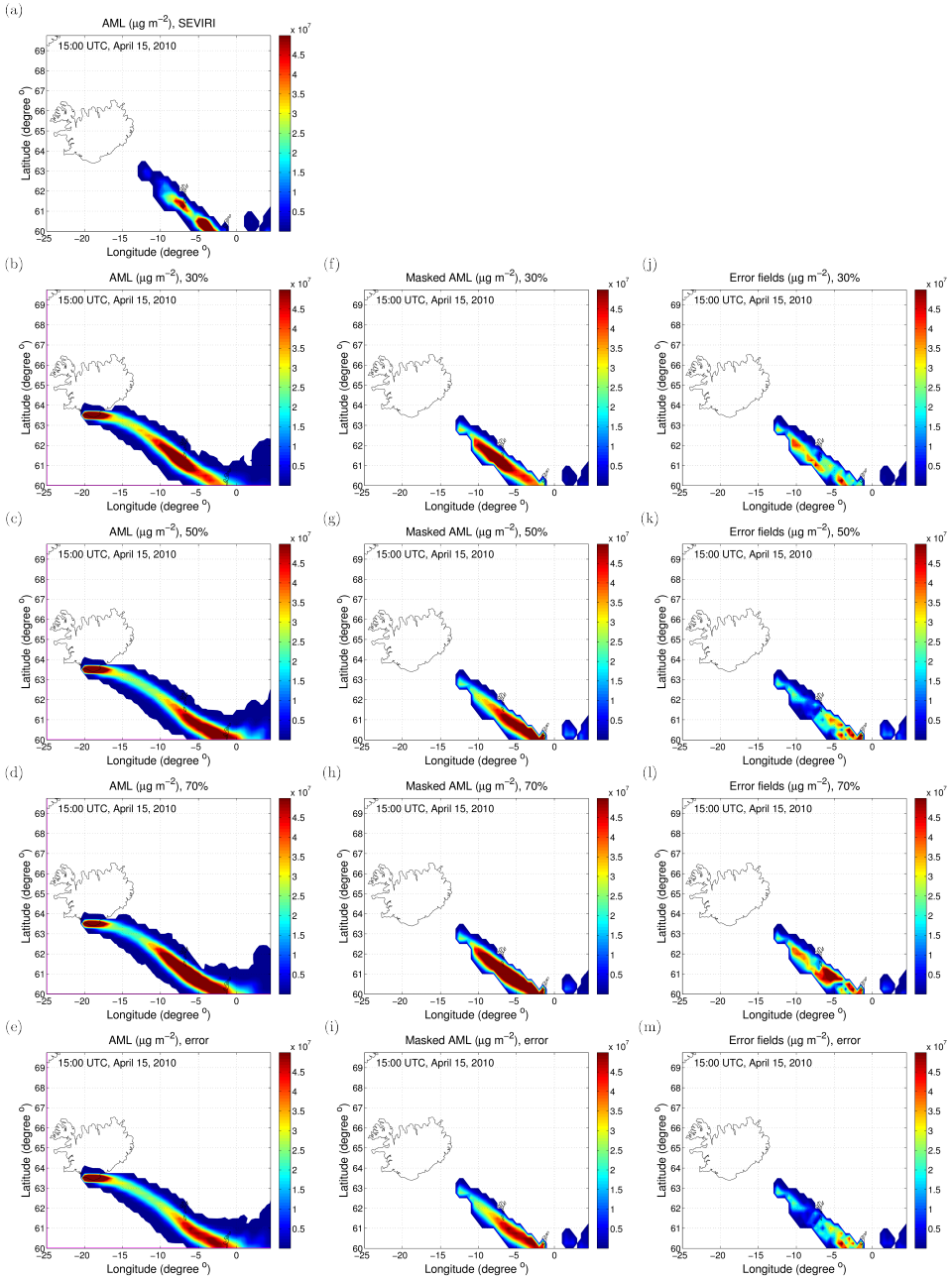

Figure 6.11: Initial conditions (AML) at 15:00 UTC, April 15, 2010, simulated with estimates of the observational error covariance matrices generated from: (b) 30% uncertainty; (c) 50% uncertainty; (d) 70% uncertainty; and (e) the SEVIRI retrieval error data. The middle column shows the AML fields of the left column in the masked area (colored pixels in (a)). The right column is the error fields of the middle column compared with (a) the SEVIRI AML fields.

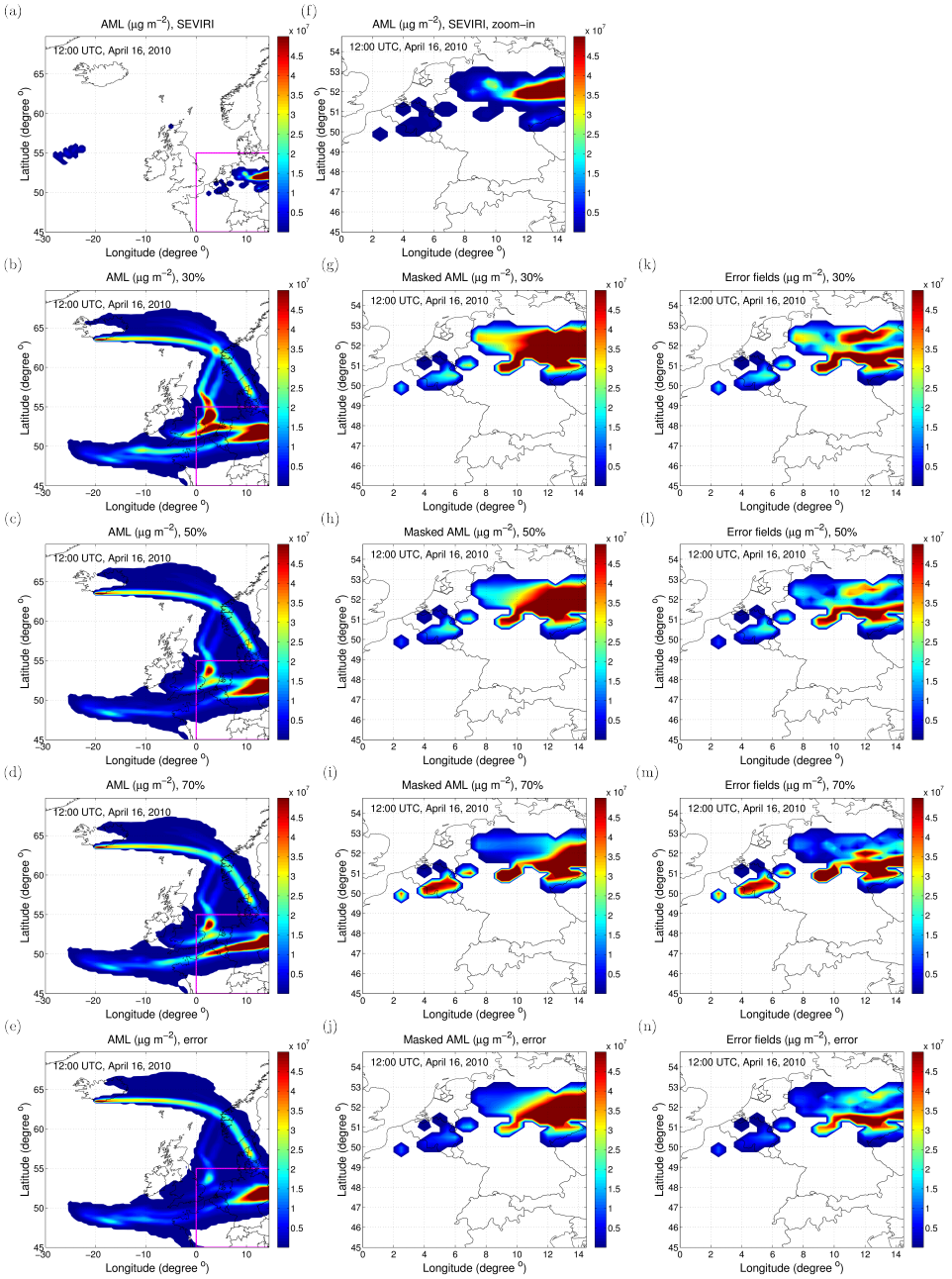

Figure 6.12: Free forecasts (AML) at 12:00 UTC, April 16, 2010, simulated with estimates of observational error covariance matrices generated from: (b) 30% uncertainty; (c) 50% uncertainty; (d) 70% uncertainty; and (e) the SEVIRI retrieval error data. The middle column shows the zoomed-in AML fields of the left column in the masked area (colored pixels in (a)). The right column is the error fields of the middle column compared with (e) the SEVIRI AML fields.

assumptions.

The estimation results are shown by Fig. 6.10. By observing the original estimation results without using correction schemes, i.e. est shown by the green lines, it can be noticed that: 30% uncertainty is an underestimation so that the injection height is not well identified, since the lower spike is larger than the spike at the injection layer; 70% uncertainty is an overestimation so that the estimate is too close to the background emission and observation data has little effect on the DA process. The 50% uncertainty balances the influence of the background emission and the observations. In addition, by observing the length of spike at the injection layer of the estimation with the penalty correction (est_pc) or background correction (est_bc), the correction algorithm has an increasingly correcting effect with higher observational uncertainty.

The initial conditions displayed in Fig. 6.11 are computed from the original estimated emissions, i.e. est solutions in Fig. 6.10. The influence of observational uncertainties on the forecasts are being tested, so it will be chosen among est, est_pc and est_bc for the one that can be distinguished the most by the use of a different uncertainty. In Fig. 6.11, although the entire ash clouds look similar in the left column, it can be noticed from the middle column that the clouds vary in the masked area. The right column gives the error fields using data assimilation. Here, we observe that using 50% uncertainty or retrieval error data results in a more accurate initial condition.

The free forecasts are shown in Fig. 6.12. We can see that the shapes and positions of the red parts formed by the estimated emissions in the left column vary. From the middle column, it can be seen that 70% uncertainty (Fig. 6.12 (i)) works the worst on the assimilation since the red parts cover a larger area (the Belgium area) compared to the SEVIRI figure 6.12 (f), while uncertainties of 50% and 30% work similarly as shown in Figs. 6.12 (h) and 6.12 (g). However, Fig. 6.12 (c) seems to be more reasonable with smaller concentrations than 6.12(b) around the Netherlands, Belgium, Luxembourg and Northern France. Using error data produces a forecast (Fig. 6.12 (j)) which matches the best to the red parts in the SEVIRI figure (Fig. 6.12 (f)). The right column confirms what we observe from the middle column, using 30% uncertainty has little influence in the masked area, while using 50% and 70% uncertainties can correct the ash-dense area (red parts) partly. Using the retrieval error data corrects most of the ash-dense area.

6.4.4. Evaluation with CALIPSO data

Additional spaceborn data is available from the Cloud-Aerosol Lidar with Orthogonal Polarization (CALIOP) lidar on the Cloud-Aerosol Lidar and Infrared Pathfider Satellite Observation (CALIPSO) platform (Winker *et al.*, 2012). This data is used for the evaluation of the vertical structure of the simulated ash cloud after the assimilation. Analysis is given on the total attenuated backscatter signal at 532 nm, which responds to aerosols including volcanic ash. On April 15, at 13:30 UTC, CALIPSO passed over the ash cloud (Fig. 6.13 (a)) and detected the cloud at around 6-7 km a.s.l. from $62.5°$N-$63.5°$N (Fig. 6.13 (c)).

The simulated AML results after the assimilation is shown in Fig. 6.13(a). We can

see that the position where ash cloud with high concentration passes the CALIPSO track (62.5°N-63.5°N) is in agreement with the CALIPSO data. In addition, evaluation is given on the vertical ash concentration profile at 62.75°N, 12.5°W using the CALIPSO data near this location. The altitude (around 6-7 km) and thickness (around 1 km) of the simulated ash cloud (Fig. 6.13 (b)) are clearly similar to the observations (Fig. 6.13 (c)).

6.4.5. Comparison with other observations

Additional spaceborn data is available from the Cloud-Aerosol Lidar with Orthogonal Polarization (CALIOP) lidar on the Cloud-Aerosol Lidar and Infrared Pathfider Satellite Observation (CALIPSO) platform (Winker *et al.*, 2012). This data is used for the evaluation of the vertical structure of the simulated ash cloud after the assimilation. Analysis is given on the total attenuated backscatter signal at 532 nm, which responds to aerosol including volcanic ash. On April 15, at 13:30 UTC, CALIPSO passed over the ash cloud (Fig. 6.13 (a)) and detected the cloud at around 6-7 km a.s.l. from 62.5°N-63.5°N (Fig. 6.13 (c)).

The simulated AML results after the assimilation are provided in Fig. 6.13(a). We can see that the position where ash cloud with high concentration passes the CALIPSO track (62.5°N-63.5°N) is in agreement with the CALIPSO data. In addition, evaluation is given on the vertical ash concentration profile at 62.75°N, 12.5°W using the CALIPSO data near this location. The altitude and thickness of the ash cloud are clearly similar to the observations.

6.5. Summary and conclusions

In this chapter, the potentials of applying the modified Trj4DVar approach to estimate the volcanic ash emissions using ash mass loadings retrieved from SEVIRI data have been explored. Discussion has been given on the preprocessing of the data and a procedure was proposed to exclude the influence of retrieval noise and the invalid detection of ash on the assimilation results. This preprocessing is necessary for achieving a more accurate estimate of the emissions. It is not a time-consuming procedure where the computational cost for data to be assimilated is much less than one model simulation during the assimilation window.

Due to the insufficiency of the data, it was recommended to estimate the emission using a proper time range which does not necessarily coincide with the observational time range. The emission time range was computed by tracing back to where the ash released covered most of the valid data area. Furthermore, we suggest to use the retrieval error data, which was obtained as a by-product of the ash mass loading data, in the construction of observational error covariance matrix as an extra benefit from the satellite data.

The modified Trj4DVar showed good performance on this case study. Its computational cost was affordable (33 minutes using 6-hour assimilation window on a computer mentioned in section 6.4, or about 13 forward simulations in our case). Therefore, the modified Trj4DVar bears a great potential for use in operational volcanic ash forecasting using assimilation of ash columns in conjunction with ground-

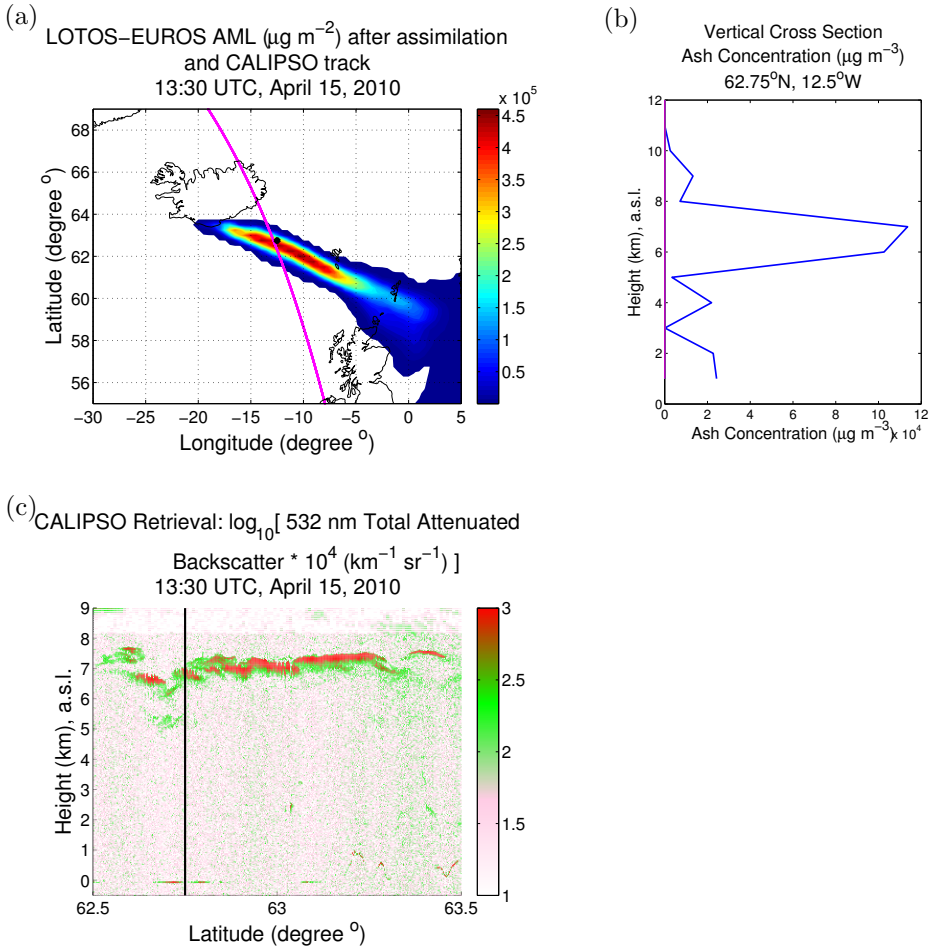

Figure 6.13: Comparison of the simulation results after the assimilation and the CALIPSO observations at 13:30 UTC, April 15, 2010: (a) LOTOS-EUROS simulated volcanic ash forecast (AML), the CALIPSO track illustrated by the magenta curve, and the evaluation spot marked by black dot; (b) vertical profile of volcanic ash concentration located at 62.75°N, 12.5°W, marked by a black dot in (a); (c) CALIPSO total backscatter at 532nm.

based observations of PH and MER. In other applications, the information of PH and MER may not be averaged and validated every 6 hours, thus assimilation windows of adaptive length could be considered. In order to utilize data of other satellite instruments, adjustments should be made in the preprocessing of the data and in the specification of the observational uncertainty. For instance, the construction of the observational error covariance can be adjusted according to the retrieval error data.

7

Evaluation criteria on the design for assimilating remote sensing data using variational approaches

Remote sensing, as a powerful tool for monitoring atmospheric phenomena, has been playing an increasingly important role in inverse modeling. Remote sensing instruments measure quantities that often combine several state variables as one. This creates very strong correlations between the state variables which share the same observation variable. This may cause numerical problems resulting in a low convergence rate or inaccurate estimates in gradient-based variational assimilation if improper error statistics are used. In this chapter, two criteria or scoring rules are proposed to quantify the numerical robustness of assimilating a specific set of remote sensing observations and to quantify the reliability of the estimates of the parameters. The criteria are derived by analyzing how the correlations are created via shared observation data and how they may influence the process of variational data assimilation. Experimental tests are conducted and show a good agreement with theory. The results illustrate the capability of the criteria to indicate the reliability of the assimilation process. Both criteria can be used with Observation System Simulation Experiments (OSSEs), and in combination of other verification scores.

Parts of this chapter are under review in:
Lu, S.*, Heemink, A., Lin, H.-X., Segers, A., and Fu, G. (2016). Evaluation criteria on the design on the assimilation of remote sensing data using variational approach. ***M*onthly Weather Review**.

7.1. Introduction

During the past three decades, the assimilation of atmospheric observations to improve the forecast of air quality and to construct the re-analysis of past weather and climate change has gained growing interest (Talagrand and Courtier, 1987; Elbern and Schmidt, 2001; Elbern *et al.*, 2007; Fu *et al.*, 2015). The available observations consist of a mixture of in situ, visual, and remotely sensed observations of temperature, wind velocity, pressure, humidity and clouds (McMurry, 2000; Clemitshaw, 2004; Lahoz *et al.*, 2010). Remote sensing makes it possible to collect data from dangerous or inaccessible areas, and meteorological satellites provide an indispensable supplement to the conventional meteorological observing system. Due to the ability of acquiring data in the traditionally data-poor regions of oceans, stratosphere and the Southern Hemisphere, and the high horizontal resolution, satellite observations have played an increasingly important role in atmospheric studies (Bocquet *et al.*, 2015; Fu *et al.*, 2016). Numerous experiments have been conducted in order to make good use of the satellite data in operational numerical weather forecasting or to improve the analysis and understanding of atmospheric phenomena and dynamics.

The assimilation of satellite data and other remote sensing data using variational approaches has been successfully applied to various atmospheric problems, such as on the improvement of initial model states and on the estimation of the emissions of natural or anthropogenic pollutants. For instance, Chai *et al.* (2009); Lamsal *et al.* (2011) estimated regional or global NO_x emission inventories with satellite NO_2 column observations. Besides the estimation of a single emission specie, Huneeus *et al.* (2012) demonstrated the simultaneous estimate of global emissions of multiple gaseous and aerosol species including dust, sea salt, BC, OC, and SO_2 by assimilating daily MODIS total and fine mode aerosol optical depth AOD. Kawabata *et al.* (2014) used the non-hydrostatic 4D-Var assimilation system to assimilate the Doppler wind lidar (DWL) data to forecast the heavy rainfall event of 5 July 2010 in Japan.

The remote sensing instruments including satellite, lidar and radar acquire information without physical contact with the object (the state) by detecting the electromagnetic radiation, solar radiation or microwave radiation. The retrieval algorithm of the detections, such as satellite-retrieved AOD data (Prata and Prata, 2012) and lidar backscatter coefficients (Wang *et al.*, 2014), usually require the combination or integration of multiple state variables and subsequently Sensor-Induced Correlations (SICs) are introduced between the states which share the same combined observation data. These SICs may have a negative impact on the performance of the parameter estimation method when erroneous or improper specification of error statistics or of the prior information is used. Alternative 4D-Var approaches that lead to better conditioned estimation problems should be used to remedy this. For example, Lu *et al.* (2016b) demonstrated that using 4D-Var method with a standard form of cost function to estimate the vertical profile of the volcanic ash emission rate from the satellite ash column data could result in undesired estimates, and this was solved by a using Trajectory-based 4D-Var (Trj4DVar) approach with a reformulated cost function.

Observation System Simulation Experiments (OSSEs) are an important tool for evaluating the potential impact of proposed observing systems, as well as for evaluating trade-offs in observing system design, and in developing and assessing improved methodology for assimilating new observations (Atlas, 1997). These OSSEs are used in combination with scoring rules and verification skills, which usually measure the deviations between forecasts and observation values, the hits, misses and false alarms (Mittermaier and Roberts, 2010; Gilleland *et al.*, 2009; Ebert, 2008; Gilleland *et al.*, 2010). Besides, there are many tools for observability or identifiability analysis can be used to diagnose whether the parameters can be identified from a given set of observations (Paulino and de Bragança Pereira, 1994; Rothenberg, 1971; Jacquez and Greif, 1985). However, these methods focus more on the usefulness of the observations and are incapable of determining numerical robustness of the estimation procedure. The condition number of the Hessian is able to indicate the numerical performance of the gradient-based assimilation approach (variational approach). However, the computation of this condition number is computational very expensive.

In this chapter, two criteria are proposed to quantify the numerical effects of the SICs on the assimilation process. The criterion are simple and practical to implement for a rough evaluation of the numerical performance of assimilating a certain type of observations for a given application. They were inspired by the analysis in section 3.3, and were originally developed to evaluate the performance of two 4D-Var approaches with different specifications of error statistics in assimilating satellite column data to estimate a vertical-distributed emission. It is found that the two criterion can be also used for other applications using remote sensing data or other integrated data.

This chapter consists of the following topics. Section 7.2 presents two criteria to evaluate the SICs introduced by assimilating remote sensing data. Tests of the criteria are given in section 7.3 based on the case study of volcanic ash problem. The last section gives a brief summary.

7.2. The evaluation methodology

7.2.1. Preliminary knowledge about variational data assimilation

Consider a discrete dynamic model given by:

$$\mathbf{x}_k = M_k(\mathbf{x}_{k-1}, \boldsymbol{\alpha}), \tag{7.1}$$

where the subscript k represents time step t_k. $\mathbf{x}_k \in \mathbb{R}^n$ and M_k are the model state vector and its corresponding dynamics operator, respectively. $\boldsymbol{\alpha} \in \mathbb{R}^p$ is the static parameter vector including the model parameters, inputs and initials which needs to be estimated in this case.

The background or the first guess of the parameters $\boldsymbol{\alpha}^b$ are assumed to differ from the true parameters $\boldsymbol{\alpha}^t$ by stochastic perturbations:

$$\boldsymbol{\alpha}^b = \boldsymbol{\alpha}^t + \boldsymbol{\epsilon}^b, \tag{7.2}$$

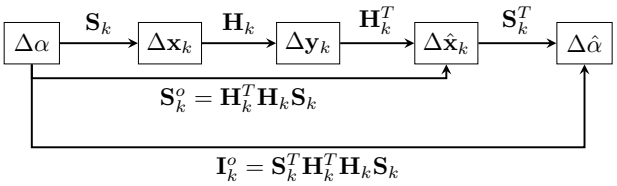

Figure 7.1: Process of gradient-based approaches

where $\boldsymbol{\epsilon}^b \sim \mathcal{N}(0, \mathbf{B})$.

Observations $\mathbf{y}^o$ at time t_k are defined by:

$$\mathbf{y}_k^o = H_k(\mathbf{x}_k^t) + \boldsymbol{\epsilon}^o, \tag{7.3}$$

where H_k is the observation operator which projects the state space into observation space, and $\boldsymbol{\epsilon}^o \sim \mathcal{N}(0, \mathbf{R}_k)$ is the observation uncertainty.

4D-Var minimizes the cost function J that measures the weighted sum of squares of distances J^b to the background parameters $\boldsymbol{\alpha}$ and J^o to the observations $\mathbf{y}^o$ obtained over a time interval $[t_0, t_{Nt}]$,

$$J(\boldsymbol{\alpha}) = \frac{1}{2}\left(\boldsymbol{\alpha} - \boldsymbol{\alpha}^b\right)^T \mathbf{B}^{-1}\left(\boldsymbol{\alpha} - \boldsymbol{\alpha}^b\right) + \frac{1}{2}\sum_{k=0}^{Nt}\left(\mathbf{y}_k - \mathbf{y}_k^o\right)^T \mathbf{R}_k^{-1}\left(\mathbf{y}_k - \mathbf{y}_k^o\right), \tag{7.4}$$

where the $\mathbf{y}_k = H_k(\mathbf{x}_k)$ represents the model-simulated observations. In this study we focus on the impact of observations on the update. Therefore, the development of the evaluation criteria requires only the observation term J^o.

The minimization usually requires the gradient of the cost function J^o with respect to the parameters:

$$\mathbf{g}^o = \nabla J^o(\boldsymbol{\alpha})^T = \sum_{k=0}^{Nt}\mathbf{S}_k^T\mathbf{H}_k^T\mathbf{R}_k^{-1}\left(\mathbf{y}_k - \mathbf{y}_k^o\right), \tag{7.5}$$

where $\mathbf{H}_k$ and $\mathbf{H}_k^T$ are the tangent linear model and its adjoint, respectively, corresponding to observation operator H_k.

$$\mathbf{S}_k = \frac{\partial\mathbf{x}_k}{\partial\boldsymbol{\alpha}} = \frac{\partial M_k}{\partial\mathbf{x}_{k-1}}\frac{\partial\mathbf{x}_{k-1}}{\partial\boldsymbol{\alpha}} + \frac{\partial M_k}{\partial\boldsymbol{\alpha}} \tag{7.6}$$

is the sensitivity of the states with respect to the parameters, and $\mathbf{S}_k^T$ is its transpose.

7.2.2. Sensor-induced correlations and their impact

Remote sensing observations, and some other observations measure quantities whose computation involves multiple state variables or parameters. SICs are created between those variables which share a common observation data, and

may have a negative numerical effect on the assimilation process or lead to ill-conditioned numerical problems. The impact of observations on the assimilation and the mechanism of a gradient-based algorithm is illustrated by Fig.7.1.

The difference $\Delta\boldsymbol{\alpha}$ between the true parameters $\boldsymbol{\alpha}^t$ and the background (first guess) parameters $\boldsymbol{\alpha}^b$ will result in a difference $\Delta\mathbf{x}_k$ between the true state fields $\mathbf{x}_k^t$ and the background state fields $\mathbf{x}_k^b$. The perturbations $\Delta\mathbf{x}_k$ are determined based on the model sensitivity behavior:

$$\Delta\mathbf{x}_k = \mathbf{S}_k\Delta\boldsymbol{\alpha}, \tag{7.7}$$

where $\mathbf{S}_k$ is given by equation (7.6).

However, $\boldsymbol{\alpha}$ or even $\mathbf{x}_k$ usually cannot be observed directly by remote sensing instruments for computing $\Delta\boldsymbol{\alpha}$ or $\Delta\mathbf{x}_k$. In order to estimate $\Delta\boldsymbol{\alpha}$, we will make use of the difference $\Delta\mathbf{y}_k$ between the true observations $\mathbf{y}_k^o$ and the simulated observations $\mathbf{y}_k$. First, the observed difference between states $\Delta\hat{\mathbf{x}}_k$ is computed by distributing $\Delta\mathbf{y}_k$ to the states according to the observational error statistics and the adjoint operational operator $\mathbf{H}_k^T$ by:

$$\Delta\hat{\mathbf{x}}_k = \mathbf{H}_k^T\mathbf{R}_k^{-1}\Delta\mathbf{y}_k = \mathbf{H}_k^T\mathbf{R}_k^{-1}\mathbf{H}_k\mathbf{S}_k\Delta\alpha = \mathbf{S}_k^o\Delta\alpha, \tag{7.8}$$

where $\mathbf{S}_k^o = \mathbf{H}_k^T\mathbf{R}_k^{-1}\mathbf{H}_k\mathbf{S}_k$ is termed the 'observed sensitivity' representing the sensitivity of states through observations with respect to the parameters. The parameters will then be updated according to model dynamics $\mathbf{S}_k$ and the observed perturbation of states $\Delta\hat{\mathbf{x}}_k$ as

$$\Delta\hat{\boldsymbol{\alpha}}_k = \mathbf{S}_k^T\Delta\hat{\mathbf{x}}_k. \tag{7.9}$$

This mechanism can be interpreted by the rewritten of the gradient in Eq. (7.5):

$$\mathbf{g}^o = \sum_{k=0}^{Nt}\mathbf{S}_k^T\mathbf{H}_k^T\mathbf{R}_k^{-1}\left(\mathbf{y}_k - \mathbf{y}_k^o\right) = \sum_{k=0}^{Nt}\mathbf{S}_k^T\left(\mathbf{H}_k^T\mathbf{R}_k^{-1}\Delta\mathbf{y}_k\right) = \sum_{k=0}^{Nt}\mathbf{S}_k^T\Delta\hat{\mathbf{x}}_k. \tag{7.10}$$

If the actual perturbation of states $\Delta\mathbf{x}_k$ is used for the update of the parameters $\Delta\tilde{\boldsymbol{\alpha}} = \mathbf{S}_k^T\Delta\mathbf{x}_k$, this update ($\Delta\tilde{\boldsymbol{\alpha}}$) is affected by no SICs. The formulation of the corresponding gradient $\mathbf{g}^c$ is given as following:

$$\mathbf{g}^c = \sum_{k=0}^{Nt}\mathbf{S}_k^T\Delta\mathbf{x}_k. \tag{7.11}$$

$\mathbf{g}^c$ can be viewed as the gradient of a cost function when using a 'complete observation operator' H^c which observes the complete states:

$$H^c(\mathbf{x}_k) = \mathbf{x}_k. \tag{7.12}$$

$\mathbf{g}^c$ reflects the model sensitivity behavior, physically only. The impact of SICs is implied by how much the observed model sensitivity differs from the physical model sensitivity, where the former is reflected by $\mathbf{g}^o$ and the latter is reflected by $\mathbf{g}^c$.

7.2.3. Evaluation criteria

Two criteria are now presented to test how much the SICs will influence the assimilation process in a negative way, which can be considered as an indication to the usefulness of the data on a given DA system.

Criterion 1 (FIM Criterion): The distance between the normalized Hessian or the normalized Fisher information matrix (FIM) generated with complete observation and remote sensing observation:

$$\left|\left| \frac{\mathbf{I}^c}{||\mathbf{I}^c||} - \frac{\mathbf{I}^o}{||\mathbf{I}^o||} \right|\right| = ||\bar{\mathbf{I}}^c - \bar{\mathbf{I}}^o||, \tag{7.13}$$

where the norm $||.||$ is Frobenius norm with $||\mathbf{A}||_F = \left(\sum_{i=1}^{m}\sum_{j=1}^{n}|a_{i,j}|^2\right)^{1/2}$ or $L_{2,1}$ norm with $||\mathbf{A}||_{2,1} = \sum_{j=1}^{n}\left(\sum_{i=1}^{m}|a_{i,j}|^2\right)^{1/2}$ for a matrix $\mathbf{A} \in \mathbb{R}^{m\times n}$. $\mathbf{I}^c = \sum_{k=0}^{Nt}\mathbf{S}_k^T\mathbf{S}_k$ and $\mathbf{I}^o = \sum_{k=0}^{Nt}\mathbf{S}_k^T\mathbf{H}_k^T\mathbf{R}_k^{-1}\mathbf{H}_k\mathbf{S}_k$ for a linear model, $\mathbf{I}^c = \partial^2 J^c/\partial\boldsymbol{\alpha}^2$ and $\mathbf{I}^o = \partial^2 J^o/\partial\boldsymbol{\alpha}^2$ for a nonlinear model or other specifications of error statistics (formulation of cost function), with J^c and J^o are the cost functions formed by complete observation and remote sensing observation, respectively.

$\mathbf{I}^c$ reflects the DA process influenced only by the physical dynamics or the model sensitivity behavior, while $\mathbf{I}^o$ reflects the performance of DA as a result of combining the observation operator and model dynamics. This criterion provides global information on how much the SICs change the sensitivity behavior that is used for the update of parameters (gradient) over iterations The FIM Criterion is practical for those cases where the FIM (Hessian) or its approximation is easy to compute.

Criterion (Gradient Criterion): The distance between the normalized model gradient and the normalized observed gradient:

$$\left|\left| \frac{\mathbf{g}^c}{||\mathbf{g}^c||} - \frac{\mathbf{g}^o}{||\mathbf{g}^o||} \right|\right| = ||\bar{\mathbf{g}}^c - \bar{\mathbf{g}}^o||, \tag{7.14}$$

or

$$\frac{1}{M}\sum_{i=1}^{M}\left|\left| \frac{\mathbf{g}_i^c}{||\mathbf{g}_i^c||} - \frac{\mathbf{g}_i^o}{||\mathbf{g}_i^o||} \right|\right| = \frac{1}{M}\sum_{i=1}^{M}||\bar{\mathbf{g}_i}^c - \bar{\mathbf{g}_i}^o||, \tag{7.15}$$

where the norm $||.||$ is Euclidean norm with $||\mathbf{a}|| = \left(\sum_{i=1}^{n}|a_i|^2\right)^{1/2}$ for a vector $\mathbf{a} \in \mathbb{R}^n$. $\mathbf{g}^c$ is the model gradient and $\mathbf{g}^o$ is the observed gradient, as defined in equation (7.11) and (7.5) for a standard cost function, respectively. Or $\mathbf{g}^o = (\nabla J^o)^T$ and $\mathbf{g}^c = (\nabla J^c)^T$ with J^o and J^c are defined as in FIM Criterion for other formulation of cost function.

Criterion (7.14) provides local and detailed information that measures the impact of SICs on the quality of gradient as well as on the convergence performance. A large value of this criterion indicates that a poor gradient is obtained using the observations. We can perturb one parameter or one state variable and compute the criterion value, which indicates whether the observation is capable of estimating the perturbed parameter. In general, perturbations can also be performed on

a set of closely-related parameters or states. Criterion (7.15) calculates in this case the mean of the differences between the two normalized gradients generated by a number of random perturbations of parameters or states, and this provides global information about whether the observed model sensitivity behavior is valid. Criterion (7.14) and (7.15) can be applied to cases where the adjoint model is available but the Hessian is difficult to obtain .

The values of the two criteria ranges from 0 to 2. A small value (say less than 0.1) implies a good observation operator, which almost preserves the characteristics of the model dynamics. The two criteria will give large values as an alarm when SICs are created by using remote sensing data or other integrated data and will lead to ill-conditioned assimilation processes. Theoretically, a bad situation occurs when the gradient is unable to distinguish the perturbed parameters and gives an equal update on each parameter, in such a case it leads to a Gradient criterion value of $\sqrt{2}\sqrt{(1-\sqrt{n}/n)} \in (0.76, 1.41)$ with $n \in [2, +\infty)$. An even worse scenario is that larger updates are given on the unperturbed parameters than on the perturbed ones, which results in even larger criteria values. Tests suggest that FIM criterion values larger than 0.9 or Gradient criterion values larger than 1.0 indicate a very ineffective assimilation process for the gradient-based method. Values less than 0.6 turned out to be acceptable for our case of volcanic ash.

Criteria (7.13) and (7.15) both provide a global assessment on the numerical robustness of the assimilation process, and on the reliability of the forecast after assimilation. The values of both criteria change with observation operators (observation position and observation type). Criterion (7.13) is invariant to perturbed variables and more robust than Criteria (7.15), while Criteria (7.15) is more simple to implement. Criteria (7.14) and (7.15) can potentially be used as a diagnostic tool to detect which parameters are correlated via observations but not physically and how this will affect the assimilation outcomes. It provides a mean to better analyze the sensitivity behavior and develop a more effective alternative method for the use of certain type of observations.

Note that, the background term J^b of the cost function plays an important role in the performance of 4D-Var approach which is able to distinguish different variable in the analysis increments and also works as a regularization term. However, this study focuses on exploring the impact of remote sensing observations and other integrated observations on the DA process, therefore in the derivation of the criteria we ignore the background term. Besides, Gradient Criteria (7.14) and (7.15) require the gradient that begins with the background (first guess), which indicates the background has no effect on the value of the criteria. The information of background is implicitly included in the observation term J^o by the use of model simulated observation $\mathbf{y}_k$. Therefore, the impact of different background and different perturbed parameters can both be tested, which are related to $\mathbf{y}_k$ and $\mathbf{y}_k^o$ in J^o, respectively.

7.2.4. Example: trajectory-based 4D-Var approach

In this section, trajectory-based 4D-Var (Trj4DVar) will be briefly reviewed and the procedure of its corresponding criteria will be described, which will be used in the case study in the next section.

Trj4DVar seeks an optimal linear combination of trajectories generated with different emissions to fit the observation data coupled with a priori information, by minimizing a reformulated 4D-Var cost function.

We assume the vector of parameters $\boldsymbol{\alpha}$ is in a parameter space spanned by the perturbed parameter sets $\Delta\boldsymbol{\alpha}^i$ $(i = 1, \cdots, p)$ and can be represented in the following form:

$$\boldsymbol{\alpha} = \boldsymbol{\alpha}^b + \sum_{i=1}^{p} \beta^i \Delta\boldsymbol{\alpha}^i, \tag{7.16}$$

where β^i is the weight of $\Delta\boldsymbol{\alpha}^i$ in the sum. If p is large the parameter space can be approximated by a smaller space spanned by a smaller number of perturbed parameters. Therefore, the determination of $\boldsymbol{\alpha}$ corresponds to estimating $\boldsymbol{\beta} = [\beta^1, \cdots, \beta^p]$.

The simulated observations $\mathbf{y}_k$ in cost function (7.4) can be approximated by:

$$\begin{aligned}
\mathbf{y}_k &= H_k(M_k(\mathbf{x}_{k-1}, \boldsymbol{\alpha})) = H_k(M_k(\mathbf{x}_{k-1}, \boldsymbol{\alpha}^b + \sum_{i=1}^{p} \beta^i \Delta\boldsymbol{\alpha}^i)) \\
&\approx H_k(M_k(\boldsymbol{x}_{k-1}, \boldsymbol{\alpha}^b)) + \sum_{i=1}^{p} \beta^i \mathbf{H}_k^T \mathbf{M}_k^T(\boldsymbol{x}_{k-1}, \Delta\boldsymbol{\alpha}^i) \\
&\approx \boldsymbol{y}_k^b + \sum_{i=1}^{p} \beta^i (H_k(M_k(\boldsymbol{x}_{k-1}, \boldsymbol{\alpha}^b + \Delta\boldsymbol{\alpha}^i)) - \mathbf{y}_k^b) \\
&= \mathbf{y}_k^b + \sum_{i=1}^{p} \beta^i \Delta\mathbf{y}_k^i,
\end{aligned} \tag{7.17}$$

where $\boldsymbol{y}_k^b = H_k(M_k(\boldsymbol{x}_{k-1}, \boldsymbol{\alpha}^b))$ are reference trajectories computed using background parameters, and $\Delta\boldsymbol{y}_k^i = H_k(M_k(\boldsymbol{x}_{k-1}, \boldsymbol{u}^b + \Delta\boldsymbol{u}^i)) - \boldsymbol{y}_k^b \approx \mathbf{H}_k^T \mathbf{M}_k^T(\boldsymbol{x}_{k-1}\Delta\boldsymbol{\alpha}^i)$ are trajectories associated with perturbation of parameters $\Delta\boldsymbol{\alpha}$ in the neighborhood of $\boldsymbol{\alpha}^b$.

Therefore, the coefficients $\boldsymbol{\beta}$ can be computed by minimizing a reformulation of the cost function (7.4) given by:

$$\begin{aligned}
J_{trj}(\boldsymbol{\beta}) &= \frac{1}{2} \sum_{k=1}^{Nt} \left(\sum_{i=1}^{p} \beta^i \Delta\boldsymbol{y}_k^i + \boldsymbol{y}_k^b - \boldsymbol{y}_k^o \right)^T [\mathbf{R}_k]^{-1} \left(\sum_{i=1}^{p} \beta^i \Delta\boldsymbol{y}_k^i + \boldsymbol{y}_k^b - \boldsymbol{y}_k^o \right) \\
&+ \frac{1}{2} \left(\sum_{i=1}^{p} \beta^i \Delta\boldsymbol{\alpha}^i \right)^T [\mathbf{B}_k]^{-1} \left(\sum_{i=1}^{p} \beta^i \Delta\boldsymbol{\alpha}^i \right) \\
&= J_{trj}^o + J_{trj}^b.
\end{aligned} \tag{7.18}$$

The gradient $\mathbf{g}^o$ of J^o in cost function (7.18) with respect to $\boldsymbol{\beta}$ now is computed

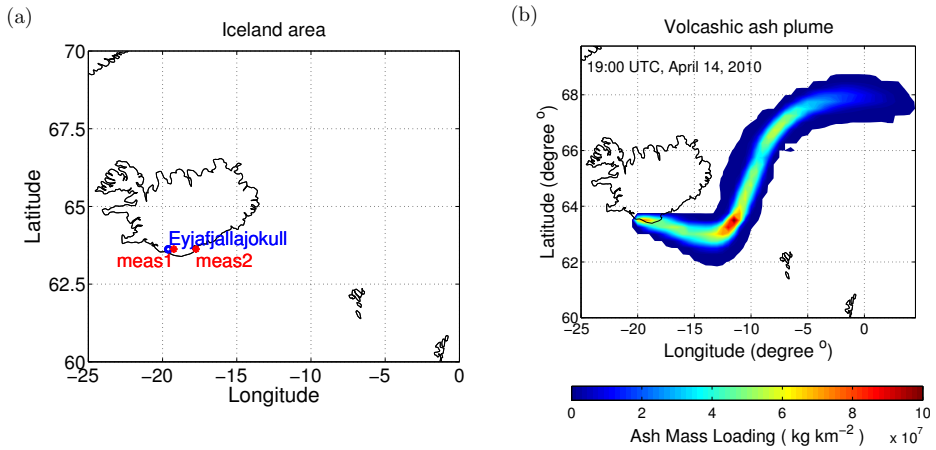

Figure 7.2: (a) Simulation and assimilation domain of Iceland area. (b) Ash columns of volcanic ash cloud at 19:00 UTC, April 14, 2010.

by:

$$\mathbf{g}^{o}_{trj} = \sum_{k=1}^{Nt} \Delta\mathbf{Y}_k^T \mathbf{R}_k^{-1} \left(\Delta\mathbf{Y}_k \boldsymbol{\beta} + \mathbf{y}_k^b - \mathbf{y}_k^o\right), \tag{7.19}$$

where $\Delta\mathbf{Y}_k = [\Delta\mathbf{y}_k^1, \cdots, \Delta\mathbf{y}_k^p]$. The Hessian can be similarly obtained as:

$$\mathbf{I}^{o}_{trj} = \sum_{k=1}^{Nt} \Delta\mathbf{Y}_k^T \mathbf{R}_k^{-1} \Delta\mathbf{Y}_k. \tag{7.20}$$

The counterparts of the gradient and Hessian for J^c can be obtained by substituting the complete observation operator (7.12) for H_k in the computation of trajectories.

7.3. Case study

We illustrate how to use both criteria for the evaluation on the effectiveness of the assimilation process and for the design of a DA system. The criteria are tested using a case where SICs typically influence the assimilation process negatively when using 4D-Var approach with a standard type of cost fucntion. It was explicitly pointed out in chapter 3 that using satellite ash-column data can result in inaccurate estimates of volcanic ash emissions. Therefore, twin experiments are conducted based on a volcanic ash estimation problem.

7.3.1. Experimental setup

Twin experiments are carried out to estimate the emission rates of volcanic ash by assimilating synthetic observations. A 3D aerosol transport model of the Iceland area (Fig. 7.2(a)) is used to simulate the eruption of the Eyjafjallajökull volcanic

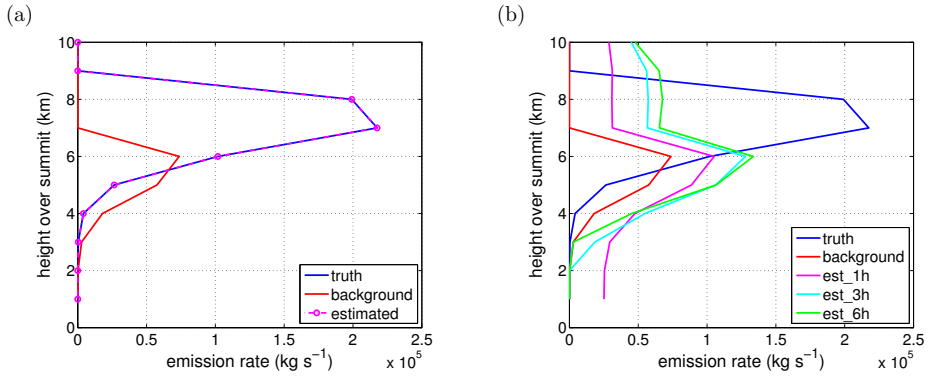

Figure 7.3: Estimation results of emission rates with (a) complete observations and (b) synthetic satellite observations.

activity during April 14-19, 2010, with a temporal resolution of 15 minutes and a spatial resolution of $0.25^\circ \times 0.25^\circ$. For simplicity, the transport model includes only advection and diffusion processes for which the adjoint model is available. Wind fields are obtained from 3-hourly meteorological data from the European Centre for Medium-Range Weather Forecasts (ECMWF), which is interpolated to hourly resolution. Figure 7.2(b) is an illustration of a volcanic ash cloud simulated by the model.

The emission information of the first few days of the explosive eruption is taken from Webley *et al.* (2012) and shown in Table 2.2 in section 2.4. The eruption is described in terms of parameters such as the total emission rate and the plume height, which are assumed to be constant during an emission episode of several hours. The 'true' emission rates in the vertical layers are generated using a Poisson distribution according to the emission information shown in Table 2.2. The 'background'/first guess emission is calculated with an underestimated total emission rate of the 'true' emission and a correspondingly lower plume height.

The synthetic observations are generated hourly by running the model with the 'true' emissions. The complete observations are 3D state fields. The satellite-like observations are ash columns computed by Eq. 3.5 given in section 3.4.1.

7.3.2. Twin experiment of using standard 4D-Var

Twin experiments are conducted with both complete observations and column-integrated observations. The results are shown in Fig. 7.3(a) and (b), respectively. In Fig. 7.3(a) it can be seen that the 'estimated' perfectly matches the 'truth', which implies that the model is physically well-conditioned and emission rates can be well estimated according to the model dynamics. However, in Fig. 7.3(b), with 1 hourly assimilation of column-integrated observations, the estimated emission rates (denoted by 'est_1h') are increased by the same amount in all layers without recognizing the vertical profile in the 'truth'. The injection layer, with the maximum of the emission rate, cannot be correctly determined. Similar results are obtained

Table 7.1: Gradient Criterion values computed from 4 single-state-perturbation experiments.

case	1 hour	3 hours	6 hours
$x_{1,6}$	1.1342	1.1618	1.2267
$x_{1,7}$	1.2203	1.1873	1.2671
$x_{2,6}$	1.0257	1.0096	1.1822
$x_{2,7}$	1.1132	1.0536	1.2442

Table 7.2: Gradient Criterion values computed from 2 single-input-perturbation experiments.

case	1 hour	3 hours	6 hours
the 5^{th} input	1.1012	0.9850	0.9510
the 7^{th} input	1.1768	1.0904	1.0331

with larger assimilation windows (3 hours and 6 hours). This shows that it is very ineffective to estimate volcanic ash emission rates using satellite data, and that this is not caused by the model but by the type of observations used.

Now we investigate the problem using the Gradient Criteria. First perturbations on a single state variable are carried out, and the model gradient and observed gradient are computed with complete observation and column-wise observation, respectively. The gradients can be viewed as sensitivities of the perturbed state with respect to the parameters (emission rates). Four single-state-perturbation experiments are performed. The first two states are located at horizontal positions shown by 'meas1' and 'meas2' in Fig. 7.2(a) marked by red asterisks, in the 6^{th} layer above the summit, denoted as $x_{1,6}$ and $x_{2,6}$, respectively. The other two are located at the same pixels as the first two, but now in the 7^{th} layer above the summit, denoted by $x_{1,7}$ and $x_{2,7}$ accordingly. The horizontal locations of the perturbed states are chosen such that they are downwind and close to the summit and thus carry more information about the parameters than those located upwind or further away. The vertical layers are chosen to be the injection layers of the 'truth' and 'background' where the injection height is located, since states at those two layers play important roles in this parameter estimation process. The Gradient criterion results given in Table 7.1 show the values all larger than 1. This implies that the observed sensitivity behavior is not able to represent the model dynamics.

Then, perturbations of a single parameter are carried out, and the model gradient and observed gradient are computed. The perturbed parameters are selected to be the inputs at the 6^{th} and 7^{th} layers, the injection layers in 'background' and 'truth', respectively. The Gradient criterion results in Table 7.2 all give large values around 1. This implies that SICs have been largely influence the numerical process for the update of the parameters, and the perturbed parameters cannot be determined accurately using this kind of error statistics. This is also reflected by the estimation results in Fig. 7.3(b), where the injection layer cannot be identified by assimilating the ash columns using a standard 4D-Var approach.

In order to diagnose how the SICs affect sensitivity behavior, the normalized model gradients and observed gradients of the parameter perturbation experiments

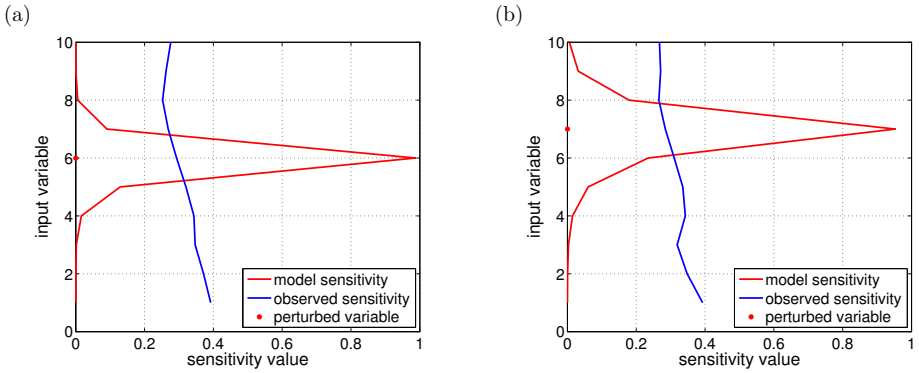

Figure 7.4: Normalized gradients generated by perturbation in a single input parameter at (a) the 6^{th} layer and (b) the 7^{th} layer above the summit, with a 1h assimilation window using Std4DVar.

are shown in Fig. 7.4. We can see that due to the model dynamics, an input variable is sensitive to its own perturbation and slightly sensitive to the inputs in the near layers. SICs are introduced by using column-integrated data, making a single input variable almost equally sensitive to all inputs and even slightly more sensitive to the variable in other layers.

7.3.3. Twin experiment of using trajectory-based 4D-Var

Based on the sensitivity analysis in section 7.3.2, Trj4DVar (see section 7.2.4) should be applied in the way of perturbing the emission rate in each layer one by one and computing the corresponding trajectories to obtain a better estimate using the ash column data. In this experiment, we will demonstrate how the two criteria are used for the configuration of the assimilation system and for a sensitivity analysis to better understand the estimation results.

The FIM criterion and Gradient criterion in Eq. (7.15) are applied for the selection between Trj4DVar and standard 4D-Var (Std4DVar), and the selection of a proper assimilation window. The criteria values are shown in Fig. 7.5, where 'std' represents Std4DVar, 'trj' represents Trj4DVar, 'FIM' represents FIM criterion and 'grd' represents Gradient criterion. It can be seen that both approaches result in criteria values which decrease with larger assimilation windows. Using Std4DVar, this decease becomes smaller. This indicates that enlarging the assimilation window will introduce less improvements in the estimates. This result is consistent with the experimental results in section 7.3.2. On the other hand, the criteria values obtained using Trj4DVar are clearly smaller and they decrease faster than those obtained using Std4DVar. Based on the diagnosis of the criteria results , we can see that Trj4DVar is a better choice for this application.

Assimilation windows larger than 3 hours lead to criteria values that are acceptable (< 0.6) for our case mentioned in section 7.2.3. 6-hour assimilation window produces the smallest values and thus is the best option. Therefore the assimilation is conducted using 6-hour window to test the performance of Trj4DVar. Figure

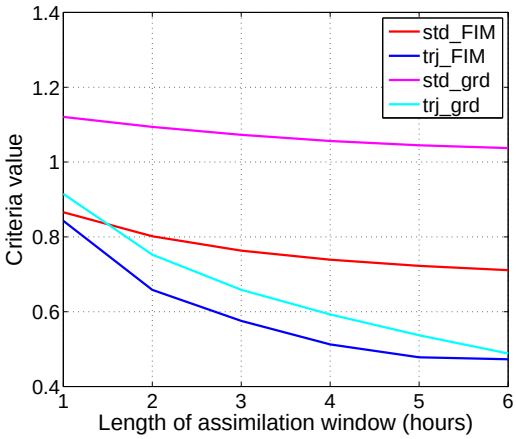

Figure 7.5: Criteria values of Std4DVar v.s. Trj4DVar.

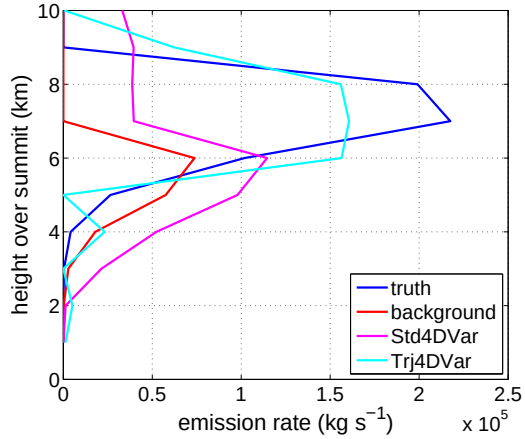

Figure 7.6: Comparison of estimation results with a 6h assimilation window using Std4DVar v.s. using Trj4DVar.

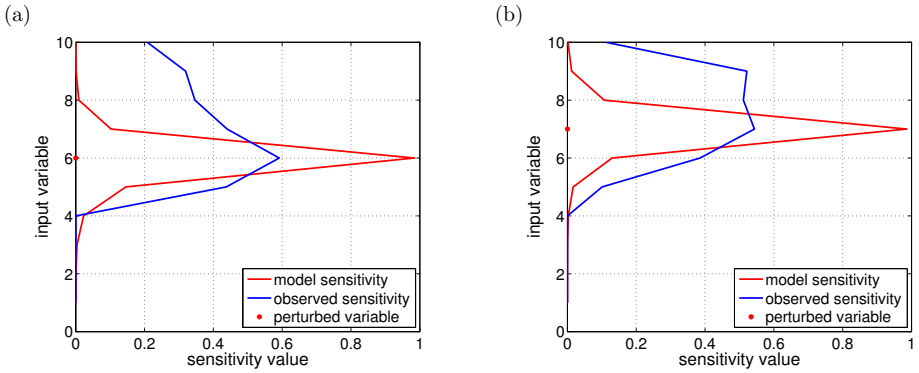

Figure 7.7: Normalized gradients generated by perturbation in a single input parameter at (a) the 5^{th} layer and (b) the 7^{th} layer, with a 6h assimilation window using Trj4DVar.

7.6 shows a comparison between the estimation results using Std4DVar and those using Trj4DVar. The vertical profile of the estimate is significantly improved using Trj4DVar. The injection layer is correctly determined in the 7^{th} layer. However, emission rates in $7^{th} - 9^{th}$ are almost the same. Parameter-perturbation experiments are conducted to illustrate the reason behind this. The normalized gradients of individually perturbing the 6^{th} and the 7^{th} inputs are illustrated in Fig. 7.7. We can observe that the $7^{th} - 9^{th}$ inputs are equally correlated. It is because meteorological patterns in the $7^{th} - 9^{th}$ layers above the summit are similar and changes occurring in any layer of the three are not distinguishable.

7

7.4. Conclusion and discussion

In this chapter two criteria were presented to evaluate the numerical performance of gradient-based parameter estimation algorithms for a given type of remote sensing observations. The first criterion (FIM) was constructed to provide global information on how numerically robust an assimilation process is, and how accurate assimilation results will be. The second one can provide local and detailed information about sensitivity behavior. This can be used to diagnose what went wrong when poor estimates were obtained. Twin experiments were carried out to validate the criteria and to illustrate how the criteria can be applied in practice for multiple purposes.

These two criteria indicate the estimation quality and the forecast quality after assimilation. They can be used for the design and configuration of an assimilation system to benefit the most from a given data set. Configurations include the selection of data when a huge amount of data are obtained, the selection of assimilation algorithm, and the configuration of the assimilation system such as the length of assimilation window. Furthermore, the criteria are also recommended as a diagnostic tool for sensitivity analysis, which provides a possibility to seek alternative methods when the use of the traditional methods is problematic due to the impact of large SICs.

It should be noticed that the two criteria are necessary not sufficient conditions

to quantify the numerical robustness of the procedure to assimilate the remote sensing data. Their benefits are that they are simple to implement and the results can be easy to understand when they are used as diagnostic tools. They can be used in OSSEs (twin experiments) where "complete observations" exists. Twin experiments performed in this chapter could be regarded as OSSE. For real system, the two criteria can be used in combination with other verification scores for forecasts. For instance, the criteria can be performed first to test the potential impact of assimilating a new type of observation on a certain application; then verification scores can be used to quantify the quality of forecasts after assimilating real data; and last, the criteria can be used as diagnostic tool for sensitivity analysis if bad results of assimilating real data occur.

8

Conclusion and Outlook

8.1. Conclusion

Volcanic eruptions, especially explosive ones, inject large amount of chemicals, corrosive gases and volcanic ash into the upper troposphere and lower stratosphere. Volcanic ash, consisting of very small rock fragments, has been known to be hazardous for human and animal health, land transportation, and aviation safety. Volcanic Ash Transport and Dispersion (VATD) models are critical tools to provide advisory information and timely volcanic ash forecasts. Even the most advanced VATDs are not capable of reproducing the reality perfectly. It is necessary to integrate available observations in the models for more accurate predictions by emloying data assimilation techniques.

An operational air-quality model - the LOTOS-EUROS, were adapted as a VATD. A new functionality was developed within the model that allowed the simulation of emission, transport (including advection and dispersion), and sedimentation of volcanic ash released during volcanic eruptions. A preprocessor tool produced an vertical ash column at the model pixel nearest to the volcano locations, based on eruption source parameters such as plume height and total emission rate, as well as additional information of timing and durations. Using this emission source, the LOTOS-EUROS model can realistically simulate transport and sedimentation of the ash cloud using its own dynamics. Parameterizations of some physical procedures such as ashfalls were adapteds.

Besides a valid VATD, eruption source parameters which are crucial for the forecasts of the locations and shapes of the ash cloud, are usually poorly known. The value of these parameters can vary frequently in a wide range depending on different eruption types, which results in the large uncertainty of the volcanic ash emission (input) to the VATDs. Therefore, the estimation of the ash emission is the main focus of this thesis. Indirect methods based on an empirical relationship were used for the calculation of mass eruption rate (MER) from observations of plume height (PH). This empirical relationship is loose, and the reproduced source

parameters can only be qualified as rough values. Therefore, observations from a more powerful monitoring tool - satellite, is considered to be assimilated. The Ash Mass Loadings (AMLs) retrieved from satellite observations contain information about the time evolution of the ash cloud, which yields good possibility of an accurate estimation of the emission.

Among all available data assimilation approaches, Four Dimensional Variational assimilation (4D-Var) approach was considered as an appropriate choice for the application. 4D-Var was first introduced in meteorological field for the estimation of initial condition, then it was proven to be a proficient tool for parameter estimation. It seeks an optimal set of parameters, including model states, initial conditions and systematic parameters, by minimizing a cost function which combines the model simulations and observations according to their statistic properties. The cost function is defined both in space and in time, which benefits from the flow dependence in the statistics by incorporating observations over a period. In addition, the parameters to be estimated can be easily accounted for in the cost function. The approach has already been used to estimate emissions of air pollutant including ozone (O3), carbon monoxide (CO), nitrogen dioxide (NO2), and aerosols/particular matter (PM), etc., by assimilating retrievals from satellite data tracing gas and aerosols of the above species.

However, it is a challenge to integrate the AMLs which lack vertical resolution for the estimation of volcanic ash emissions which are presented in forms of an eruption column. Standard 4D-Var (Std4DVar) are tested in a twin experiment framework, where synthetic observations of ash columns computed from model simulated 3D ash concentrations are used. The results show that Std4DVar is unable to reconstruct the vertical profile of the emission. Actually, the emission rate distributed to each vertical layer will increase/decrease almost in the same amount depending on the difference between the true MER and the background MER. The injection layer containing the maximal amount of emission rate cannot be accurately determined.

To deal with this problem, a Trajectory-based 4D-Var (Trj4DVar) approach is proposed. Trj4DVar reformulates the cost function in a regression type which computes the total difference between observed ash columns and a linear combination of simulated trajectories coupled with a priori emission knowledge. To construct the cost function, it decomposes the system into subsystems which represent source-receptor relationships to each source term (ash injection at each layer), thus it does not lose vertical information as Std4DVar does. The results of twin experiments show that, for most cases, Trj4DVar is capable of estimating the input emission column when a large assimilation window ($>$ 6 hours) is used.

The twin experiments is repeated where different values of noise are given in the synthetic observations or perturbations are used in the meteorologic data. The outcomes show that there is still a small possibility that Trj4DVar fails to determine the injection height accurately. Being disturbed by the weather condition (light and cloud, etc) at that moment, satellite instrument can be hampered to observe the ash cloud, which may increase the possibility of failure for the use of Trj4DVar. To remedy this, Trj4DVar is modified to incorporate observations of PH and MER in addition to satellite AMLs. The modification aims at restricting the maximal fraction

of emission rate to the injection layer. The modified Trj4DVar is able to accurately estimate injection height the based on the results of twin experiments.

When it comes to using real-life field data, the situation is more complicated. The detection of volcanic ash can be disturbed by the weather condition such as water vapor. This will result in observations of undetected or wrongly-detected ash. Besides, many sensors ,such as UV and visible sensors, have limited temporal coverage which can only observe during daylight. Due to the temporal and sometimes spatial insufficiency of the data, study is taken on how to use the data properly in order to benefit more and produce a reasonable estimate. A prepossessing procedure and guidance on the proper use of satellite data is provided.

Finally, a deeper analysis is given on the failure of using Std4DVar in this application. It is found that using Std4DVar to assimilation remote sensing data can be tricky. Remote sensing instruments measure quantities that combine several state variables. This creates SICs between the state variables which share the same observation variable. The SICs may cause numerical problems resulting in a low convergence rate or inaccurate estimates in gradient-based variational assimilation when an improper specification of error statistics are used. Two criteria are proposed to quantify the numerical effects of the SICs, which can be regarded as indications of the effectiveness of the assimilation process and the forecast quality. They are tested in the twin experiments. The results show that they are able to give evaluation on the design and configuration of the assimilation system with remote sensing data, and the evaluation on how well the forecast with assimilation can reproduce the 'truth'.

8.2. Outlook

There are still unresolved problems or challenges remain, which can be inspiring for further research. Some suggestions and topics that might be interesting are discussed in the following.

Based on the experimental results of this thesis, the modified Trj4DVar are shown to bear a great potential for use in operational volcanic ash forecasting using assimilation of ash columns in conjunction with ground-based observations of PH and MER. Adaption should be made on the approach for applications to other volcanoes. First, due to the experimental results and the fact that the information of PH and MER were averaged and validated every 6 hours, 6 hour is an optimal length of the assimilation windows in this case. For other cases, the selection of assimilation window should be based on examination and eruption type, or assimilation window with adaptable length can be considered. Second, in order to utilize data of other satellite instruments, adjustments should be made in the preprocessing of the data and in the specification of the observational uncertainty. For instance, the construction of the observational error covariance can be adjusted according to the retrieval error data.

Care should be taken of using remote sensing data. The mapping of model states into observation space usually involves the integration of several states in a column/row. SICs are created between the state variables which share a common observation variable. This will have different influence the assimilation process and

the quality of estimation for different specifications of error statistics. Interesting topics are triggered on the use of this kind of data (integrated data). Firstly, evaluation schemes can be developed to numerical robustness of assimilating the data, and assess effectiveness of assimilation process or the quality of estimates. Secondly, new method can be developed for the assimilation of this data, for instance, Trj4DVar can be extended to general cases. Thirdly, the 2D retrievals of remote sensing data can be transfered to the 3D state fields to be assimilated.

References

Annen, C. and Wagner, J.-J., *The Impact of Volcanic Eruptions During the 1990s,* Natural Hazards Review **4**, 169 (2003).

Ansmann, A., Tesche, M., Groß, S., Freudenthaler, V., Seifert, P., Hiebsch, A., Schmidt, J., Wandinger, U., Mattis, I., Müller, D., and Wiegner, M., *The 16 April 2010 major volcanic ash plume over central Europe: EARLINET lidar and AERONET photometer observations at Leipzig and Munich, Germany,* Geophys. Res. Lett. **37**, L13810+ (2010).

Arason, P., Petersen, G. N., and Bjornsson, H., *Observations of the altitude of the volcanic plume during the eruption of Eyjafjallajökull, April–May 2010,* Earth System Science Data **3**, 9 (2011).

Armienti, P., Macedonio, G., and Pareschi, M. T., *A numerical model for simulation of tephra transport and deposition: Applications to May 18, 1980, Mount St. Helens eruption,* J. Geophys. Res. **93**, 6463 (1988).

Atlas, R., *Atmospheric observations and experiments to assess their usefulness in data assimilation,* Journal of Meteorological Society of Japan **75**, 111 (1997).

Barbu, A. L., Segers, A. J., Schaap, M., Heemink, A. W., and Builtjes, P. J. H., *A multi-component data assimilation experiment directed to sulphur dioxide and sulphate over Europe,* Atmospheric Environment **43**, 1622 (2009).

Baxter, P. J., Bonadonna, C., Dupree, R., Hards, V. L., Kohn, S. C., Murphy, M. D., Nichols, A., Nicholson, R. A., Norton, G., Searl, A., Sparks, R. S., and Vickers, B. P., *Cristobalite in volcanic ash of the soufriere hills volcano, montserrat, british west indies,* Science (New York, N.Y.) **283**, 1142 (1999).

Bocquet, M., *Parameter-field estimation for atmospheric dispersion: application to the Chernobyl accident using 4D-Var,* Q.J.R. Meteorol. Soc. **138**, 664 (2012).

Bocquet, M., Elbern, H., Eskes, H., Hirtl, M., Žabkar, R., Carmichael, G. R., Flemming, J., Inness, A., Pagowski, M., Camaño, J. L. P., Saide, P. E., San Jose, R., Sofiev, M., Vira, J., Baklanov, A., Carnevale, C., Grell, G., and Seigneur, C., *Data assimilation in atmospheric chemistry models: current status and future prospects for coupled chemistry meteorology models,* Atmospheric Chemistry and Physics Discussions **14**, 32233 (2014).

Bocquet, M., Elbern, H., Eskes, H., Hirtl, M., Žabkar, R., Carmichael, G. R., Flemming, J., Inness, A., Pagowski, M., Pérez Camaño, J. L., Saide, P. E., San Jose, R., Sofiev,

M., Vira, J., Baklanov, A., Carnevale, C., Grell, G., and Seigneur, C., *Data assimilation in atmospheric chemistry models: current status and future prospects for coupled chemistry meteorology models,* Atmospheric Chemistry and Physics **15**, 5325 (2015).

Bonadonna, C. and Costa, A., *Plume height, volume, and classification of explosive volcanic eruptions based on the Weibull function, Bulletin of Volcanology*, **75**, 1 (2013).

Bonadonna, C., Ernst, G. G. J., and Sparks, R. S. J., *Thickness variations and volume estimates of tephra fall deposits: the importance of particle Reynolds number,* Journal of Volcanology and Geothermal Research **81**, 173 (1998).

Bonadonna, C. and Houghton, B. F., *Total grain-size distribution and volume of tephra-fall deposits,* Bulletin of Volcanology **67**, 441 (2005).

Bonadonna, C., Macedonio, G., and Sparks, R. S. J., *Numerical modelling of tephra fallout associated with dome collapses and Vulcanian explosions: application to hazard assessment on Montserrat,* Geological Society, London, Memoirs **21**, 517 (2002a).

Bonadonna, C., Mayberry, G. C., Calder, E. S., Sparks, R. S. J., Choux, C., Jackson, P., Lejeune, A. M., Loughlin, S. C., Norton, G. E., Rose, W. I., Ryan, G., and Young, S. R., *Tephra fallout in the eruption of Soufrière Hills Volcano, Montserrat,* Geological Society, London, Memoirs **21**, 483 (2002b).

Bonadonna, C. and Phillips, J. C., *Sedimentation from strong volcanic plumes,* J. Geophys. Res. **108**, 2340+ (2003).

Burgers, G., Jan van Leeuwen, P., and Evensen, G., *Analysis Scheme in the Ensemble Kalman Filter,* Mon. Wea. Rev. **126**, 1719 (1998).

Bursik, M. I., Carey, S. N., and Sparks, R. S. J., *A gravity current model for the May 18, 1980 Mount St. Helens plume,* Geophys. Res. Lett. **19**, 1663 (1992a).

Bursik, M. I., Sparks, R. S. J., Gilbert, J. S., and Carey, S. N., *Sedimentation of tephra by volcanic plumes: I. Theory and its comparison with a study of the Fogo A plinian deposit, Sao Miguel (Azores), Bulletin of Volcanology*, **54**, 329 (1992b).

Cacuci, D. G., Navon, I. M., and Ionescu-Bujor, M., *Computational Methods for Data Evaluation and assimilation* (Chapman and Hall/CRC, 2013).

Carey, S. and Sparks, R. S. J., *Quantitative models of the fallout and dispersal of tephra from volcanic eruption columns, Bulletin of Volcanology*, **48**, 109 (1986).

Carey, S. N. and Sigurdsson, H., *Influence of particle aggregation on deposition of distal tephra from the MAy 18, 1980, eruption of Mount St. Helens volcano,* J. Geophys. Res. **87**, 7061 (1982).

Casadevall, T. J., *Volcanic hazards and aviation safety: Lessons of the past decade,* FAA Aviation Safety Journal **2**, 1 (1992).

Casadevall, T. J., *The 1989–1990 eruption of Redoubt Volcano, Alaska: impacts on aircraft operations,* Journal of Volcanology and Geothermal Research **62**, 301 (1994).

Casadevall, T. J., Delos Reyes, P. J., and Schneider, D. J., *The 1991 Pinatubo eruptions and their effects on aircraft operations, In: Newhall CG, Punongbayan RS (eds) Fire and Mud: eruptions and lahars of Mount Pinatubo, Philippines*, , 625 (1996).

Chai, T., Carmichael, G. R., Tang, Y., Sandu, A., Heckel, A., Richter, A., and Burrows, J. P., *Regional NOx emission inversion through a four-dimensional variational approach using SCIAMACHY tropospheric NO2 column observations,* Atmospheric Environment **43**, 5046 (2009).

Christopher, S. A., Feng, N., Naeger, A., Johnson, B., and Marenco, F., *Satellite remote sensing analysis of the 2010 Eyjafjallajökull volcanic ash cloud over the North Sea during 4–18 May 2010,* J. Geophys. Res. **117**, D00U20+ (2012).

Clemitshaw, K., *A Review of Instrumentation and Measurement Techniques for Ground-Based and Airborne Field Studies of Gas-Phase Tropospheric Chemistry,* Critical Reviews in Environmental Science and Technology **34**, 1 (2004).

Connor, C. B., Hill, B. E., Winfrey, B., Franklin, N. M., and Femina, P. C., *Estimation of Volcanic Hazards from Tephra Fallout,* Natural Hazards Review **2**, 33 (2001).

Cook, R. J., Barron, J. C., Papendick, R. I., and Williams, G. J., *Impact on agriculture of the mount st. Helens eruptions.* Science (New York, N.Y.) **211**, 16 (1981).

Costa, A., Macedonio, G., and Folch, A., *A three-dimensional Eulerian model for transport and deposition of volcanic ashes,* Earth and Planetary Science Letters **241**, 634 (2006).

Courtier, P. and Talagrand, O., *Variational Assimilation of Meteorological Observations With the Adjoint Vorticity Equation. Ii: Numerical Results,* Q.J.R. Meteorol. Soc. **113**, 1329 (1987).

Courtier, P., Thépaut, J. N., and Hollingsworth, A., *A strategy for operational implementation of 4D-Var, using an incremental approach,* Q.J.R. Meteorol. Soc. **120**, 1367 (1994).

Cronin, S. J., Hedley, M. J., Smith, R. G., and Neall, V. E., *Impact of Ruapehu ash fall on soil and pasture nutrient status 1. October 1995 eruptions,* New Zealand Journal of Agricultural Research **40**, 383 (1997).

Cronin, S. J., Neall, V. E., Lecointre, J. A., Hedley, M. J., and Loganathan, P., *Environmental hazards of fluoride in volcanic ash: a case study from Ruapehu volcano, New Zealand,* Journal of Volcanology and Geothermal Research **121**, 271 (2003).

Curier, R. L., Timmermans, R., Calabretta-Jongen, S., Eskes, H., Segers, A., Swart, D., and Schaap, M., *Improving ozone forecasts over Europe by synergistic use of the LOTOS-EUROS chemical transport model and in-situ measurements,* Atmospheric Environment **60**, 217 (2012).

Dacre, H. F., Grant, A. L. M., Hogan, R. J., Belcher, S. E., Thomson, D. J., Devenish, B. J., Marenco, F., Hort, M. C., Haywood, J. M., Ansmann, A., Mattis, I., and Clarisse, L., *Evaluating the structure and magnitude of the ash plume during the initial phase of the 2010 Eyjafjallajökull eruption using lidar observations and NAME simulations,* J. Geophys. Res. **116**, D00U03+ (2011).

Dacre, H. F., Grant, A. L. M., and Johnson, B. T., *Aircraft observations and model simulations of concentration and particle size distribution in the Eyjafjallajökull volcanic ash cloud,* Atmospheric Chemistry and Physics **13**, 1277 (2013).

D'amours, R., *Modeling the ETEX plume dispersion with the Canadian emergency response model,* Atmospheric Environment **32**, 4335 (1998).

Dee, D. P. and Da Silva, A. M., *Data assimilation in the presence of forecast bias,* Q.J.R. Meteorol. Soc. **124**, 269 (1998).

Dimet, f.-X. and Talagrand, O., *Variational algorithms for analysis and assimilation of meteorological observations: theoretical aspects,* Tellus A **38A**, 97 (1986).

Doicu, A., Trautmann, T., and Schreier, F., *Numerical Regularization for Atmospheric Inverse Problems* (Springer-Verlag and Praxis Publishing, 2010).

Draxler, R. R. and Hess, G. D., *An overview of the HYSPLIT_4 modeling system of trajectories, dispersion, and deposition,* Australian Meteorological Magazine **47**, 295 (1998).

Durant, A. J. and Rose, W. I., *Sedimentological constraints on hydrometeor-enhanced particle deposition: 1992 Eruptions of Crater Peak, Alaska,* Journal of Volcanology and Geothermal Research **186**, 40 (2009).

Durant, A. J., Rose, W. I., Sarna-Wojcicki, A. M., Carey, S., and Volentik, A. C. M., *Hydrometeor-enhanced tephra sedimentation: Constraints from the 18 May 1980 eruption of Mount St. Helens,* Journal of Geophysical Research **114** (2009), 10.1029/2008jb005756.

Ebert, E. E., *Fuzzy verification of high-resolution gridded forecasts: a review and proposed framework,* Met. Apps **15**, 51 (2008).

Eckhardt, S., Prata, A. J., Seibert, P., Stebel, K., and Stohl, A., *Estimation of the vertical profile of sulfur dioxide injection into the atmosphere by a volcanic eruption using satellite column measurements and inverse transport modeling,* Atmospheric Chemistry and Physics **8**, 3881 (2008).

Elbern, H. and Schmidt, H., *Ozone episode analysis by four-dimensional variational chemistry data assimilation,* J. Geophys. Res. **106**, 3569 (2001).

Elbern, H., Schmidt, H., and Ebel, A., *Variational data assimilation for tropospheric chemistry modeling,* J. Geophys. Res. **102**, 15967 (1997).

Elbern, H., Schmidt, H., Talagrand, O., and Ebel, A., *4D-variational data assimilation with an adjoint air quality model for emission analysis,* Environmental Modelling & Software **15**, 539 (2000).

Elbern, H., Strunk, A., Schmidt, H., and Talagrand, O., *Emission rate and chemical state estimation by 4-dimensional variational inversion,* Atmospheric Chemistry and Physics **7**, 3749 (2007).

Errera, Q. and Fonteyn, D., *Four-dimensional variational chemical assimilation of CRISTA stratospheric measurements,* J. Geophys. Res. **106**, 12253 (2001).

Evensen, G., *Sequential data assimilation with a nonlinear quasi-geostrophic model using Monte Carlo methods to forecast error statistics,* J. Geophys. Res. **99**, 10143 (1994).

Fertig, E. J., Baek, s.-J., Hunt, B. R., Ott, E., Szunyogh, I., Aravéquia, J. A., Kalnay, E., Li, H., and Liu, J., *Observation bias correction with an ensemble Kalman filter,* Tellus A **61**, 210 (2009).

Flemming, J. and Inness, A., *Volcanic sulfur dioxide plume forecasts based on UV satellite retrievals for the 2011 Grímsvötn and the 2010 Eyjafjallajökull eruption,* J. Geophys. Res. Atmos. **118**, 10,172 (2013).

Flentje, H., Claude, H., Elste, T., Gilge, S., Köhler, U., Plass-Dülmer, C., Steinbrecht, W., Thomas, W., Werner, A., and Fricke, W., *The Eyjafjallajökull eruption in April 2010 – detection of volcanic plume using in-situ measurements, ozone sondes and lidar-ceilometer profiles,* Atmospheric Chemistry and Physics **10**, 10085 (2010).

Folch, A. and Felpeto, A., *A coupled model for dispersal of tephra during sustained explosive eruptions,* Journal of Volcanology and Geothermal Research **145**, 337 (2005).

Fu, G., Lin, H.-X., Heemink, A., Segers, A., Prata, F., and Lu, S., *Satellite data assimilation to improve forecasts of volcanic ash concentrations,* Atmospheric Chemistry and Physics Discussions , 1 (2016).

Fu, G., Lin, H. X., Heemink, A. W., Segers, A. J., Lu, S., and Palsson, T., *Assimilating aircraft-based measurements to improve forecast accuracy of volcanic ash transport,* Atmospheric Environment **115**, 170 (2015).

Gilleland, E., Ahijevych, D., Brown, B. G., Casati, B., and Ebert, E. E., *Intercomparison of Spatial Forecast Verification Methods, Weather and Forecasting*, Wea. Forecasting **24**, 1416 (2009).

Gilleland, E., Ahijevych, D. A., Brown, B. G., and Ebert, E. E., *Verifying Forecasts Spatially, Bulletin of the American Meteorological Society*, Bull. Amer. Meteor. Soc. **91**, 1365 (2010).

Glaze, L. S. and Self, S., *Ashfall dispersal for the 16 September 1986, eruption of Lascar, Chile, calculated by a turbulent diffusion model,* Geophys. Res. Lett. **18**, 1237 (1991).

Gouhier, M. and Donnadieu, F., *Mass estimations of ejecta from Strombolian explosions by inversion of Doppler radar measurements,* J. Geophys. Res. **113**, B10202+ (2008).

Gudmundsson, M. T., Thordarson, T., Höskuldsson, A., Larsen, G., Björnsson, H., Prata, F. J., Oddsson, B., Magnússon, E., Högnadóttir, T., Petersen, G. N., Hayward, C. L., Stevenson, J. A., and Jónsdóttir, I., *Ash generation and distribution from the April-May 2010 eruption of Eyjafjallajökull, Iceland,* Scientific Reports **2** (2012), 10.1038/srep00572.

Guffanti, M., Mayberry, G., Casadevall, T., and Wunderman, R., *Volcanic hazards to airports, Natural Hazards*, **51**, 287 (2009).

Hakami, A., Henze, D. K., Seinfeld, J. H., Chai, T., Tang, Y., Carmichael, G. R., and Sandu, A., *Adjoint inverse modeling of black carbon during the Asian Pacific Regional Aerosol Characterization Experiment,* J. Geophys. Res. **110**, D14301+ (2005).

Harris, D. M. and Rose, W. I., *Estimating particle sizes, concentrations, and total mass of ash in volcanic clouds using weather radar,* J. Geophys. Res. **88**, 10969 (1983).

Heffter, J. L. and Stunder, B. J. B., *Volcanic Ash Forecast Transport And Dispersion (VAFTAD) Model,* Wea. Forecasting **8**, 533 (1993).

Hopkins, A. T. and Bridgman, C. J., *A volcanic ash transport model and analysis of Mount St. Helens ashfall,* J. Geophys. Res. **90**, 10620 (1985).

Horwell, C. and Baxter, P., *The respiratory health hazards of volcanic ash: a review for volcanic risk mitigation, Bulletin of Volcanology*, Bulletin of Volcanology **69**, 1 (2006).

Horwell, C. J., Sparks, R. S. J., Brewer, T. S., Llewellin, E. W., and Williamson, B. J., *Characterization of respirable volcanic ash from the Soufrière Hills volcano, Montserrat, with implications for human health hazards, Bulletin of Volcanology*, Bulletin of Volcanology **65**, 346 (2003).

Houtekamer, P. L. and Mitchell, H. L., *Data Assimilation Using an Ensemble Kalman Filter Technique,* Mon. Wea. Rev. **126**, 796 (1998).

Huneeus, N., Chevallier, F., and Boucher, O., *Estimating aerosol emissions by assimilating observed aerosol optical depth in a global aerosol model,* Atmos. Chem. Phys. **12**, 4585 (2012).

Jackson, C., Sen, M. K., and Stoffa, P. L., *An Efficient Stochastic Bayesian Approach to Optimal Parameter and Uncertainty Estimation for Climate Model Predictions,* J. Climate **17**, 2828 (2004).

Jacquez, J. A. and Greif, P., *Numerical parameter identifiability and estimability: Integrating identifiability, estimability, and optimal sampling design,* Mathematical Biosciences **77**, 201 (1985).

Jones, A., Thomson, D., Hort, M., and Devenish, B., *The U.K. Met Office's Next-Generation Atmospheric Dispersion Model, NAME III,* in *Air Pollution Modeling and Its Application XVII*, edited by Borrego, C. and Norman, A.-L. (Springer US, 2007) pp. 580–589.

Kawabata, T., Iwai, H., Seko, H., Shoji, Y., Saito, K., Ishii, S., and Mizutani, K., *Cloud-Resolving 4D-Var Assimilation of Doppler Wind Lidar Data on a Meso-Gamma-Scale Convective System,* Mon. Wea. Rev. **142**, 4484 (2014).

Konovalov, I. B., Beekmann, M., Richter, A., and Burrows, J. P., *Inverse modelling of the spatial distribution of no$_x$ emissions on a continental scale using satellite data,* Atmospheric Chemistry & Physics **6**, 1747 (2006).

Koyaguchi, T., *Grain-size variation of tephra derived from volcanic umbrella clouds, Bulletin of Volcanology*, **56**, 1 (1994).

Koyaguchi, T. and Ohno, M., *Reconstruction of eruption column dynamics on the basis of grain size of tephra fall deposits: 1. Methods,* J. Geophys. Res. **106**, 6499 (2001).

Lacasse, C., Karlsdóttir, S., Larsen, G., Soosalu, H., Rose, W. I., and Ernst, G. G. J., *Weather radar observations of the Hekla 2000 eruption cloud, Iceland, Bulletin of Volcanology*, **66**, 457 (2004).

Lahoz, W., Khattatov, B., and Menard, R., *Data assimilation – Making sense of observations*, 1st ed. (Springer-Verlag Berlin Heidelberg, 2010).

Lamsal, L. N., Martin, R. V., Padmanabhan, A., van Donkelaar, A., Zhang, Q., Sioris, C. E., Chance, K., Kurosu, T. P., and Newchurch, M. J., *Application of satellite observations for timely updates to global anthropogenic NOx emission inventories,* Geophys. Res. Lett. **38**, L05810+ (2011).

Liu, C., Xiao, Q., and Wang, B., *An Ensemble-Based Four-Dimensional Variational Data Assimilation Scheme. Part II: Observing System Simulation Experiments with Advanced Research WRF (ARW),* Mon. Wea. Rev. **137**, 1687 (2009).

Lu, S., Lin, H. X., Heemink, A., Segers, A., and Fu, G., *Estimation of volcanic ash emissions through assimilating satellite data and ground-based observations,* J. Geophys. Res. Atmos. **121**, 10,971 (2016a).

Lu, S., Lin, H. X., Heemink, A. W., Fu, G., and Segers, A. J., *Estimation of Volcanic Ash Emissions Using Trajectory-Based 4D-Var Data Assimilation,* Mon. Wea. Rev. , 575 (2016b).

Macedonio, G., Costa, A., and Longo, A., *A computer model for volcanic ash fallout and assessment of subsequent hazard,* Computers & Geosciences **31**, 837 (2005).

Macedonio, G., Pareschi, M. T., and Santacroce, R., *A numerical simulation of the Plinian Fall Phase of 79 A.D. eruption of Vesuvius,* J. Geophys. Res. **93**, 14817 (1988).

Mankin, W. G., Coffey, M. T., and Goldman, A., *Airborne observations of SO2, HCl, and O3 in the stratospheric plume of the Pinatubo Volcano in July 1991,* Geophys. Res. Lett. **19**, 179 (1992).

Marzano, F. S., Barbieri, S., Vulpiani, G., and Rose, W. I., *Volcanic Ash Cloud Retrieval by Ground-Based Microwave Weather Radar,* IEEE Transactions on Geoscience and Remote Sensing **44**, 3235 (2006a).

Marzano, F. S., Lamantea, M., Montopoli, M., Di Fabio, S., and Picciotti, E., *The Eyjafjöll explosive volcanic eruption from a microwave weather radar perspective,* Atmospheric Chemistry and Physics **11**, 9503 (2011).

Marzano, F. S., Vulpiani, G., and Rose, W. I., *Microphysical characterization of microwave Radar reflectivity due to volcanic ash clouds,* IEEE Transactions on Geoscience and Remote Sensing **44**, 313 (2006b).

Mastin, L. G., Guffanti, M., and Servranckx, R., *Alaska Volcano Observatory - A multidisciplinary effort to assign realistic source parameters to models of volcanic ash-cloud transport and dispersion during eruptions,* J. Volcan. Geoth. Res. **186**, 10 (2009a).

Mastin, L. G., Guffanti, M., Servranckx, R., Webley, P., Barsotti, S., Dean, K., Durant, A., Ewert, J. W., Neri, A., Rose, W. I., Schneider, D., Siebert, L., Stunder, B., Swanson, G., Tupper, A., Volentik, A., and Waythomas, C. F., *A multidisciplinary effort to assign realistic source parameters to models of volcanic ash-cloud transport and dispersion during eruptions,* Journal of Volcanology and Geothermal Research **186**, 10 (2009b).

McMurry, P., *A review of atmospheric aerosol measurements,* Atmospheric Environment **34**, 1959 (2000).

Meirink, J. F., Bergamaschi, P., Frankenberg, C., d'Amelio, M. T. S., Dlugokencky, E. J., Gatti, L. V., Houweling, S., Miller, J. B., Röckmann, T., Villani, M. G., and

Krol, M. C., *Four-dimensional variational data assimilation for inverse modeling of atmospheric methane emissions: Analysis of SCIAMACHY observations,* J. Geophys. Res. **113**, D17301+ (2008).

Miller, C. D., Ewert, J. W., and Andrew, B. L., *The USGS/USAID volcano disaster assistance program,* USGS open-file rep. , 93 (1993).

Mittermaier, M. and Roberts, N., *Intercomparison of Spatial Forecast Verification Methods: Identifying Skillful Spatial Scales Using the Fractions Skill Score, Weather and Forecasting*, Wea. Forecasting **25**, 343 (2010).

Mona, L., Amodeo, A., D'Amico, G., Giunta, A., Madonna, F., and Pappalardo, G., *Multi-wavelength Raman lidar observations of the Eyjafjallajökull volcanic cloud over Potenza, southern Italy,* Atmospheric Chemistry and Physics **12**, 2229 (2012).

Oxford-Economics, *The Economic Impacts of Air Travel Restrictions Due to Volcanic Ash, Report for Airbus (http://www.oxfordeconomics.com/my-oxford/projects/129051).*, Tech. Rep. (2010).

Paulino, C. and de Bragança Pereira, C., *On identifiability of parametric statistical models, Journal of the Italian Statistical Society*, Statistical Methods & Applications **3**, 125 (1994).

Penenko, V., Baklanov, A., Tsvetova, E., and Mahura, A., *Direct and Inverse Problems in a Variational Concept of Environmental Modeling, Pure and Applied Geophysics*, Pure and Applied Geophysics **169**, 447 (2012).

Penenko, V. V., *Variational methods of data assimilation and inverse problems for studying the atmosphere, ocean, and environment, Numerical Analysis and Applications*, Numerical Analysis and Applications **2**, 341 (2009).

Petäjä, T., Laakso, L., Grönholm, T., Launiainen, S., Evele-Peltoniemi, I., Virkkula, A., Leskinen, A., Backman, J., Manninen, H. E., Sipilä, M., Haapanala, S., Hämeri, K., Vanhala, E., Tuomi, T., Paatero, J., Aurela, M., Hakola, H., Makkonen, U., Hellén, H., Hillamo, R., Vira, J., Prank, M., Sofiev, M., Siitari-Kauppi, M., Laaksonen, A., Lehtinen, K. E. J., Kulmala, M., Viisanen, Y., and Kerminen, V. M., *In-situ observations of Eyjafjallajökull ash particles by hot-air balloon,* Atmospheric Environment **48**, 104 (2012).

Pfeiffer, T., Costa, A., and Macedonio, G., *A model for the numerical simulation of tephra fall deposits,* Journal of Volcanology and Geothermal Research **140**, 273 (2005).

Pierce, R. B., *Development of Data Assimilation Capabilities for SEVIRI Volcanic Ash retrievals With Georg Grell (NOAA/ESRL) Martin Stuefer (UAF) Mike Pavolonis (NOAA/NESDIS),* NOAA Satellite Science Week Virtual Meeting (2013).

Prata, *Determination of mass loadings and plume heights of volcanic ash clouds from satellite data,* (2015), 10.13140/RG.2.1.4405.2327.

Prata, A., *Satellite detection of hazardous volcanic clouds and the risk to global air traffic,* Natural Hazards **51**, 303 (2009).

Prata, A. J., *Infrared radiative transfer calculations for volcanic ash clouds,* Geophys. Res. Lett. **16**, 1293 (1989).

Prata, A. J. and Prata, A. T., *Eyjafjallajökull volcanic ash concentrations determined using Spin Enhanced Visible and Infrared Imager measurements,* J. Geophys. Res. **117**, D00U23 (2012).

Prata, A. J., Zehner, C., and Stebel, K., *Earth Observations and Volcanic Ash: A report of the ESA/Eumesat Workshop, 4-7 March, 2013*, Tech. Rep. (2014).

Pudykiewicz, J., *Numerical simulation of the transport of radioactive cloud from the Chernobyl nuclear accident,* Tellus B **40B**, 241 (1988).

Pudykiewicz, J., *Simulation of the Chernobyl dispersion with a 3-D hemispheric tracer model,* Tellus B **41B**, 391 (1989).

Rantucci, G., *Geological disasters in the Philippines : The July 1990 earthquake and the June 1991 eruption of Mount Pinatubo,* (1994).

Reichel, L. and Ye, Q., *simple square smoothing regularization operators,* ETNA. Electronic Transactions of Numerical Analysis [electronic only] **33**, 63 (2008).

Robock, A., *Volcanic eruptions and climate,* Rev. Geophys. **38**, 191 (2000).

Rose, W. I., Bluth, G. J. S., Schneider, D. J., Ernst, G. G. J., Riley, C. M., Henderson, L. J., and McGimsey, R. G., *Observations of Volcanic Clouds in Their First Few Days of Atmospheric Residence: The 1992 Eruptions of Crater Peak, Mount Spurr Volcano, Alaska,* The Journal of Geology **109**, 677 (2001).

Rose, W. I. and Durant, A. J., *Fine ash content of explosive eruptions,* Journal of Volcanology and Geothermal Research **186**, 32 (2009).

Rose, W. I., Self, S., Murrow, P. J., Bonadonna, C., Durant, A. J., and Ernst, G. G. J., *Nature and significance of small volume fall deposits at composite volcanoes: Insights from the October 14, 1974 Fuego eruption, Guatemala, Bulletin of Volcanology*, Bulletin of Volcanology **70**, 1043 (2008).

Rothenberg, T. J., *Identification in Parametric Models,* Econometrica **39**, 577 (1971).

Roustan, Y. and Bocquet, M., *Inverse modelling for mercury over Europe,* Atmospheric Chemistry and Physics **6**, 3085 (2006).

Ruiz, J. J., Pulido, M., and Miyoshi, T., *Estimating Model Parameters with Ensemble-Based Data Assimilation: A Review,* Journal of the Meteorological Society of Japan. Ser. II **91**, 79 (2013).

Schaap, M., Timmermans, R. M. A., Roemer, M., Boersen, G. A. C., Builtjes, P. J. H., Sauter, F. J., Velders, G. J. M., and Beck, J. P., *The LOTOS EUROS model: description, validation and latest developments,* International Journal of Environment and Pollution **32**, 270+ (2008).

Schmetz, J., Pili, P., Tjemkes, S., Just, D., Kerkmann, J., Rota, S., and Ratier, A., *An Introduction to Meteosat Second Generation (MSG),* Bull. Amer. Meteor. Soc. **83**, 977 (2002).

Schneider, D. J., Rose, W. I., Coke, L. R., Bluth, G. J. S., Sprod, I. E., and Krueger, A. J., *Early evolution of a stratospheric volcanic eruption cloud as observed with TOMS and AVHRR,* J. Geophys. Res. **104**, 4037 (1999).

Schwaiger, H. F., Denlinger, R. P., and Mastin, L. G., *Ash3d: A finite-volume, conservative numerical model for ash transport and tephra deposition,* Journal of Geophysical Research: Solid Earth **117**, n/a (2012).

Scollo, S., Del Carlo, P., and Coltelli, M., *Tephra fallout of 2001 Etna flank eruption: Analysis of the deposit and plume dispersion,* Journal of Volcanology and Geothermal Research **160**, 147 (2007).

Searcy, C., Dean, K., and Stringer, W., *PUFF: A high-resolution volcanic ash tracking model,* Journal of Volcanology and Geothermal Research **80**, 1 (1998).

Seibert, P., *Inverse modelling of sulfur emissions in Europe based on trajectories, Inverse Methods in Global Biogeochemical Cycles*, Washington DC American Geophysical Union Geophysical Monograph Series **114**, 147 (2000).

Shimizu, Y., Dobashi, K., Hisada, T., Ono, A., Todokoro, M., Iijima, H., Utsugi, M., Kakegawa, S., Iizuka, K., Ishizuka, T., Morikawa, A., and Mori, M., *Acute impact of volcanic ash on asthma symptoms and treatment.* International journal of immunopathology and pharmacology **20**, 9 (2007).

Sparks, Burski, M. I., Carey, S. N., Gilbert, J. S., Glaze, L. S., Sigurdsson, H., and Woods, A. W. A., *Volcanic plumes,* , 574 (1997).

Sparks, Moore, J. G., and Rice, C. J., *The initial giant umbrella cloud of the May 18th, 1980, explosive eruption of Mount St. Helens,* Journal of Volcanology and Geothermal Research **28**, 257 (1986).

Sparks, R. S. J., *The dimensions and dynamics of volcanic eruption columns, Bulletin of Volcanology*, **48**, 3 (1986).

Spence, R. J. S., Kelman, I., Baxter, P. J., Zuccaro, G., and Petrazzuoli, S., *Residential building and occupant vulnerability to tephra fall,* Natural Hazards and Earth System Science **5**, 477 (2005).

Stewart, C., Johnston, D. M., Leonard, G. S., Horwell, C. J., Thordarson, T., and Cronin, S. J., *Contamination of water supplies by volcanic ashfall: A literature review and simple impact modelling,* Journal of Volcanology and Geothermal Research **158**, 296 (2006).

Stohl, A., Prata, A. J., Eckhardt, S., Clarisse, L., Durant, A., Henne, S., Kristiansen, N. I., Minikin, A., Schumann, U., Seibert, P., Stebel, K., Thomas, H. E., Thorsteinsson, T., Tørseth, K., and Weinzierl, B., *Determination of time- and height-resolved volcanic ash emissions and their use for quantitative ash dispersion modeling: the 2010 eyjafjallajökull eruption,* Atmospheric Chemistry and Physics **11**, 4333 (2011).

Strunk, A., Ebel, A., Elbern, H., Friese, E., Goris, N., and Nieradzik, L., *Four-Dimensional Variational Assimilation of Atmospheric Chemical Data – Application to Regional Modelling of Air Quality,* in *Large-Scale Scientific Computing*, Lecture Notes in Computer Science, Vol. 5910, edited by Lirkov, I., Margenov, S., and Waśniewski, J. (Springer Berlin Heidelberg, 2010) pp. 214–222.

Stuefer, M., Freitas, S. R., Grell, G., Webley, P., Peckham, S., McKeen, S. A., and Egan, S. D., *Inclusion of ash and SO2 emissions from volcanic eruptions in WRF-Chem: development and some applications,* Geosci. Model Dev. **6**, 457 (2013).

Suzuki, T., *A theoretical model for dispersion of tephra,* in *Arc Volcanism: Physics and Tectonics*, edited by Shimozuru, D. and Yokoyama, I. (Terra Scientific Publishing Company (TERRAPUB), 1983) pp. 95–113.

Talagrand, O. and Courtier, P., *Variational Assimilation of Meteorological Observations With the Adjoint Vorticity Equation. I: Theory,* Q.J.R. Meteorol. Soc. **113**, 1311 (1987).

Taylor, H. E. and Lichte, F. E., *Chemical composition of Mount St. Helens volcanic ash,* Geophys. Res. Lett. **7**, 949 (1980).

Thomas, H. E. and Prata, A. J., *Sulphur dioxide as a volcanic ash proxy during the April–May 2010 eruption of Eyjafjallajökull Volcano, Iceland,* Atmospheric Chemistry and Physics **11**, 6871 (2011).

Tian, X., Xie, Z., and Dai, A., *An ensemble-based explicit four-dimensional variational assimilation method,* J. Geophys. Res. **113**, D21124+ (2008).

Tian, X., Xie, Z., and Sun, Q., *A POD-based ensemble four-dimensional variational assimilation method,* Tellus A **63**, 805 (2011).

Tong, M. and Xue, M., *Simultaneous Estimation of Microphysical Parameters and Atmospheric State with Simulated Radar Data and Ensemble Square Root Kalman Filter. Part II: Parameter Estimation Experiments,* Mon. Wea. Rev. **136**, 1649 (2008).

Tuck, B. H. and Huskey, L., *Economic disruptions by Redoubt Volcano; assessment methodology and anecdotal empirical evidence,* proceedings of the first international symposium on volcanic ash and aviation safety , 137 (1994).

Ucl-Irdr, *Volcanic Hazard from Iceland: Analysis and Implications of the Eyjafjallajökull Eruption (https://www.ucl.ac.uk/rdr/publications/irdr-special-reports/iceland)*, Tech. Rep. (UCL Institute for Risk and Disaster Reduction, London, 2010).

Valdebenito, A. M., Tsyro, S., Kahnert, M., and Heiberg, H., *The EMEP data assimilation system: Technical description and first results*, Tech. Rep. 4/2010 (Norwegian Meteorological Institute, 2010).

Vicente, G. A., Davenport, J. C., and Scofield, R. A., *The role of orographic and parallax corrections on real time high resolution satellite rainfall rate distribution,* International Journal of Remote Sensing **23**, 221 (2002).

Vira, J. and Sofiev, M., *On variational data assimilation for estimating the model initial conditions and emission fluxes for short-term forecasting of SOx concentrations,* Atmospheric Environment **46**, 318 (2012).

Walcek, C. J., *Minor flux adjustment near mixing ratio extremes for simplified yet highly accurate monotonic calculation of tracer advection,* J. Geophys. Res. **105**, 9335 (2000).

Wang, X., Boselli, A., D'Avino, L., Pisani, G., Spinelli, N., Amodeo, A., Chaikovsky, A., Wiegner, M., Nickovic, S., Papayannis, A., Perrone, M. R., Rizi, V., Sauvage, L., and Stohl, A., *Volcanic dust characterization by EARLINET during Etna's eruptions in 2001–2002,* Atmospheric Environment **42**, 893 (2008).

Wang, Y., Sartelet, K. N., Bocquet, M., Chazette, P., Sicard, M., D'Amico, G., Léon, J. F., Alados-Arboledas, L., Amodeo, A., Augustin, P., Bach, J., Belegante, L., Binietoglou, I., Bush, X., Comerón, A., Delbarre, H., García-Vízcaino, D., Guerrero-Rascado, J. L., Hervo, M., Iarlori, M., Kokkalis, P., Lange, D., Molero, F., Montoux, N., Muñoz, A., Muñoz, C., Nicolae, D., Papayannis, A., Pappalardo, G., Preissler, J., Rocadenbosch, F., Sellegri, K., Wagner, F., and Dulac, F., *Assimilation of lidar signals: application to aerosol forecasting in the western Mediterranean basin,* Atmospheric Chemistry and Physics **14**, 12031 (2014).

Wardman, J. B., Wilson, T. M., Bodger, P. S., Cole, J. W., and Johnston, D. M., *Investigating the electrical conductivity of volcanic ash and its effect on HV power systems,* Physics and Chemistry of the Earth, Parts A/B/C **45-46**, 128 (2012).

Weber, K., Eliasson, J., Vogel, A., Fischer, C., Pohl, T., van Haren, G., Meier, M., Grobéty, B., and Dahmann, D., *Airborne in-situ investigations of the Eyjafjallajökull volcanic ash plume on Iceland and over north-western Germany with light aircrafts and optical particle counters,* Atmospheric Environment **48**, 9 (2012).

Webley, P. W., Steensen, T., Stuefer, M., Grell, G., Freitas, S., and Pavolonis, M., *Analyzing the Eyjafjallajökull 2010 eruption using satellite remote sensing, lidar and WRF-Chem dispersion and tracking model,* J. Geophys. Res. **117**, D00U26+ (2012).

Wen, S. and Rose, W. I., *Retrieval of sizes and total masses of particles in volcanic clouds using AVHRR bands 4 and 5,* J. Geophys. Res. **99**, 5421 (1994).

Whitaker, J. S. and Hamill, T. M., *Ensemble Data Assimilation without Perturbed Observations, Monthly Weather Review*, Mon. Wea. Rev. **130**, 1913 (2002).

Wilson, G., Wilson, T. M., Deligne, N. I., and Cole, J. W., *Volcanic hazard impacts to critical infrastructure: A review,* Journal of Volcanology and Geothermal Research **286**, 148 (2014).

Wilson, T., Stewart, C., Cole, J., Johnston, D., and Cronin, S., *Vulnerability of farm water supply systems to volcanic ash fall, Environmental Earth Sciences*, **61**, 675 (2010).

Wilson, T. M., Stewart, C., Sword-Daniels, V., Leonard, G. S., Johnston, D. M., Cole, J. W., Wardman, J., Wilson, G., and Barnard, S. T., *Volcanic ash impacts on critical infrastructure,* Physics and Chemistry of the Earth, Parts A/B/C **45-46**, 5 (2012).

Winker, D. M., Liu, Z., Omar, A., Tackett, J., and Fairlie, D., *CALIOP observations of the transport of ash from the Eyjafjallajökull volcano in April 2010,* J. Geophys. Res. **117**, D00U15 (2012).

Yumimoto, K. and Uno, I., *Adjoint inverse modeling of CO emissions over Eastern Asia using four-dimensional variational data assimilation,* Atmospheric Environment **40**, 6836 (2006).

Yumimoto, K., Uno, I., Sugimoto, N., Shimizu, A., Hara, Y., and Takemura, T., *Size-resolved adjoint inversion of Asian dust,* Geophys. Res. Lett. **39**, L24808+ (2012).

Zakšek, K., Hort, M., Zaletelj, J., and Langmann, B., *Monitoring volcanic ash cloud top height through simultaneous retrieval of optical data from polar orbiting and geostationary satellites,* Atmospheric Chemistry and Physics **13**, 2589 (2013).

Zehner, C., *Monitoring Volcanic Ash from Space,* ESA Scientific & Technical Memoranda **280** (2012), 10.5270/atmch-10-01.

Zhang, L., *A size-segregated particle dry deposition scheme for an atmospheric aerosol module,* Atmospheric Environment **35**, 549 (2001).

Zupanski, D. and Zupanski, M., *Model Error Estimation Employing an Ensemble Data Assimilation Approach,* Mon. Wea. Rev. **134**, 1337 (2006).

Zupanski, M., *Maximum Likelihood Ensemble Filter: Theoretical Aspects,* Mon. Wea. Rev. **133**, 1710 (2005).

Acknowledgements

This work was carried out at Delft University of Technology in a close cooperation with TNO. I thank the financial support from China Scholarship Council.

I owe my deepest gratitude to all the people I worked with during my PhD research. This PhD thesis is a result of support and guidance from many people.

First, I would like to thank my supervisors Prof. Hai Xiang Lin and Prof. Arnold Heemink for their great help on the entire long journey of my PhD studies. I thank Hai Xiang for believing in me so that I could be a PH.D candidate at TU Delft. He gave me enough freedom and guided me to be an independent researcher. He always encouraged me to try out my ideas and to make progress step by step. I really appreciate and enjoy his supervision to allow me to do research for my own interest. I am deeply grateful to Arnold Heemink for his constructive suggestions on my research progress. I admire Arnold's extraordinary knowledge and experience in both theoretical and practical aspects of data assimilation. I feel very lucky to work with Arnold, a top expert in data assimilation, from whom I can always get the most to-the-point comment.

Many heartfelt thanks to Dr. Arjo Segers. I appreciate that I can borrow Arjo's expertise on the LOTOS-EUROS model, which saved me a lot of trouble and accelerated my research procedures. I enjoyed our monthly meeting about my research topic, where arjo always gave me very constructive suggestion and recommendation for my research questions. Although arjo's main interest is in application, he also has a very strong theoretical background in data assimilation, which helped me a lot to take practical value into account.

I thank Hai Xiang, Arnold, Arjo for introducing me to many data assimilation experts in some interesting workshops. It was really an honor to present my work at TNO regular meeting and the RIVM's LOTOS-EUROS annual workshop. I also appropriate their careful reading and useful comments on my every journal manuscript and draft thesis. They were very patient throughout those iterations of revision, so that I was able to publish my results on the top journals.

Next, I would like to express my gratitude to my colleague – Guangliang Fu. We worked in the same research team, exchanged ideas, shared experience, and helped each other from time to time. Discussion and sometimes arguments with him over some topics usually inspired me. I also thank Umer Altaf for being patient on all my questions during my first two years of my PhD. Special thanks to Dr. Fred Prata (Nicarnica aviation, Norway), Dr. Jeffery Anderson (NCAR, US), PD Dr. Hendrik Elbern (Koln univ., Germany). It was a pleasure to discuss with you at EGU conference or consult you by emails. I was grateful to get your comments and suggestions.

During my whole PhD period, I have had so many good friends. I want to thank them all for taking care of me since my very beginning of being in the Netherlands. Thank Evelyn, Dorothee and Kees, they always gave me very warm supports, then I can concentrate on my research. There are also so many other dear friends in this group that I want to express my gratitude, e.g., Kaihua, Jianbing, Cong, Senlei, Tudor, Maya, Xinchao, Yuan, Changgong, Yunlong, Zhijie, Yu ….

I want to thank my master supervisors Prof. Tongchao Lu for passing me knowledge and wisdom, and giving me the opportunity to come to the Netherlands. I will remember all your words to keep working hard and thinking divergently, hopefully I can be very famous in my research field.

At last, I want to thank my mother and father. All my achievements during my PhD were related to your encouragement, support and understanding.

Sha Lu
Delft, June 2016

A

Notations

A.1. Abbreviations

Symbol	Description
VATD	Volcanic Ash Transport and Dispersion model
PH	Plume Height
MER	Mass Eruption Rate
AML	Ash Mass Loading
DA	Data assimilation
4D-Var	Four Dimensional Variational assimilation approach
Std4DVar	Standard 4D-Var approach with a standard cost function
Trj4DVar	Trajectory-based 4D-Var approach with a reformulated cost function
ESP	Eruption Source Parameter
AOD	Aerosol Optical Depth
NAME	Numerical Atmospheric-dispersion Modelling Environment
WRF-Chem	Weather Research and Forecast model coupled with Chemistry
ASL	Above Sea Level
ECMWF	European Centre for Medium-range Weather Forecast
VAA	Volcanic Ash Advisory
SEVIRI	Spinning Enhanced Visible and Infrared Imager
SIC	Sensor-Induced Correlation

A.2. Vectors

Symbol	Dimension	Description
$\mathbf{x}_k$	$[\mu g\ m^{-3}]$	state vector at k^{th} time level containing 3D volcanic ash concentration field

A

$\mathbf{y}_k$	[μg m^{-2}]	observation vector at k^{th} time level containing 2D ash mass loading field
$\mathbf{u}_k$	[kg s^{-1}]	emission rate of volcanic ash at k^{th} time level
$\mathbf{u}_k^b$	[kg s^{-1}]	background emission rate of volcanic ash at k^{th} time level
$\mathbf{u}$	[kg s^{-1}]	constant emission rate during one assimilation window
$\mathbf{u}^b$	[kg s^{-1}]	constant background emission rate during one assimilation window
$\Delta\mathbf{u}^i$	[kg s^{-1}]	perturbation on the i^{th} element of $\mathbf{u}$
$\mathbf{w}_k$	[-]	uncertainty of $\mathbf{u}_k$
$\mathbf{v}_k$	[-]	uncertainty of $\mathbf{y}_k$
$\boldsymbol{\beta}$	[-]	coefficient of linear combination of vectors $\Delta\mathbf{u}^i$
$\mathbf{g}$	[-]	gradient of cost function with respect to parameters

A.3. Matrices

Symbol	Dimension	Description
$\mathbf{B}_k$	[-]	covariance matrix of $\mathbf{w}_k$
$\mathbf{R}_k$	[-]	covariance matrix of $\mathbf{v}_k$

A.4. Operators

Symbol	Description
M_k	volcanic ash transport model
H_k	observation operator projecting then state space into the observation space
$\mathbf{M}_k$	tangent linear model of M_k
$\mathbf{H}_k$	tangent linear model of H_k
$\mathbf{M}_k^T$	adjoint model of M_k
$\mathbf{H}_k^T$	adjoint model of H_k
J	cost function
J^b	background term of cost function J
J^o	observation term of cost function J
$\mathbf{I}$	Fisher information matrix

Curriculum Vitæ

Sha Lu was born on 10 December 1986 in Shandong, China. She finished her bachelor studies in Numerical Mathematics in 2009 at Shandong University, China. From 2009 to 2012, Sha Lu continued her Master studies in Numerical Mathematics at Shandong University.

Since 2012, Sha Lu has been working on her PhD project at Delft Institute of Applied Mathematics at Delft University of Technology, the Netherlands. She worked on the project: Variational data assimilation of satellite data to estimate volcanic ash emissions. This project investigated the benefits of variational data assimilation with remote sensing observations to estimate volcanic ash emissions. The project has been supervised by Prof. H.X. Lin, Prof. A.W. Heemink and Dr. A.J. Segers. During Sha Lu's PhD project, she developed a Trj4D-Var (Trajectory-based 4D-Var) data assimilation method as an efficient method to assimilate satellite data.

For future, Sha Lu wants to contribute her data assimilation knowledge to all the related research fields.

List of Publications

Peer-Reviewed Journal Articles

1. **Lu, S.***, Lin, H.X., Heemink, A.W., Fu, G., and Segers, A.J. (2016). Estimation of Volcanic Ash Emissions Using Trajectory-Based 4D-Var Data Assimilation. ***M*onthly Weather Review** 144, 575-589, 2016. *d*oi: 10.1175/mwr-d-15-0194.1.

2. **Lu, S.***, Lin, H.-X., Heemink, A., Segers, A., and Fu, G. (2016). Estimation of volcanic ash emissions through assimilating satellite data and ground-based observations. ***J*ournal of Geophysical Research: Atmospheres** 121, 18, 10,971–10,994, 2016. *d*oi: 10.1002/2016JD025131.

3. **Lu, S.***, Lin, H.-X., Heemink, A., Segers, A., and Fu, G. (2016). Evaluation criteria on the design on the assimilation of remote sensing data using variational approach. ***M*onthly Weather Review** (under review).

Conference Publications

1. **Lu, S.***, Lin, H.X., Heemink, A.W., Segers, A.J. and Fu, G.. Estimation of volcanic ash emissions with satellite data: The inclusion of mass loading and plume height information in modified 4D-Var. ***E*GU General Assembly Conference 2015**.
   http:meetingorganizer.copernicus.org/EGU2015/EGU2015-6255.pdf.

2. **Lu, S.***, Lin, H.X., Heemink, A.W., Segers, A.J. and Fu, G.. volcanic ash emissions from satellite data using trajectory-based 4D-Var. ***E*GU General Assembly Conference 2016**.
   http:meetingorganizer.copernicus.org/EGU2016/EGU2016-3168.pdf.